Max-Planck-Institut für Kernphysik, Heidelberg, Germany
and
Centre d'Etudes Nucléaires de Bordeaux Gradignan, France

PHD THESIS

Antoine de ROUBIN

Mass measurements of neutron-rich strontium and rubidium isotopes in the region $A \approx 100$ and development of an electrospray ionization ion source

Contents

CHAPTER 1

Introduction

A nucleus is constituted by nucleons, namely the protons and the neutrons, which are linked together through the strong interaction. The nuclear chart shown in Figure 1.1 represents all the nuclei that have been identified so far. The 254 nuclides shown in black are stable, i.e. they do not spontaneously undergo radioactive decay. Up to $Z = 20$, they have an equivalent neutron number, i.e. $Z \sim N$. For higher values of Z, the number of neutrons becomes more important than the number of protons, in order to counteract the Coulomb repulsion which evolves as a function of Z^2. These stable nuclei form the so-called valley of stability, and together with 34 more nuclei with sufficiently long half-lives, are identified as primordial. It means that their half-life is comparable to or greater than the Earth's age of 4.5 billion years.

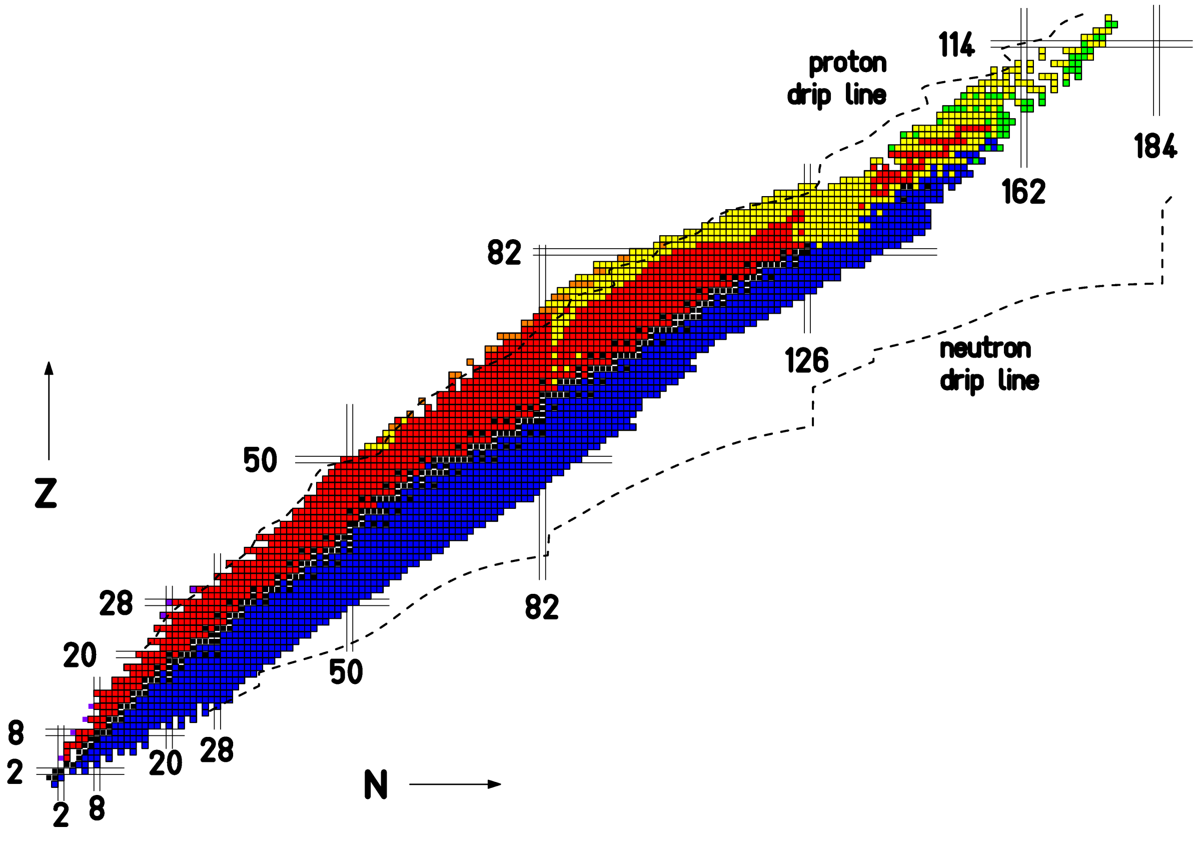

Figure 1.1 – Representation of the nuclear chart with the stable nuclei in black and the radioactive nuclei in different colors, depending on their decay mode.

All the nuclides which are not stable can be identified as exotic nuclei. They are represented in Figure 1.1 by different colors depending on their decay mode. For an exotic nucleus having a proton number Z between 1 and 82, its instability originates from an unbalanced number of protons and neutrons (with respect to the stable nuclei). The nucleus tries thus to reach the stability via the conversion of a proton to a neutron, or the other way about, this is the β-process (or β decay). A capture of an orbiting electron might also induce the conversion of a proton into a neutron (electron capture). The β decay and the electron capture are two processes governed by the weak interaction. For heavier nuclei ($Z > 82$) the energy release can also proceed due to the Coulomb interaction, through an α-particle emission (α decay) or, in some cases, a spontaneous fission[1]. Note that the α decay can also appear for very neutron deficient nuclei with $Z < 82$. From all of these energy emissions results an enhancement of the nuclear stability. The radioactive decay is a stochastic process, thus impossible to predict. However, from an ensemble of atoms (of the same species) the decay rate, also called half-life, can be calculated.

These exotic nuclei have become in the last decade the favorite playground of nuclear physicists.Indeed, the number of exotic nuclei in more important than the number of the stable one (~ 3000 exotic nuclei for only ~ 300 stable nuclei), extending therefore the possibilities for testing and developing nuclear models. In this particular case, for the study of the nuclear deformation.

The nucleus is not a solid object for which the shape is well defined. All of its nucleons, described by wave functions, are interacting with each other. Another way for a nucleus to minimize its potential energy (in other words increase its stability) is by allowing different configurations for its nucleons, relative to their wave function. These configurations have an impact on the *nuclear shape*. The notion of shape for a nucleus has thus to be understood as the mean occupation of the space by its nucleons. This occupied space can be close to a sphere or more *deformed*, depending on the spatial characteristics of the nucleon wave functions. For nuclei having a *magic number* of nucleons the shape is spherical. For all other exotic nuclei, their shape differs from the sphere, the nucleus is then considered as deformed. The most common shape for a deformed nucleus is ellipsoidal.

Different regions of deformation are identified along the nuclear chart. The one investigated in this work is located on the neutron-rich side of the nuclear chart far from stability ($A \approx 100$), between the isotopic chains of krypton ($Z = 36$) and molybdenum ($Z = 42$). The interest in this region resides in its sudden onset of deformation at neutron number $N = 60$, making it one of the most dramatic shape changes on the nuclear chart. The "southwest" border of this region of deformation is unknown, and experimental data are of great importance in the nuclear structure discussion and essential ingredients for the improvement of mass models.

A nuclear deformation can be experimentally studied via γ-ray spectroscopy [ENS 2016], mass measurements [Wang 2012] or charge radii measurements [Angeli 2013]. In this work, the region of interest has been investigated through the mass measurements of $^{100-102}$Sr and $^{100-102}$Rb isotopes with the ISOLTRAP [Mukherjee 2008] mass spectrometer at ISOLDE/CERN [Kugler 2000]. The results presented in this work, and more particularly the first mass measurements of ^{102}Sr and ^{101,102}Rb, allow to extend the knowledge of this region of deformation.

Nowadays, the most precise device for mass measurements is the Penning trap. However, the process takes time and for exotic nuclei having a half-life of less than 50 ms, a Penning-trap mass measurement starts to be limited in terms of sensitivity, precision or resolution. The shortest-lived nuclide measured with the ISOLTRAP precision trap is ^{100}Rb, having a half-life of 48(3) ms [Manea 2013]. In 2010 an electrostatic ion trap called multi-reflection time-of-flight mass spectrometer (MR-TOF MS) was installed at ISOLTRAP. Formerly planned for beam purification purposes, its fast measurement cycles and its sensitivity have made it a tool of choice for mass measurement of short-lived species. In this work, the MR-TOF MS was used as a beam purifier for the strontium mass measurements and as a mass spectrometer for the rubidium mass measurements.

The principles of the different ion traps used in this work (Penning trap, Paul trap and electrostatic trap) are introduced in the first chapter of the thesis.

The second chapter presents the region of deformation $A \approx 100$ and the impact of the $^{100-102}$Sr and

---

[1] One can note here that an energy emission is not always induced by a nuclear transmutation. For example, an excited nucleus can release its energy via a γ ray (γ decay) or by energy transmission to one of the orbiting electron, causing it to be ejected (internal conversion).

$^{100-102}$Rb mass measurements in this region. The chapter starts with a presentation of the different nuclear models developed through the years which have attempted to reproduce and predict the nuclear deformation. The region of deformation of interest is then introduced and the different experimental evidences of deformation are shown. It follows a presentation of the ISOLTRAP mass spectrometer and the results obtained for the $^{100-102}$Sr and $^{100-102}$Rb mass measurements. Finally, a comparison of the experimental masses and charge radii values with the most recent Hartree-Fock-Bogoliubov calculations takes place at the end of the chapter. However, the state-of-the-art calculations in the region of interest are only performed for even-even nuclei. In order to better understand the trend of the ground-state properties along the isotopic chains of interest, Hartree-Fock-Bogoliubov calculations with the HFODD solver [Schunck 2012, Dobaczewski 2009a] and the SLy4 parametrization [Chabanat 1998] of the Skyrme interaction were performed for the Sr and Kr isotopic chains.

Finally, in the third chapter of this thesis is presented the development of an electrospray ion source. In the framework of mass spectrometry, reference ions are of great importance for calibration purposes. Surface ionization ion sources are one of the easiest types of sources used to provide such ions. However, the species one can produce are limited to alkali elements. In order to extend our knowledge in nuclear physics, a broad mass range of reference ions are more and more solicited. An ion source being able to deliver any kind of reference ions would thus be of a great help. Electrospraying an alcoholic solution is one way to produce these reference molecular ions. The electrospray ion source presented in this work is an updated version of the one developed at RIKEN [Naimi 2013]. It is constituted of an electrospray ionization system, an rf-carpet and a quadrupole mass spectrometer. The early commissioning of this device is presented.

CHAPTER 2

Ion trapping basics

Contents

2.1 Introduction

The Heisenberg's uncertainty principle given by the inequality: $\Delta E \cdot \Delta t \geqslant h/2\pi$ (with ΔE the uncertainty on the energy measurement, Δt the observation time, and h the Planck's constant) states that precise energy measurements require long observation times. However, a long measurement time implies that the particle of interest has to be confined in a well-defined environment, i.e. free of uncontrolled events. Over the years, several solutions have been found to store particles. One of them, the so-called ion trap, uses electromagnetic fields to confine charged particles in a finite volume of space [Brown 1982, Dehmelt 1990, Paul 1990]. The motion of an ion inside a trap is function of its charge-over-mass ratio (q/m). As a consequence, the device can be used as a mass separator to separate ions having different q/m, or as a mass spectrometer to measure the q/m value of a specific ion.

In this work, a particular attention will be given on three different ion traps; the Penning-trap, the linear Paul trap and an electrostatic ion trap, the multi-reflection time of flight mass spectrometer (MR-TOF MS). A brief introduction on these devices is given in this chapter.

2.2 Penning trap

The birth of the Penning trap was the invention of the cold cathode vacuum gauge by F. M. Penning in 1936. The idea of this gauge is to ionize a gas in a chamber, and to measure the resulting ion current, which is thus proportional to the gas pressure [Penning 1936].

The principle is the following: an anode is mounted at the center of a cylinder, the cathode. A potential difference (≈ 3 kV) is applied between the anode and the cathode, creating electrons. On their path to the cathode, the electrons ionize the gas and the produced ions are collected on the anode as a current proportional to the gas pressure. In addition, a magnetic field, perpendicular to the particle momentum, force the electrons to oscillate at the cyclotron frequency, extending their path in the gas volume, thus increasing significantly the ionization probability. The key point of the gauge mechanism, which has led to the invention of the ion trap, is the effect of the magnetic field on the electrons.

The description of the confinement mechanism is credited to J. R. Pierce [Pierce 1954]. In his book is discussed the principle of a magnetron trap. Within the discussion, conditions of a pure quadrupole electric field and a magnetic field needed to trap electrons are mentioned, as well as solutions for the trapping stability. For the first time, the motion of three-dimensional confinement via an electromagnetic field is approached.

According to his biographical [Nobelprize.org 1989], H. G. Dehmelt got his inspiration from the work of F. M. Penning and J. R. Pierce. H. G. Dehmelt is the first one who mathematically described the three eigenmotions of an electron inside a magnetron trap: the axial, the magnetron and the modified cyclotron motions. In 1959 he built the first high vacuum magnetron trap, and succeeded to trap electrons for about ten seconds [Dehmelt 1976]. The Penning trap was named after F. M. Penning by H. G. Dehmelt in reference to his preliminary work on ion trapping. H. G. Dehmelt and W. Paul received the Nobel Prize in Physics in 1989 for their work on ion traps, the Penning trap and the Paul trap. The Penning trap is described in the following, the Paul trap will be discussed in section 2.3.

In its quality of mass spectrometer, a Penning trap can be used for beam purification and/or precise mass measurements. In this work an experimental set-up which uses Penning traps will be described: the ISOLTRAP experiment [Mukherjee 2008]. It two Penning traps, the first one mainly dedicated to beam purification, although it can also be used for mass measurements, the second one designed for precise mass measurements. In chapter 2 the mass measurements of neutron rich rubidium and strontium isotopes performed with the ISOLTRAP mass spectrometer will be presented.

2.2.1 Three-dimensional confinement in an ideal Penning trap

To confine a charged particle in three dimensions with a Penning trap, one needs a strong homogeneous magnetic field for the radial confinement, and an electrostatic potential for the axial trapping. The simplest Penning trap, see Figure 2.1, is constituted by three electrodes; two endcaps and one ring. The trap is placed in a strong magnetic field created by a superconducting magnet. A potential difference is applied between the endcaps and the ring electrode. In the ideal case, the electrodes are infinite hyperboloids of revolution, creating a perfect axially symmetric electric quadrupole potential $\phi(r,z)$. However, in reality the electrodes have finite dimensions, see Figure 2.1, which results in field imperfections. This point will be discussed in section 2.2.2.

To confine a charged particle, the electric potential has to fulfill the Laplace equation $\Delta\phi(\vec{r}) = 0$. The expression of the potential is:

$$\phi(r,z) = \frac{V_0}{4d^2}(2z^2 - r^2), \tag{2.1}$$

with V_0 being the potential difference between the ring electrode and the endcaps, and d a geometric parameter which characterizes the Penning trap:

$$d = \sqrt{\frac{1}{2}(z_0^2 + \frac{r_0^2}{2})}. \tag{2.2}$$

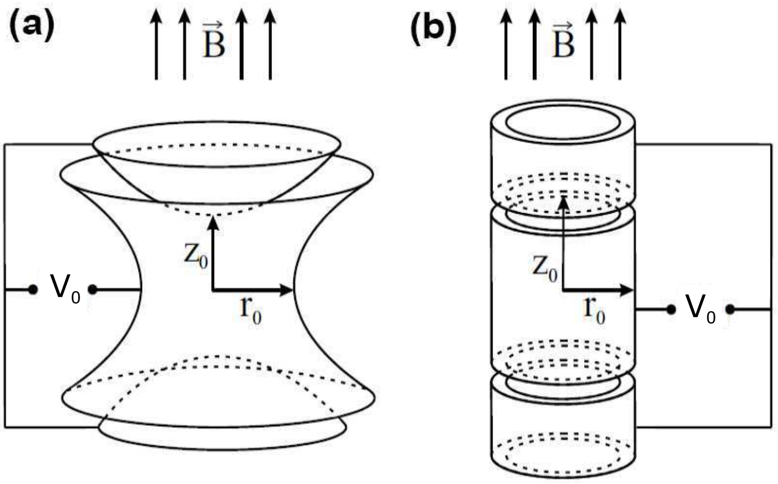

Figure 2.1 – Two different representations of a simple Penning trap constituted by one ring electrode in the middle, surrounded by two endcap electrodes. The magnetic field is represented by $\vec{B}$. A potential difference V_0 is applied between the ring electrode and the endcap electrodes. z_0 and r_0 are the distances between the trap center and the endcaps and the ring electrode, respectively. (a) represents a hyperbolic Penning trap, (b) represents a cylindrical Penning trap. Picture from [Naimi 2010a].

z_0 and r_0 being the minimal distances from the trap center to the endcaps and from the trap center to the ring electrodes, respectively.

The interaction of the charged particles with the electromagnetic field is described by the Lorentz force law:

$$\vec{F} = q(\vec{E} + \vec{v} \times \vec{B}), \tag{2.3}$$

with $\vec{B} = B\vec{e}_z$ the magnetic field, and $\vec{E} = -\vec{\nabla}\phi$ the electric field.

The equations of the ion motion in a Penning trap have been extensively solved through the years (see [Brown 1982]). In this paragraph, only a summary of the results will be given. The solving of the equations results in three different eigenmotions, as shown in Figure 2.2. One of them is the axial motion, and the two others are the radial motions. Each motion has its corresponding eigenfrequency. These three independent motions with their corresponding frequencies allow the manipulation of the ions by applying radio-frequency fields at these frequencies. This is described in section 2.2.3.

The axial motion is a harmonic oscillation around the trap center. Its corresponding eigenfrequency is:

$$\nu_z = \frac{1}{2\pi}\sqrt{\frac{qV_0}{md^2}}, \tag{2.4}$$

with q/m the charge-over-mass ratio of the stored ion.

The radial motions are the modified cyclotron motion and the magnetron motion, respectively. The corresponding frequencies are ν_+ and ν_-, respectively:

$$\nu_\pm = \frac{1}{2}\left(\nu_c \pm \sqrt{\nu_c^2 - 2\nu_z^2}\right), \tag{2.5}$$

where the cyclotron frequency ν_c is, in the ideal Penning trap, equal to the sum of the two radial eigenfrequencies:

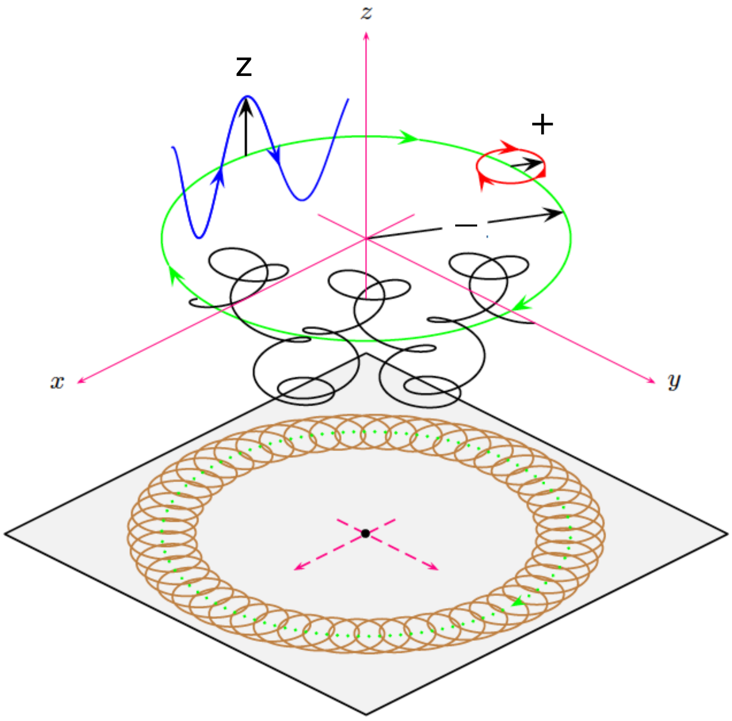

Figure 2.2 – Representation of the three eigenmotions of an ion inside a Penning trap. The axial motion (z) is represented in blue. The two radial motions are in red and in green, representing the modified cyclotron motion (+) and the magnetron motion (-), respectively. The superposition of the three motions is represented in black. Figure from [Ketter 2015].

$$\nu_c = \nu_+ + \nu_-. \tag{2.6}$$

ν_c can also be expressed as a function of the magnetic field and the charge-over-mass ratio of the ion of interest:

$$\nu_c = \frac{qB}{2\pi m}. \tag{2.7}$$

To first order, the magnetron frequency and the reduced cyclotron frequency can be expressed as:

$$\nu_- \approx \frac{V_0}{4\pi d^2 B}, \tag{2.8}$$

and

$$\nu_+ \approx \nu_c - \frac{V_0}{4\pi d^2 B}, \tag{2.9}$$

respectively. Via the different expressions of the eigenfrequencies, one can deduce the two trapping conditions. To yield a stable motion, the square root of equation (2.5) has to be real, i.e. $\nu_c^2 - 2\nu_z^2 > 0$. The combination of this equation with equation (2.4) and equation (2.7) gives the conditions for stable confinement of a charged particle in an ideal Penning trap:

$$\frac{|q|}{m}B^2 > \frac{2|V_0|}{d^2} \text{ and } qV_0 > 0. \tag{2.10}$$

The first condition defines the minimum magnetic field to apply in order to compensate the electric field, which is not confining in the radial direction. The second condition states that the sign of the electric field is the same as the trapped charged particle sign.

From equation (2.5), an important relation can be verified:

$$\nu_c^2 = \nu_+^2 + \nu_-^2 + \nu_z^2. \tag{2.11}$$

This equation is known as the invariance theorem [Brown 1982] and is also valid for a real trap.

Penning traps are not always designed with a hyperbolic shape, but can also have a cylindrical shape, see Figure 2.1 (right). The storage volume of such a trap is larger, and higher precision in the machining and alignment processes can be achieved. Similarly to the hyperbolic trap, a quadrupole electric field can be defined as well. Due to various reasons, the Penning trap (either hyperbolic or cylindrical) machining is limited in precision and the electromagnetic field cannot be defined perfectly. The consequences of these imperfections are discussed in the next section.

2.2.2 Real Penning trap

The previous section is an introduction to the ideal Penning trap. In reality a Penning trap (hyperbolic or cylindrical) suffers from many defects. Indeed, the magnetic and electric fields have imperfections, leading to a shift of the eigenfrequencies. In addition, the Coulomb force and misalignment between the electric and magnetic fields disturb the ideal ion motions in a trap. These effects are described in the following. The imperfections listed below are present for hyperbolic and cylindrical Penning traps.

Magnetic field imperfections: There are three main origins to magnetic field imperfections. Firstly, the current in the superconducting coils decreases over time: this is the flux creep phenomenon, see [Anderson 1962]. Secondly, the pressure and temperature fluctuations in the helium and nitrogen reservoirs change the magnetic permeability of the vacuum chamber. Specific studies can be performed to quantify the impact of the fluctuations and the flux creep phenomenon on the motion frequencies. In the case of ISOLTRAP, the results are reported in [Kellerbauer 2003]. Finally, ferromagnetic and/or paramagnetic materials brought too close to the trapping area can disturb the magnetic field, modifying the ion trapping conditions.

One should also consider the magnetic field homogeneity in the trapping region, which is typically in standard Penning-trap mass spectrometers about $0.1-1$ ppm for a volume of 1 cm^3.

Electric potential imperfections: In the ideal case the shape of the electrical potential is defined by the perfect shape of trap electrodes of infinite size. However, in the real case, the trap electrodes suffer from geometrical imperfections: The electrodes have finite size, some of them are segmented (required for ion manipulation techniques, see section 2.2.3 for details) or even drilled (it is the case for the endcap of hyperbolic trap in order to let the ions going in/out the trap). Furthermore, the electrode surfaces are not perfect (due to the machining), and, while assembling the trap electrodes, the electrodes might not be perfectly aligned to each other. Because of all these imperfections, the trapping potential deviates from its pure quadrupole shape. In order to minimize this deviation, one can use additional electrodes, the so-called correction electrodes. They find their place between the ring electrode and the endcaps (or even behind the endcap for a seven electrode Penning trap).

Field alignment: The alignment between the magnetic and the electric field is crucial. Indeed, a misalignment between the two fields can disturb the ion motions and induce frequency shifts. One can minimize this effect by performing an alignment of the vacuum tube with the magnetic field by using an electron gun. This device is inserted in the vacuum tube, where the Penning trap is supposed be placed. Electrons are created by heating a filament at the center of the superconducting magnet and fly along the magnetic field lines through collimators towards position sensitive detectors located at both ends of the magnet. The alignment is performed by adjusting the position of the tube so that the electrons reach the centers of both detectors.

Coulomb effect: As soon as more than one ion is trapped at the same time, the Coulomb interaction can affect the ion motions. This is why high-precision measurements are ideally performed with one single ion trapped. The Coulomb effects are difficult to predict, and experimental studies are needed to evaluate them. One of the studies was performed with the precision trap of the ISOLTRAP spectrometer [Bollen 1992] for ten to thirty ions loaded in the trap. It was concluded that in the case of two ion species trapped, frequency shifts are observed and they increase with the total number of the trapped ions.

2.2.3 Ion manipulation techniques

As mentioned in section 2.2.1, a trapped ion has three eigenmotions, and the corresponding motional amplitudes can be manipulated. To do so, sinusoidal driving fields are applied on the trap electrodes with a given frequency tuned on one of the ion eigenfrequency (or linear combination of them). The control of the radial motions is achieved by radiofrequency fields applied on the ring electrode (which have to be segmented for this purpose). The axial motion amplitude can be modified via radiofrequency fields applied on the endcaps. In the following, two different radiofrequency fields commonly used for ion motion excitations are discussed: the dipole field and the quadrupole field. Only radial motions are taken as examples.

The dipole field: A dipole field can be created by applying the opposite phases of a sinusoidal signal on the opposite segments of the ring electrode, see the left part of Figure 2.3. It results in an increase or decrease of the motion amplitude, depending on the signal phase.

The quadrupole field : A quadrupole field can be created by applying the same phase of a sinusoidal signal on opposite segments but 180° shifted to neighbouring electrodes, see right part of Figure 2.3. The frequency of a quadrupole field is tuned on the sum of two eigenfrequencies, e.g. the cyclotron frequency, being the sum of the magnetron frequency and the reduced cyclotron frequency, see equation (2.6). The quadrupole field induces a resonant periodic conversion between the two eigenmotions. If the initial motion is a pure magnetron motion, the quadrupole field will convert the motion into the modified cyclotron motion and vice-versa, depending on the signal strength and the excitation time.

The different ion manipulation techniques used in a Penning trap have been discussed in more detail in the following articles: [Bollen 1990, Kretzschmar 1999, George 2007b]. More recently, another radiofrequency field has been investigated to manipulate the ions; the octupole field. The excitation is applied on an eight fold radially segmented ring electrode and is expected to reach a higher resolution than the quadrupole excitation. More information about the octupole driving field can be found in [Eliseev 2011].

The next section will show that ion manipulation techniques allow to perform mass measurements. Another application of these manipulation techniques is the beam purification. As the ion motion is linked to its mass, excitation fields can be applied with a high mass selectivity. For example, unwanted species can be pulled away from the center of the trap, while the ions of interest remain in the center so that, via the use of a diaphragm, only the species of interest are transported to the next (precision) trap,

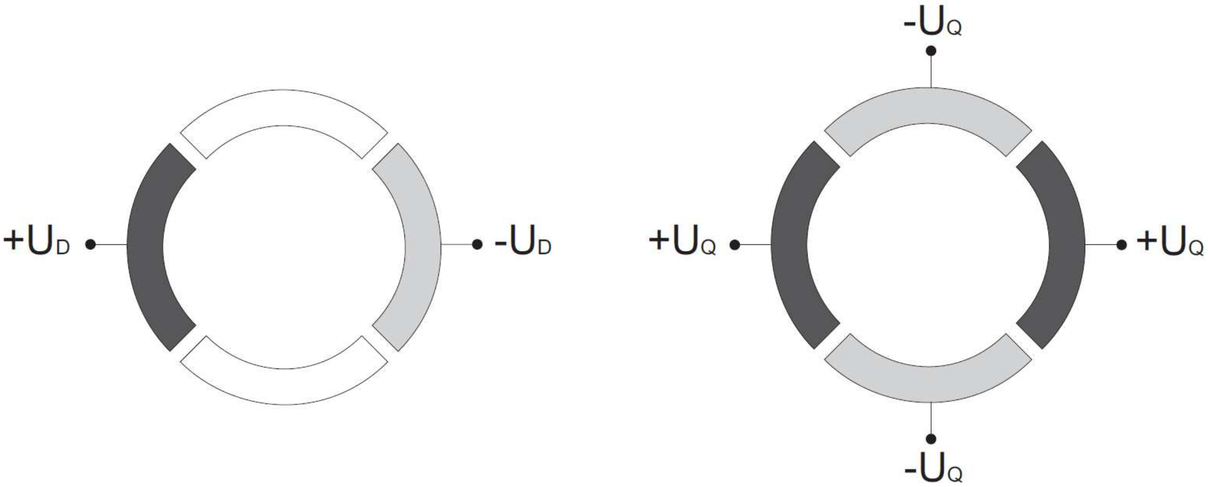

Figure 2.3 – Top view of the ring electrode of a Penning trap, which is four times radially segmented. The left side of the picture represents a configuration in order to create a dipole radiofrequency field. The right side of the picture represents a configuration in order to create a quadrupole radiofrequency field. Figure adapted from [Naimi 2010a].

as in the case of ISOLTRAP. This technique is called dipole cleaning. Another technique called resonant buffer-gas cooling technique [Savard 1991] is discussed in section 3.4.2.3.

2.2.4 Frequency measurement techniques

According to equation (2.7), the cyclotron frequency of a trapped particle is proportional to its charge-over-mass ratio. Therefore, to have access to the mass of a trapped particle, one has to measure its cyclotron frequency. To do so, different techniques can be used: the so-called TOF-ICR and PI-ICR techniques (which are destructive techniques, i.e. the ion is lost during the process), and the FT-ICR technique (non destructive). In the following, the discussion will be focused only on the time of flight ion cyclotron resonance technique (TOF-ICR) [Gräff 1980]. More information about the PI-ICR and FT-ICR techniques can be found in [Eliseev 2013] and [Comisarow 1974], respectively.

The time-of-flight ion cyclotron resonance technique (TOF-ICR): By ejecting the ion through drift electrodes towards a detector, a microchannel plate (MCP) detector for example, one can measure the ion's time of flight from the trap to the detector. This time of flight is linked to the radial motion the ion had inside the trap. The radial motion of an ion bears a magnetic moment:

$$\mu = \frac{E_r}{B} = \frac{\omega_+^2 \rho_+^2 - \omega_-^2 \rho_-^2}{B} \approx \frac{\omega_+^2 \rho_+^2}{B} \text{ with } \omega_+ \gg \omega_-, \tag{2.12}$$

with E_r being the radial kinetic energy and $\rho_\pm$ the radii of the modified cyclotron motion and magnetron motion, respectively. When the ion is ejected towards the detector, it experiences the rapid decrease in magnitude of the magnetic field, which creates an accelerating force:

$$\vec{F} = -\mu(\vec{\nabla} B). \tag{2.13}$$

From equation (2.12), one can see that the magnetic moment depends mostly on the modified cyclotron motion of the ion, as $\omega_+ \gg \omega_-$. Therefore, if the modified cyclotron motion of the trapped ion is maximized, when ejected the ion experiences a strong force $\vec{F}$ along the magnetic field lines, i.e. the axial velocity of the ion increases and the time of flight decreases.

The modified cyclotron motion of a trapped ion can be monitored via an excitation pattern. Ideally, an ion initially stored in the trap has no radial eigenmotions (in reality there is always a small motion). A dipole excitation is applied at ν_- to increase the magnetron radius, followed by a quadrupole excitation ν_{rf}, around ν_c, which converts the energy from the magnetron motion to the modified cyclotron motion. In case of a resonant excitation on ν_c, the energy transfer is more efficient and the ion time of flight is minimum. In the off-resonant case the energy transfer is less efficient and the time of flight is higher. Therefore, a scan of the quadrupole frequency ν_{rf} around ν_c allows to determine the minimum time of flight for the ion, thus, to determine the ion cyclotron frequency. The relation between the time of flight and the radio-frequency excitation is:

$$TOF_{\nu_{rf}} = \int_0^{Z_{detector}} \sqrt{\frac{m}{2(E_0 - qV(z) - E_r(\nu_{rf})B(z)/B_0)}}\,dz, \tag{2.14}$$

where E_0 is the initial axial energy of the ions, $V(z)$ the electric potential created by the drift electrodes (between the trap and the detector), $B(z)$ the strength of the magnetic field along the z-axis, and B_0 the magnetic field value in the trap region. A scheme of the technique is shown in Figure 2.4. With the TOF-ICR technique a relative uncertainty of typically $\delta m/m \sim 5 \times 10^{-8}$ is achieved for nuclei with half-lives between 50 ms and 150 ms.

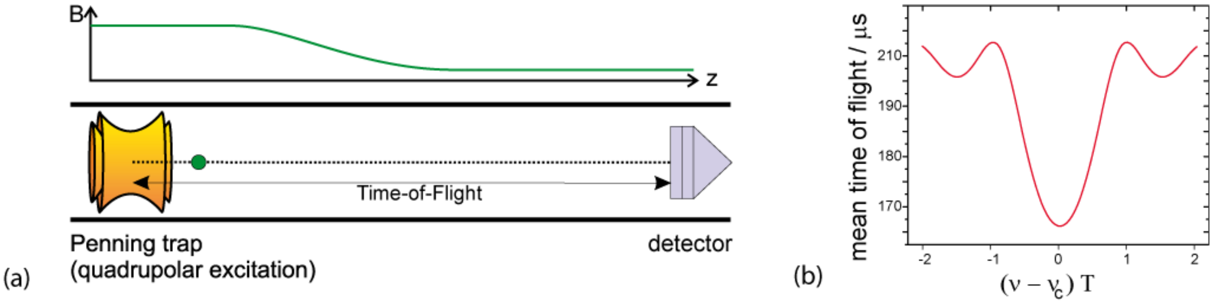

Figure 2.4 – Representation of the TOF-ICR measurement. In (a) is shown a sketch of a particle being ejected from the Penning trap and drifting towards the detector. The decrease in magnitude of the magnetic field is represented in green. In (b) is shown a typical example a TOF-ICR spectrum. Figure from [Blaum 2006].

Another excitation pattern can be used to apply a quadrupole excitation with a rectangular function, the Ramsey type excitation [George 2007a, George 2007b]. It consists of two short rectangular pulses separated by a waiting time. This excitation allows to reduce the statistical error in the frequency determination by a factor of three, while keeping the number of ions and the excitation time constant [George 2007b].

2.3 Linear Paul trap

The Paul trap was named after W. Paul. In 1951 he worked on molecular beam focalisation with quadrupole lenses [Paul 1955]. However, a quadrupole field confines only in one-dimension. When the beam is focused along the x-axis, it is unfocused along the y-axis, and vice-versa. Therefore, a regular set of alternatively converging and diverging lenses was used. It is the "strong focusing principle", see [Paul 1955, Paul 1990].

The operation mode of a Paul trap follows the idea of the strong focusing principle. As one cannot confine a charged particle in three-dimensions with only a static quadrupole field, a radiofrequency quadrupole field is employed in addition. The first application of the Paul trap was in 1964. There are two kinds of Paul traps. One is a three-dimensional Paul trap, see Figure 2.5 (a) (the radiofrequency field is applied between the ring and the endcaps). The other one is a two-dimensional linear Paul trap, also called radio-frequency quadrupole (RFQ), see Figure 2.5 (b) (the radiofrequency confinement is only in the radial direction). In this work the attention will remain on the linear Paul trap.

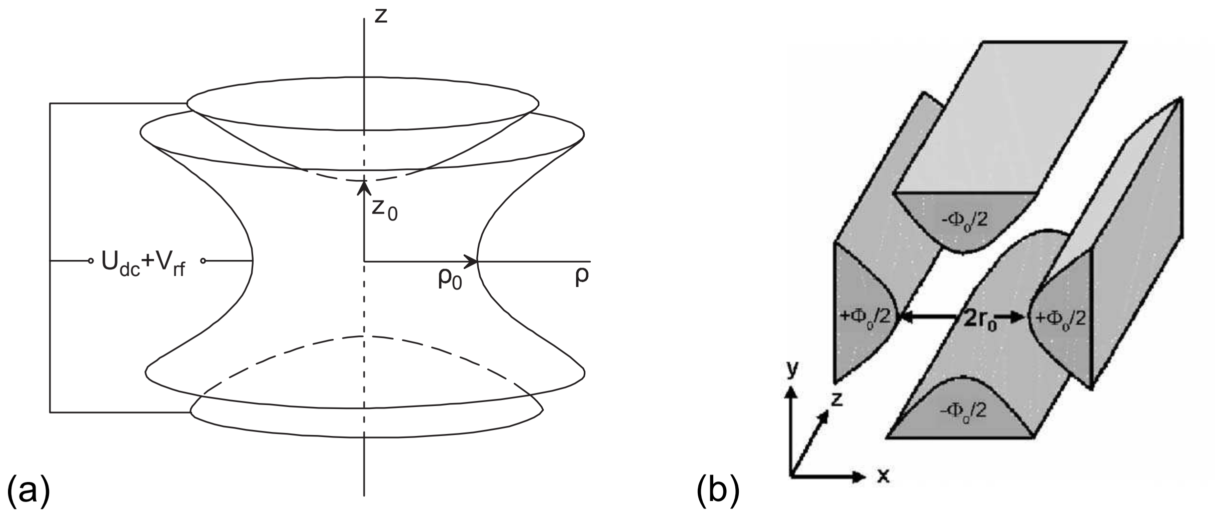

Figure 2.5 – Representation of the two kinds of Paul traps. In (a) is shown a three-dimensional Paul trap. A radiofrequency quadrupole field is applied on the electrodes, allowing to trap in 3D. In (b) is shown a linear Paul trap. The radiofrequency field is applied on the rods, allowing to confine particles radially. Adapted figure from [Blaum 2006].

2.3.1 Two-dimensional confinement in a linear Paul trap

An ideal linear Paul trap is constituted by four hyperbolic electrodes of infinite length, creating thus a perfect axially symmetric quadrupole electric trapping potential. Nevertheless, in the same way than as for a Penning trap, the electrodes are not perfect and the electric potential suffers from imperfections.

The ideal potential distribution $\phi(\vec{r},t)$ is:

$$\phi(\vec{r},t) = \frac{\phi_0(t)}{2}\frac{(x^2-y^2)}{r_0^2} \tag{2.15}$$

with

$$\phi_0(t) = \frac{1}{2}(U_{dc} + V_{rf}\cos\omega_{rf}t). \tag{2.16}$$

r_0 is the radius defined by the circle tangential to the four hyperbolic electrodes (see Figure 2.5 (b)). The rf potential oscillates between adjacent electrodes at an angular frequency $\omega_{rf} = 2\pi\nu_{rf}$, with an amplitude V_{rf} and a phase difference between neighboring electrodes of 180°. The addition of a static quadrupole electric potential U_{dc} allows to operate the linear Paul trap as a mass filter. This point will be discussed and explained in section 2.3.2.

2.3.2 Stability of trajectories

The potential $\phi(\vec{r},t)$ satisfies the Laplace equation $\nabla^2\phi = 0$, and it is invariant in the z-direction. From the interaction between an ion confined in the RFQ and the electric field results an equation of motion which is of Mathieu type:

$$\frac{d^2u}{d\xi^2} + (a_u - 2q_u \cos 2\xi)u = 0, \tag{2.17}$$

where $\xi = \omega_{rf}t/2$ and u represent the x and y independent positions of the ion in both directions. The two parameters a_u and q_u, named the Mathieu's parameters, are related to the potentials U_{dc} and V_{rf}:

$$a_u = \frac{4qU_{\mathrm{dc}}}{mr_0^2\omega_{rf}^2} \tag{2.18}$$

$$q_u = \frac{2qV_{rf}}{mr_0^2\omega_{rf}^2}, \tag{2.19}$$

where q/m is the charge-to-mass ratio.

The solutions of the equations of motion are functions of the Mathieu's parameters. In Figure 2.6a is shown the so-called Mathieu's stability diagram. It represents the stable solutions of the equations of motions for a fixed mass-to-charge ratio in the (a_u, q_u) plane. The overlapping areas I, II, III, IV, V and VI are the solutions for which the charged particle has a stable trajectory in two dimensions. For practical reasons, only the first region of stability will be discussed thereafter. A zoom of the region I for $a > 0$ is shown in Figure 2.6b. More information about the linear Paul trap can be found in [Paul 1958].

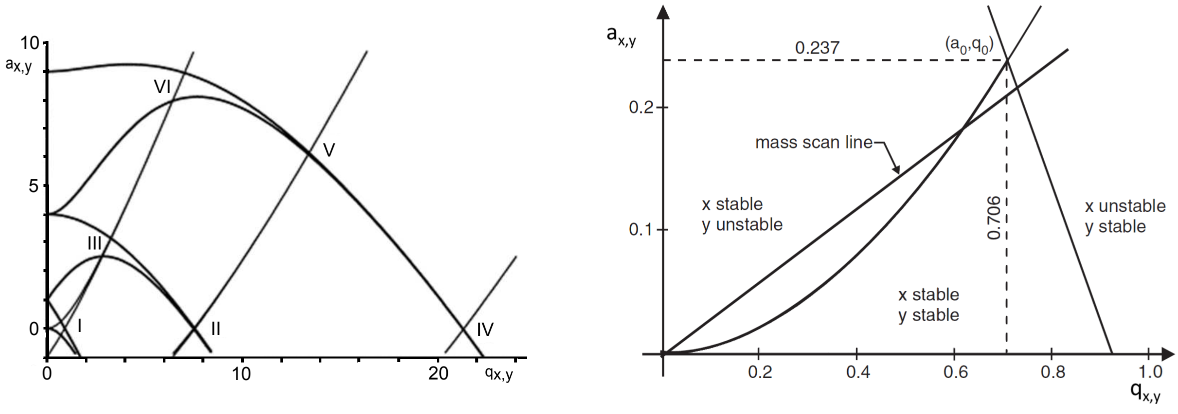

(a) (b)

Figure 2.6 – (a): Region of stabilities in a_u- and q_u-plane. The overlapping areas I, II, III, IV, V and VI are the stable solutions in both x- and y-directions. Modified figure from [Konenkov 2002]. (b): Zoom of the stability region I for $a > 0$. Modified figure from [Blaum 2006].

The fact that the trajectories can be stable for a given mass-to-charge ratio gives the possibility to use the RFQ as a mass-spectrometer. The mass selection is the result of the definition of the a_u and q_u parameters, i.e. the U_{dc} and V_{rf} potentials, respectively. This is discussed in the following.

2.3.3 Application of the linear Paul trap

2.3.3.1 Mass selection with a quadrupole mass spectrometer

As mentioned previously, the definition of the rf and dc potential amplitudes gives the possibility to mass-filter an ion beam. Via the simultaneous increase of the ac and the dc potential, one can, iteratively, mass-select the different ion species constituting the ion beam: this is a mass scan. To do so, a mass scan line, see Figure 2.6b, has to be defined. The slope of the line is the result of the division of a_u (equation (2.19)) by q_u (equation (2.18)):

$$\frac{a_u}{q_u} = \frac{2U_{dc}V_{rf}}{\Leftrightarrow} U_{dc} = V_{rf}\cdot\frac{a_u}{2q_u} \tag{2.20}$$

The closer the line is to the apex of the stable area, the higher the resolving power of the mass filter is. An example of a device dedicated to two-dimensional confinement and mass selection is the quadrupole mass spectrometer (QMS), used in the framework of the ESI source, see chapter 4. More information about the QMS operation will be given in this chapter.

2.3.3.2 A linear Paul trap cooler and buncher

The linear Paul trap can also be used to cool and bunch an ion beam. For the cooling, the device is filled with buffer gas (usually helium) at a relatively high pressure: $10^{-5} - 10^{-3}$ mbar. By elastic collisions with the buffer gas molecules, the kinetic energy of the trapped ions decreases. While the ions are cooled, the radial losses are avoided thanks to the radio frequency quadrupole field. In addition, the RFQ electrodes are longitudinally segmented, and a dc gradient is applied on these segments, in order to guide the ions to the end of the RFQ and accumulate them in the potential minimum near the exit. When the sample is large enough the ions are ejected by switching the electric potential of the last electrode, realizing ion bunches.

The RFQ installed at ISOLTRAP [Herfurth 2001] is an example of a linear Paul trap cooler and buncher, a sketch is shown in Figure 2.7. More information about the ISOLTRAP RFQ operation is given in chapter 2.

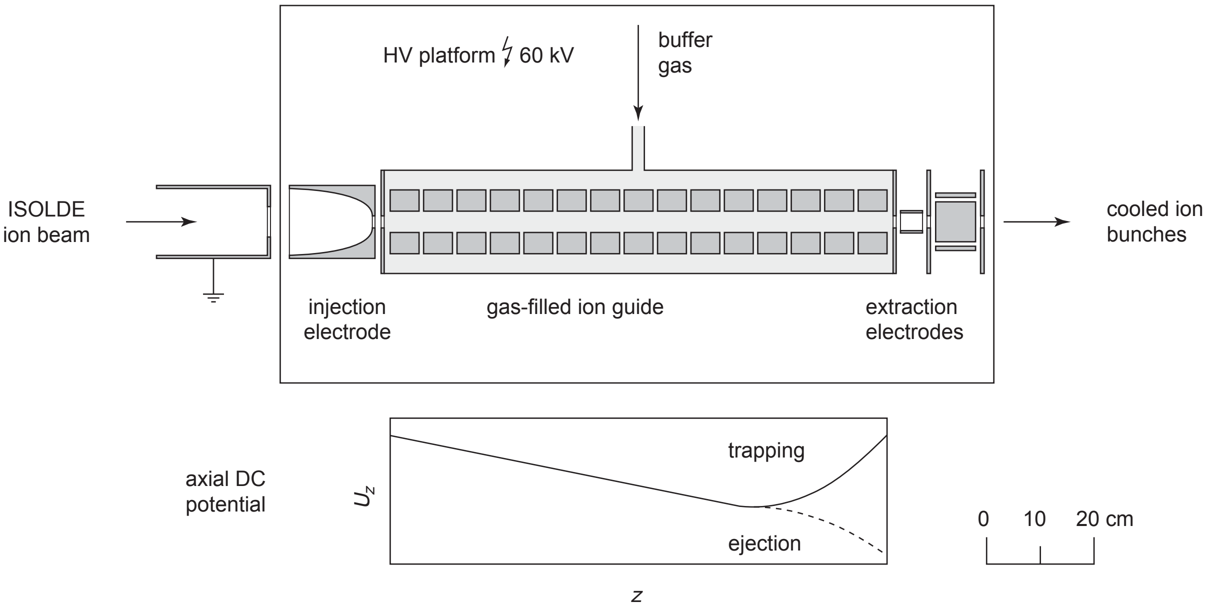

Figure 2.7 – Detailed sketch of the ISOLTRAP linear Paul trap. The device is placed on a HV platform, so that when entering the trap the ions are decelerated. The ions are radially confined by a radiofrequency quadrupole field, and cooled by collisions with the buffer gas. The axial potential is created by application of dc potentials on the segmented rods. The ions are accumulated near the end of the trap and re-accelerated after ejection. Figure from [Blaum 2006].

2.4 Electrostatic ion trap

Mass spectrometry experiments are often using magnetic fields to separate charged particles. However, it is well known that the time of flight of particles can also be used to perform mass separation.

In 1949, A. E. Cameron and D. F. Eggers have invented a new type of mass spectrometer, the "Velocitron" [Cameron 1948]. The idea of this device is to inject ion pulses of known energy in a long evacuated drift tube. Via the expression of the velocity:

$$v = \sqrt{\frac{2qE}{m}} \tag{2.21}$$

one can relate the charge q, the mass m, and the particle energy E. When arriving at the tube's end, there is a separation in time between the ion species proportional to: $L(\sqrt{m_1} - \sqrt{m_2})$, with L being the drift tube length and m_1 and m_2 the two different ion masses. Therefore, the longer the drift tube is, the easier it becomes to resolve the two different masses. For such mass spectrometry, the initial dispersion in time of the ion bunch has to be as low as possible. Otherwise a time of flight elongation of the ion bunch would inhibit the identification process. The Velocitron is an elegant tool to separate ions via their time of flight differences, but it is strongly limited in terms of available space. The Velocitron can not be indefinitely extended for obvious reasons.

In 1960 the "Farvitron" by W. Tretner [Tretner 1960] was introduced, it is a small high-vacuum gauge. Electrons ionize the residual gas, creating ions which are forced to oscillate between two plain electrodes by an inhomogeneous electrostatic field, see Figure 2.8. Similarly to a Penning trap, the ion motion can be resonantly excited by a sinusoidal driving field applied on the electrodes, so that the amplitude of their motion increase until they can reach the electrodes. The picked up current is thus proportional to the pressure of the residual gas. There is another mode of operation of the Farvitron: if several ion species are present in the residual gas, they are all ionized by the electrons, and via the oscillations between the electrodes, their flight paths are extended. After several oscillations a time of flight difference can be witnessed between the ion species. The first multiple path time of flight mass spectrometer was born.

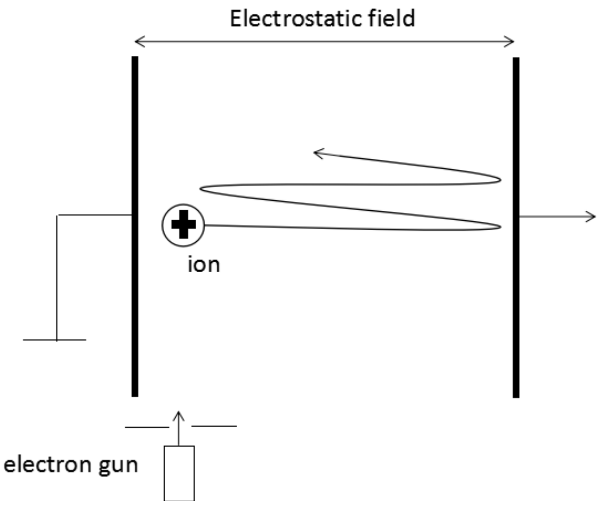

Figure 2.8 – Schematic representation of the Farvitron introduced in 1960 by W. Tretner.

In 1990, a description of the multi-reflection mass spectrometer was given by H. Wollnik and M. Przewloka [Wollnik 1990]. The key point of the instrument is that the ion flights have to be independent on the ion kinetic energy, as long as they have the same mass. Therefore, while being reflected, the fastest ions have to have an extended flight path, and the slowest ions have to have a reduced flight path. This is the so-called time of flight focusing.

An example of an electrostatic ion-trap is discussed in the following. It is a multi-reflection time of flight mass spectrometer (MR-TOF MS) [Wolf 2012a], which was developed and installed in 2010 at ISOLTRAP at ISOLDE/CERN. Since then, the high performances of such a device applied to nuclear physics led to the development of MR-TOF MS in several radioactive ion beam facilities worldwide.

2.4.1 The multi-reflection time-of-flight mass spectrometer

The MR-TOF MS described thereafter consists of a pair of electrostatic ion-mirrors and a field-free drift cavity, the in-trap lift electrode (see Figure 2.9). Once the ions have entered the device they undergo multiple reflections while being repeatedly focused by the ion mirrors. Once a mass separation in time of flight is obtained, the ions are released.

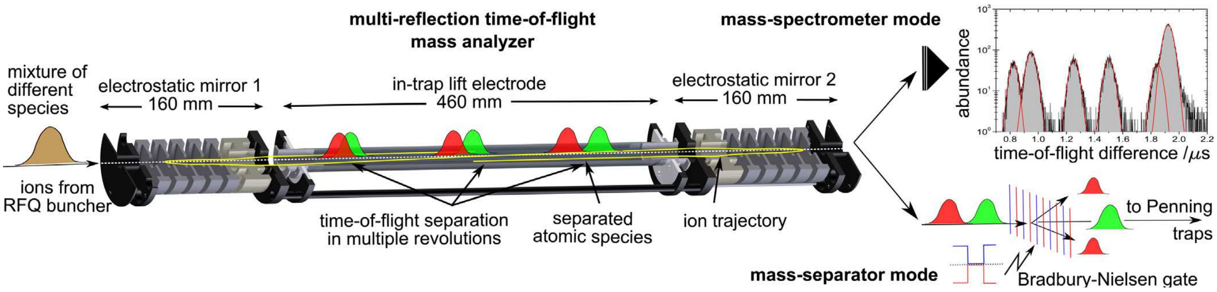

Figure 2.9 – Representation of the MR-TOF MS. The ions enter the electrostatic trap and undergo multiple reflections between two sets of mirror electrodes. After the mass separation, the ions are either detected by a microchannel plate (MCP) detector, for a TOF measurement (right top) or sent through a Bradbury-Nielsen gate (BNG) to select the species of interest (right bottom). The picture is from [Wolf 2013].

In-trap lift electrode and mirror voltages The usual method to inject (or eject) ions in an MR-TOF MS is to switch down the electric potentials of the entrance (or the exit) electrostatic-mirrors, respectively. However, the ISOLTRAP's MR-TOF MS proposes an alternative method. The potentials applied on the mirrors remain unchanged, only the in-trap lift electrode is switched [Wolf 2012a].

To enter the MR-TOF MS, the kinetic energy of the ions has to be slightly above the maximum of the electric potentials on the mirrors: $qU_{ions} > qU_{mirror}$ (Figure 2.10a). As a potential is set on the lift electrode (U_{lift}), when the ions enter this electrode, their relative kinetic energy is reduced by qU_{lift}. Then, the drift electrode is switched down to ground potential. The ions lose some of their kinetic energy, and are trapped between the mirrors (Figure 2.10b). To eject the ions the process is the opposite, the drift electrode is switched up (Figure 2.10c), giving enough kinetic energy to the ions to overcome the potential applied on the exit mirror (Figure 2.10d). One should note here that the ion kinetic energy can be influenced while the in-trap lift electrode potential is switched. To avoid any modifications on the ion energy when entering (or exiting) the MR-TOF MS, the in-trap lift electrode has thus to be switched when a distance of one to two times the drift-tube diameter is kept between the mirrors and the ions.

Once they are trapped, the ions are very sensitive to the potential defined by the ion mirrors. If the shape is slightly modified, the reflection is not optimized anymore. It results in a decrease of the mass resolving power of the MR-TOF MS (which can reach $\sim 10^5$). To keep the mass resolving power as high as possible, the voltages applied on the ion mirrors are supplied by high-precision modules, and thanks

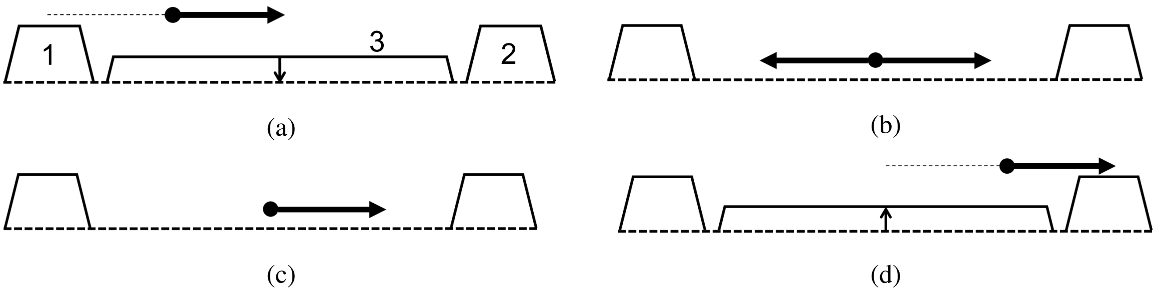

(a) (b) (c) (d)

Figure 2.10 – Schematic illustration of the in-trap lift technique. 1 and 2 represent the MR-TOF MS mirrors, 3 the in-trap lift electrode. To trap the ions inside the MR-TOF MS only the electric potential applied on the drift electrode is switched down. Once the ions have undergone enough reflections, the drift electrode is activated for the ion ejection. Adapted figure from [Wolf 2012a].

to the in-trap lift method the mirror potentials are never switched, avoiding voltage perturbations. Only the in-trap lift electrode is switched, via a solid-state MOSFET switch [Wolf 2012b].

Time focusing and energy dispersion Although the idea of the MR-TOF MS is really simple, the use of an electrostatic trap as a mass spectrometer requires serious developments. One can take as an example the time of flight focusing effect mentioned earlier. To have a time of flight difference only as a function of the ion mass, one needs an initial ion bunch with a time dispersion as low as possible and perfectly defined potential shapes for the ion reflections [Wolf 2012a].

To minimize the dispersion in time of the ion bunch, the ISOLTRAP's RFQ cooler buncher, which was delivering ion bunches with a longitudinal emittance of $\varepsilon_{long} \approx 10\,\mathrm{eV\mu s}$ [Herfurth 2001], had to be modified. The time structure of the bunches was reduced from 1 µs to 60 ns, thanks to the development of new radiofrequency switches [Wolf 2012a]. The energy dispersion was measured as $\Delta E^{Buncher} \approx 60\,\mathrm{eV}$. The longitudinal emittance has been decreased, being now $\varepsilon_{long} \approx 3.6\,\mathrm{eV\mu s}$ [Wolf 2012b].

2.4.2 Bradbury-Nielsen beam gate for mass selection

As shown in Figure 2.9, at the exit of the device a Bradbury-Nielsen gate (BNG) can be used together with the MR-TOF MS, allowing to mass select an ion species of interest. The BNG consists of two sets of parallel wires in a planar arrangement such that neighboring wires belong to different sets [Wolf 2012b]. When it is closed, voltages of alternating signs but equal values are applied to neighboring wires, it deflects the unwanted ions. When it is open, the voltages applied on the wires are switched off. A fast switch can open and close the gate fast enough, i.e. on the nanosecond scale, such that only the ions of interest can fly through the gate.

2.4.3 The MR-TOF MS: a versatile tool for nuclear physics

The MR-TOF MS was originally thought as an auxiliary device to enhance the mass purification capabilities for Penning-trap mass spectrometry. However, it became a tool of choice for ISOLTRAP and for the ISOLDE facility. Indeed, many advantages can be taken out from the use of this device. The measurement cycles are fast, typically $10-30$ ms, the mass purification with the MR-TOF MS is about one order of magnitude faster than a Penning-trap purification cycle, and a resolving power of 10^5 can be obtained, which is sufficient for most of the isobars.

Besides the purification, the MR-TOF MS can be used to perform mass measurements. In comparison to the TOF-ICR technique with a Penning trap, a mass measurement with the MR-TOF MS is more sensitive, i.e. less ions are needed. Indeed, it is not required to scan parameters to have access to the mass, the whole spectrum is obtained from a few injections.

The contaminants and the species of interest can be measured in the same spectrum, thus identified simultaneously. These contaminants do not perturb the measurements, at least for a reasonable number of ions inside the device. They can even be used to calibrate the device. More information on the different operation modes of the ISOLTRAP's MR-TOF MS can be found in [Wolf 2013].

Finally, the MR-TOF MS can also be used for other purposes, such as yield checks for ISOLDE (prior to an experiment) or it can be operated in collaboration with the RILIS experiment, [Marsh 2013], for laser spectroscopy experiments.

CHAPTER 3

Mass measurements of strontium and rubidium nuclei in the region A = 100

Contents

3.1 Introduction to nuclear physics

The atomic nucleus was discovered in the early twentieth century by Rutherford and his collaborators, Geiger and Mardsen [Geiger 1909, Rutherford 1911], and with it the nuclear physics as well as the search of a predictive model of nuclear structure were born. Nevertheless, no description and no prediction can be found with a lack of knowledge concerning the nature of the forces acting within the nucleus [Rutherford 1929]. The primary studies dedicated to the understanding of the nucleus were performed with scattering α-particles at different energies. As the investigation of the nuclear structure was ongoing, the notion of mass excess has emerged with the determination of the proton mass. It was shown that the proton mass is nearly 1 u when it is part of a nucleus, while when it is in its free state, the proton has a mass of ≈ 1.0073 u. The proton appeared to be lighter when bound. This mass loss was named the mass defect, it represents the fact that the mass $M(N,Z)$ of a nucleus is lower than the sum of the masses of its constituents. In the late twenties, when the nucleus was assumed being constituted of α-particles, protons and electrons, the mass defect was quantified. For example, an atom of mass 120, thus containing 120 protons, had an equivalent energy loss corresponding to the mass defect evaluated to 840 million volts [Rutherford 1929]. Many models with different approaches were attempted in order to explain this phenomenon. One of these models was proposed in 1930 by Gamow, the so-called liquid drop model [Gamow 1930]. In its first version the model compared the nucleus to a water-drop of incompressible nuclear matter constituted of α particles. It was defined as a trade-off between the long-range electromagnetic force and the relatively short-range nuclear force, in such a way that they can be assimilated to the surface tension forces in liquid drops of different sizes.

Two years later, the picture of the nucleus completely changed with the discovery of the neutron. This particle was postulated by Chadwick [Chadwick 1932] through the interpretation of some unexplained forms of gamma radiations. This discovery modified the picture of the nuclear constituents, leading to the modern view in which there are nuclear particles (nucleons) of two types: the neutrons and the protons. The introduction of the neutron initiated the development of the so-called new semi-empirical mass formula by Bethe and Weizsäcker in 1935 [Weizsäcker 1935, Bethe 1936]. This formula, which is presented in its generalized form in section 3.2.1, explains the mass defect via the notion of *binding energy*. According to the Einstein's famous equation [Einstein 1905]:

$$E = mc^2, \tag{3.1}$$

the missing mass is transformed into energy when the nucleus is formed. This energy is called binding energy $B(N,Z)$ and is linked to the mass of the atomic nucleus via the following formula:

$$M(N,Z)c^2 = N \cdot M_N c^2 + Z \cdot M_P c^2 - B(N,Z), \tag{3.2}$$

with M_N and M_P the neutron and proton masses, respectively, and c the speed of light.

The liquid drop model was reconsidered with the Bethe and Weizsäcker semi-empirical mass formula and led to a promising reproduction of nuclear binding energies. However, it was observed that when the number of neutrons and/or protons reaches certain values, now called magic numbers, an enhancement of the binding energy appears. The discovery of these numbers, which are: $2, 8, 20, 28, 50, 82, 126$, has highlighted the fact that the nucleus does not have only liquid drop characteristics, but also an internal structure coexisting with the liquid drop picture. Another fact encouraged this idea: an enhanced binding was also observed for nuclei having an even number of protons [Rutherford 1929]. This observation, reflected in the increased abundance of even nuclei, is called the pairing effect. However, in the liquid drop picture, a shell structure cannot be reproduced properly, it was thus interpolated from binding energy measurements of even-even nuclei. In analogy to the shell model in atomic physics a shell structure was thus proposed for the nucleus, based on the pairing association of two protons and two-neutrons, according to the Pauli principle.

The nuclear shell model - mentioned above - describes the nucleus as shells filled with protons and neutrons. It was developed in the fifties [Mayer 1949, Haxel 1949, Mayer 1950]. The proton and neutron shells are defined as independent from each other, and a shell closure corresponds to a number of nucleons equal to a magic number. The model reproduces the observed magic numbers with a potential defined as a three-dimensional harmonic oscillator plus a spin-orbit interaction. Not only the magic numbers could be successfully described with the model, but also other experimental observations; such as the spins, the magnetic moments and the isomers, see [Mayer 1950] for details.

However, deviations from the shell model were observed for nuclei having nucleon numbers midway between the magic numbers. In particular, a broad general increase in stability has been observed in the region $82 < N < 126$ [Hogg 1953]. It was associated to the phenomenon of "configuration mixing". At mid-shell closure, the nucleus gains binding energy by forming configuration states as a superposition of many independent-particle states. The dynamics of the protons and the neutrons are thus correlated, leading to extra binding gained via the configuration mixing. Therefore, the approximation of particles moving independently in the potential breaks down and the nuclear structure becomes linked to the collective motions of all nucleons.

In the nuclear shell model the configuration mixing can be considered by adding a residual nucleon-nucleon interactions "on top" of the single-particle potential, or can be incorporated from the beginning. Another approach which allows considering the configuration mixing was developed, the Hartree-Fock model. In this model, the nucleons are also treated as independent particles, but a self-consistent mean field is constructed from the nucleon-nucleon interactions. In the following, the different models introduced in this section are discussed in more detail. A particular attention will be given in the treatment of mid-shell nuclei, and their increase of stability, which can be explained as the result of deformation.

3.2 The concept of nuclear deformation

The different models dedicated to the description and the prediction of the nucleus are based on three kinds of approaches. The liquid drop model is a macroscopic model, as it focuses on macroscopic aspects of the nucleus, like the surface tensions. The addition of microscopic terms in macroscopic models, such as shell corrections, has led to the development of macroscopic-microscopic models. A more fundamental description of the nucleus is given in the microscopic nuclear shell model and Hartree-Fock method.

The qualitative properties of nuclei along or close to the magic numbers are rather easily reproduced by the three approaches. However, adding or removing only a few protons or neutrons can completely change these properties and the models can no longer reproduce the experimental results. In the incoming sub-sections the macroscopic and microscopic approaches, as well as a combination of both, will be discussed in more detail. For each approach, a particular attention is given to the method used to describe the shape evolution of nuclei.

3.2.1 The nuclear deformation with a macroscopic approach

As already mentioned in section 3.1, the semi-empirical mass formula from Bethe and Weizsäcker is a key point for the liquid drop model. The formula was slightly modified over the years to its present form [Bethe 1936, Myers 1966, Lunney 2003]:

$$E = a_{vol}A - a_{sf}A^{2/3} - \frac{3e^2}{5r_0}\frac{Z^2}{4\pi\varepsilon_0}A^{-1/3} + (a_{sym}A + a_{ss}A^{2/3})I^2. \tag{3.3}$$

The nuclear internal energy E is equivalent to the binding energy: $E \equiv -B(N,Z)$ and $I = (N-Z)/A$ is the charge asymmetry parameter. The first term is a volume term. It takes into account the increase of binding energy as a function of the nucleon number. The second term considers the decrease of binding energy due to the less bound nucleons lying at the surface of the nucleus. The third term represents the repulsive influence of the infinite-range Coulomb force. The fourth term, with a_{sym} the symmetry coefficient and a_{ss} the surface-symmetry term, takes into account the fact that the neutrons and protons are composite particles, and that the nucleus minimizes its energy by equilibrating the number of protons and neutrons (because of the Pauli principle). This fourth term is a correction to the volume and surface term. In its formula, Weizsäcker also gave a possibility for a term correcting the pairing effect by interpolation [Weizsäcker 1935]. However, it is already a microscopic correction that will be discussed in section 3.2.2. The parameters a_{vol}, a_{sf}, a_{sym}, a_{ss} and r_0 from equation (3.3) are fixed by fitting them to the known $N, Z \geqslant 8$ masses included in the AME 2012 [Wang 2012] (for the most recent fit).

The liquid drop model considers that a nucleon mean free path in the nucleus is on the order of the nuclear size. Furthermore, the nucleon repartition is defined as homogeneous in the nucleus. Therefore, a well bound nucleus can be easily imagined having a spherical shape. It is the case for nuclei having a magic number of protons and neutrons, for example. However, it has been shown experimentally that a non magic nucleus, therefore one which is less bound, has a deformed shape in order to minimize its potential energy. In other words, a non magic nucleus can undergo dynamical shape or surface oscillations to minimize its potential energy. In the framework of the liquid drop model, such evolutions of the nuclear shape can be expressed via a parametrization of the nuclear surface by the length of the radius vector pointing from the origin to the surface [Ring 2004]:

$$R(\theta,\phi) = R_0 \left(1 + \alpha_{00} + \sum_{\lambda=1}^{\infty} \sum_{\mu=-\lambda}^{\lambda} \alpha^*_{\lambda\mu} Y_{\lambda\mu}(\theta,\phi)\right), \tag{3.4}$$

with R_0 the radius of the sphere, λ the deformation mode (or degree) and μ the order of the deformation. For $\lambda = 0$ it is a monopole deformation. When $\lambda = 1$ the whole system can translate, only for small deformations. When $\lambda = 2$, the system goes through ellipsoidal shapes, thus quadrupole deformation. Higher values of λ describe higher orders of deformation, and will not be considered here. The discussion will now remain on small quadrupole deformations. α_{00} and $\alpha_{1\mu}$ are omitted [Ring 2004].

Hence, when $\lambda = 2$, one can distinguish five parameters $\alpha_{\lambda\mu}$. After a transformation in the body-fixed frame described by the Euler angles the five coefficients $\alpha_{2\mu}$ are reduced to three real independent variables a_{20} and a_{22}, with $a_{22} = a_{2-2}$, which together with the Euler angles give a complete description of the system. The two intrinsic variables of the deformation a_{20}, a_{22} and a_{2-2} can be re-expressed a function of the Hill-Wheeler [Hill 1953] coordinates β and γ ($\beta > 0$):

$$\begin{aligned} a_{20} &= \beta \cos\gamma, \\ a_{22} &= a2-2 = \frac{1}{\sqrt{2}} \beta \sin\gamma, \end{aligned} \tag{3.5}$$

from which we have

$$\sum_{\mu} |\alpha_{2\mu}|^2 = a20^2 + 2a_{22}^2 = \beta^2, \tag{3.6}$$

where β is the axial elongation and γ the triaxiality parameter. The nuclear shape evolution in the β, γ plane is shown in Figure 3.1. The γ values of 0°, 120° and 240° correspond to the prolate shape of a nucleus. For $\gamma = 60°$, 180° and 300° the nucleus has an oblate shape. When γ has different values than the ones previously mentioned, the nucleus shape is triaxial. One can notice the discrete symmetry which allows to change the axis without modifying the shape. Therefore, the interval $0 < \gamma < 60°$ is enough to illustrate all the quadrupole shapes of the nucleus. More detailed information about the nuclear shape deformation studies within the liquid drop model can be found in [Ring 2004].

3.2.2 The nuclear deformation with a macroscopic-microscopic approach

Probably the most famous macroscopic-microscopic model is the finite range droplet model (FRDM). It is based on the liquid drop model (equation (3.3)) but includes several strong enhancements. They consist on modifications of the macroscopic part of the model and the introduction of shell corrections.

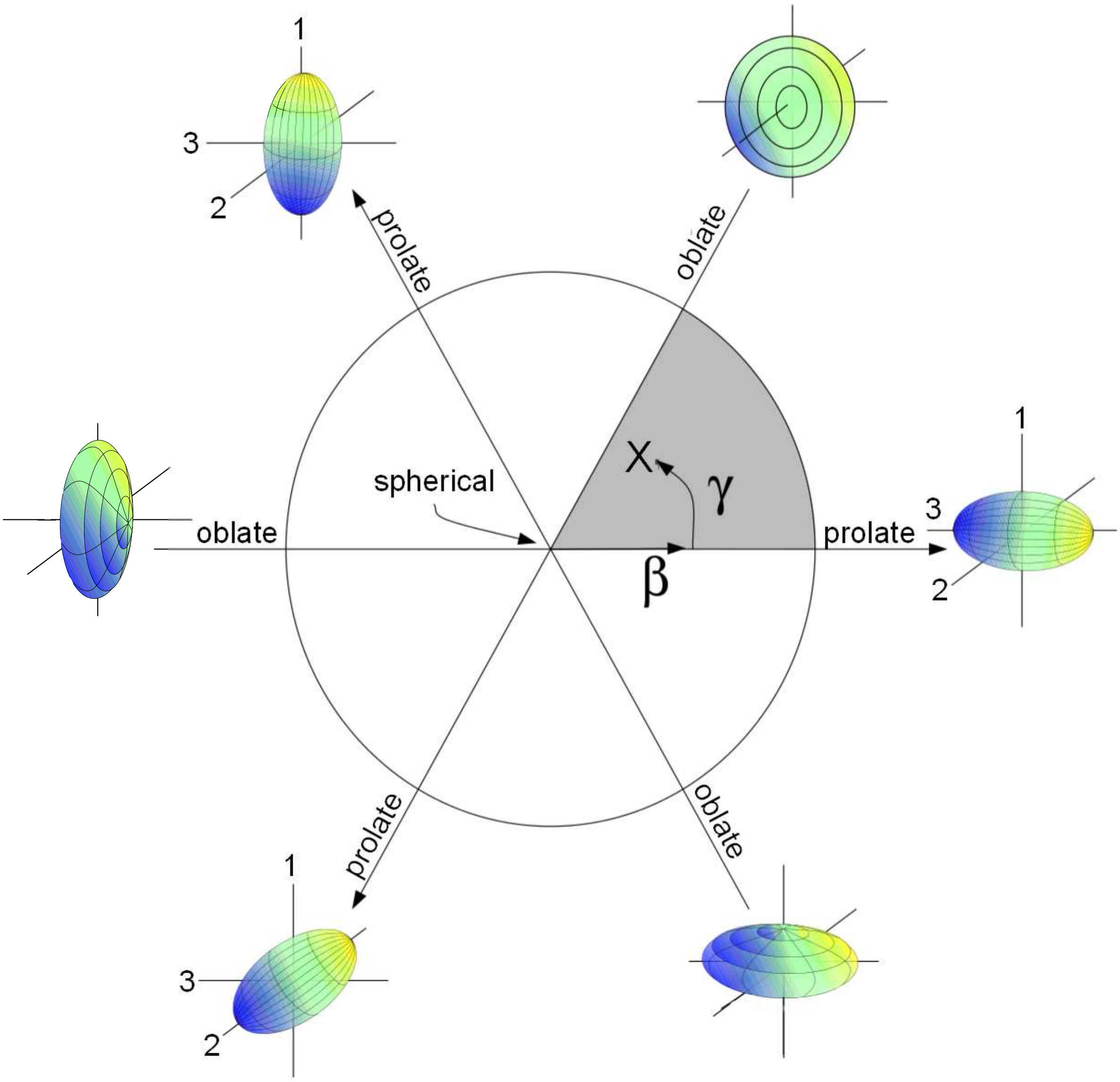

Figure 3.1 – Representation of the nuclear shape evolution in the β, γ plane. β is the axial elongation and γ is the triaxiality parameter. Figure adapted from [Clément 2006]

There are three macroscopic modifications: First, the incompressibility of the nuclear matter is not considered to be infinite anymore. This modification has a strong impact on the models, resulting in a new mass formula which also includes deformations factors [Myers 1974]. The second modification named "finite range" concerns the nucleon-nucleon interaction. The short-range character of the interaction is taken into account and affects the surface energy [Möller 1981]. The last modification is a phenomenological compressibility term, which was introduced to correct the overestimation of the central density [Treiner 1986].

The shell corrections are introduced using the Schrödinger equation for a single particle in a single-particle field, expressed for the FRDM model as follows:

$$U = V_0 + V_{so} + V_{coul}. \tag{3.7}$$

V_0 is a spin-independent term, V_{so} a spin-orbit interaction term and V_{coul} a Coulomb interaction term. In addition, corrections for the pairing interaction and an adapted Wigner term are also added. The latter comes from the Wigner effect [Wigner 1937], which states that there is an enhanced binding energy for nuclei with $N \approx Z$.

3.2.3 The nuclear deformation with a microscopic approach

In microscopic nuclear-structure calculations, the Schrödinger equation:

$$H|\Phi\rangle = E|\Phi\rangle, \tag{3.8}$$

has to be solved for the many-body Hamiltonian:

$$H = \sum_{i=1}^{A} t(i) + \sum_{i<j}^{A} V(i,j), \tag{3.9}$$

where the terms $t(i)$ correspond to the kinetic energy of the nucleons, and the terms $V(i,j)$ to the nucleon-nucleon interaction, depending on the spatial, spin and isospin coordinates of the particles i and j [Ring 2004]. However, this many-body problem can only be solved for the lightest atomic nuclei, and at a great computational cost. Therefore, the only way to describe the nuclear structure microscopically for every nucleus is by defining an effective nuclear potential. It is the method used in the nuclear shell model [Mayer 1964] and the Hartree-Fock-Bogoliubov approach [Bender 2003], which are discussed in the following. The starting point of both models is to consider the interaction of a nucleon with all the other protons and neutrons constituting the nucleus, as being approximated, at least to the first order, by a mean-field, i.e. a single-particle potential. This approximation is enough to explain qualitatively some of the observed nuclear properties. However, the correlations due to the nucleon-nucleon interactions are too important, and they are missing in this "naive" independent-particle picture of the nucleus.

The nuclear shell model The nuclear shell model, which was developed in analogy to the shell model of atomic physics by M. Goeppert-Mayer and H. Jensen could reproduce the shell closures via the introduction of an energy correction to the single-particle energies associated to the spin-orbit coupling. M. Goeppert-Mayer and H. Jensen have shared the Physics Nobel Prize in 1963 for their work [Mayer 1964].

The shell model takes into account explicitly the nucleon-nucleon interaction but restricts itself to the nucleons outside a certain inert core, the so-called valence nucleons. The core (typically, a doubly-magic nucleus) being considered as inert, the nucleons occupy the single-particle states with probability one. With the shell model, the Schrödinger equation is thus solved for the part of the Hamiltonian corresponding to the valence nucleons.

The shell model computed with a spherical potential reproduced very well the experimental data for nuclei having closed - or nearly closed - shells. However, for mid-shell nuclei only the assumption of a deformed single particle potential gives results which reproduced the data [Rainwater 1950, Bohr 1951]. The introduction of deformed potentials has allowed the description of some previously unexplained experimental facts, such as the existence of rotational bands and large quadrupole moments [Ring 2004].

There are two widely used approaches to describe a deformed nucleus. One is the deformed Woods-Saxon potential:

$$V_{central}(\vec{r},\beta) = \frac{V_0}{1 + e^{\frac{dist_{\sum}(\vec{r},\beta)}{a}}} \tag{3.10}$$

where $dist_{\sum}(\vec{r},\beta)$ is the distance $\vec{r}$ between a point and the nuclear surface $\sum$, and β is the deformation parameter [Cwiok 1987]. The Woods-Saxon approach has been used for the first time in the region $A \approx 100$ in 1985 by Nazarewicz *et al.* [Nazarewicz 1985].

The second approach is the Nilsson deformed model, in which the potential is chosen as an anisotropic harmonic oscillator plus two terms [Nilsson 1955]. The first one gives the strength to the spin orbit forces and the second one is proportional to the square of the angular momentum. The resulting potential is:

$$V(\vec{r}) = \frac{m}{2}((x\cdot\omega_x)^2 + (y\cdot\omega_y)^2 + (z\cdot\omega_z)^2) + C\vec{l}\cdot\vec{s} + D\vec{l}^2, \tag{3.11}$$

where the rotational frequencies ω_x, ω_y and ω_z describe the nuclear deformation, C is related to the spin orbit force and D to the angular momentum. The resolution of the Schrödinger equation with this potential allows to determine the single particle energy at the corresponding deformation. The results can be plotted as a function of the deformation, the so-called Nilsson diagrams.

Hartree-Fock approach At first formulated for electrons in the Coulomb potential of the atomic nucleus, the Hartree-Fock (HF) approach was also developed in nuclear physics. For this method, the nucleons are approximated as independent single particles (similarly to the shell model). Here only the two-body interactions are considered. The three-body interaction can also be added to the model, but for clarity, it is not taken into account here. All the interactions are then averaged to form a mean field. However, to determine this mean field from the two-body interactions, and not the real many-body interactions anymore, one has to use an effective two-body interaction in the Hamiltonian:

$$H = \sum_{i=1}^{A} t(i) + \sum_{i<j}^{A} V_{ij}^{\text{eff}}, \tag{3.12}$$

with V_{ij}^{eff} the effective interaction. The many-body wave function Ψ is thus approximated by a product Φ of A single particle wave functions ϕ_i. The nucleons are fermions, therefore, the wave function has to be antisymmetric with respect to the exchange of two particles according to the Pauli principle. This is ensured by using the Slater determinant as an ansatz:

$$\Psi \to \Phi = \det\{\phi_i\} \tag{3.13}$$

The resolution of the Schrödinger equation with the HF method requires the variational principle, the ground-state energy E_0 is minimized by a variation of Φ:

$$\frac{\langle\Phi|H|\Phi\rangle}{\langle\Phi|\Phi\rangle} \geqslant E_0. \tag{3.14}$$

The use of the variational method is possible due to the equivalence between the Schrödinger equation and the condition that the expected value of the energy is stationary with respect to a small variation of Φ. This means that by minimizing E_0 one obtains an approximation of the correct ground-state energy. In the variational approach, the Schrödinger equation is thus re-formulated by means of a functional derivative δ to:

$$\frac{\delta}{\delta\Phi}\langle\Phi|H^{\text{eff}}|\Phi\rangle = 0. \tag{3.15}$$

The substitution of the Slater determinant, equation (3.13), into the re-formulated Schrödinger equation, equation (3.15), gives the so-called HF equations:

$$h_i(\phi_i)\phi_i = e_i\phi_i, \tag{3.16}$$

where h_i is the single particle Hamiltonian and e_i is the single particle energy. h_i contains the kinetic energy t and the self-consistent field Γ, which is the optimal approximation of the given interaction V_{ij}^{eff}

to an independent-particle potential. Γ is the average potential felt by one particle through interactions with all other particles, also called the mean-field potential. The HF equations are solved iteratively, as they are non-linear (an analytical solution is thus not possible) and the single-particle Hamiltonian h_i is a function of the single-particle wave function ϕ_i (due to the self consistent mean field). The iterative process goes as follows: one selects an ansatz for ϕ_i, calculates h_i and solves the resulting Schrödinger equation. It gives an improved ϕ_i. The procedure can be started anew until the change from one step to the next one becomes smaller then a predefined ε:

$$\delta\langle\Phi|H|\Phi\rangle < \varepsilon, \tag{3.17}$$

which acts like a termination condition. A self-consistence solution is obtained. A detailed demonstration of the HF method can be found in the book from P. Ring and P. Schuck [Ring 2004].

The HF method is able to reproduce ground state properties of spherical nuclei (with closed shells). However, for mid-shell nuclei, a slightly deformed density distribution is obtained: oblate or prolate. This effect conducts to a deformed mean-field. As long as it concerns only a few external particles, one can still compute the method and expect reasonable results by taking into account the correlation caused by the interaction of the external particle with the other nucleons. However, if the number of external particles increases, one has to consider the pairing interactions in the HF description.

The pairing interaction The HF approach is a powerful model which reproduces nicely the properties of spherical nuclei. However, this model takes into account only the long-range part of the nucleon-nucleon interaction, the so-called particle-hole interaction. The short-range part of the interaction, which causes pairing correlations, is not present in the pure HF picture. There is however significant experimental evidences for its existence, such as the difference in excitation spectra between even-even and odd nuclei, the odd-even staggering of binding energies and the moments of inertia of rotational bands [Ring 2004]. In order to consider the pairing effect, a theory was developed for nuclear physics in analogy to the Bardeen, Cooper and Schrieffer (BCS) method used to determine the ground-state of a superconductor [Bardeen 1957].

Similarly to the HF theory, the BCS theory does not provide an exact solution, but it can also be derived from a variational principle. Likewise the Slater determinant for the HF theory, an ansatz is needed in the BCS theory which explicitly makes pairs of single particles appearing in the expression of the many-body wave function. The latter is thus no longer a state of independent particles. The variational method is used to minimize the ground state energy, but with an additional constraint on the particle number, which ensures that the nucleus has the correct mean number of protons and neutrons.

The BCS wave function obtained from the variational principle can be written as a product of quasi-particle states, which can be related to the particle states via the so-called BCS transformation [Ring 2004]. A new type of fermion particle, the quasi-particle, are thus used to describe the particle correlations while still approximating the nuclear ground state by a product state. Therefore, by using the same approach as the HF approach, one can solve the BCS equations with quasi-particles and extract a single quasi-particle potential, the pairing field Δ.

The BCS theory presented here takes into account all the nucleons, and can be generalized for different types of interaction, similarly to the pure HF method. However, the pairing field Δ treats only the short-range part of the nucleon-nucleon interaction. Therefore, a generalized model is needed in which the HF and the BCS approaches, i.e. the long- and short-range parts of the interaction are combined.

The Hartree-Fock-Bogoliubov approach As seen in the previous paragraphs, nuclear properties can be described with a microscopic approach, in terms of independent particles moving in a self-consistent mean-field; the HF approach. The BCS model takes into account additional correlations in order to treat the mid-shell with a generalized single-particle picture by introducing the quasi-particle fermions. The Hartree-Fock-Bogoliubov (HFB) model generalizes and unifies both methods. The Bogoliubov quasi-particles are defined more generally than the BCS particles, by the so-called Bogoliubov transformation [Ring 2004]. In the HFB theory, the ground-state wave function is thought as the most general product state of independent Bogoliubov quasi-particles. With the energy minimization, via the variational method, one obtains the HFB equations:

$$\begin{pmatrix} h-\lambda & \Delta \\ -\Delta & -h^{*}-\lambda \end{pmatrix} \begin{pmatrix} U_k \\ V_k \end{pmatrix} = \begin{pmatrix} U_k \\ V_k \end{pmatrix} E_k \tag{3.18}$$

where h is the single-particle Hamiltonian from the HF theory which contains the self-consistent field Γ. λ is the chemical potential determined by the particle-number condition, and Δ is the pairing field. For the full demonstration, see for example [Ring 2004]. This model allows to reproduce the ground state properties of spherical and deformed nuclei. It can also be used for the description of excited states such as pure quasi-particle excitations or rotational states in well-deformed nuclei.

The nucleon-nucleon effective interactions The nucleon-nucleon interactions used to substitute the many-body problem in the Hamiltonian are various. In this work will be mentioned two effective interactions, the Skyrme and the Gogny interactions. The Skyrme interaction includes a two- and a three-body interaction term. More developed than the Skyrme interaction, the Gogny interaction includes a non-zero range force which allows to better calculate the pairing interaction, but, in return, it requires more computational power [Dechargé 1980]. Different parameterizations of these interactions will be used, see section 3.7.1.

3.3 Overview of the region $A \approx 100$

One of the very important regions of nuclear deformation is located on the nuclear chart around mass number $A \approx 100$, between the isotopic chains of krypton ($Z = 36$) and molybdenum ($Z = 42$). This region is particularly interesting due to the sudden onset of deformation at $N = 60$ making it one of the most dramatic shape changes on the nuclear chart.

A first experimental hint of the deformation of these nuclei was given in the work of S.A.E. Johansson [Johansson 1965]. Via gamma spectroscopy studies of ^{252}Cf fission fragments, S.A.E. Johansson originally intended to study the rare-earth region, another famous region of nuclear deformation at $A \approx 150$, which presents rotational-like spectra in the emission of γ-rays. During the measurement it was found out that the gamma spectra from fragments within a mass range $92 < A < 110$ were showing similarities with those from the rare-earth region fragments. More especially, the γ emission from some of the $A \approx 100$ fragments presented rotational-type spectra, similarly to the γ spectrum from the rare-earth fragments. Furthermore, the energies of the first 2^+ states of even-even nuclei with $Z = 42 - 48$ were also in favor of a nuclear deformation in this region. The mass region $A \approx 100$ was thus identified as a new region of stable deformation. Since this discovery, considerable efforts have been made, both experimentally and theoretically, to understand the properties of the region [Cheifetz 1970, Hotchkis 1991, Ebert 2012].

3.3.1 Experimental evidence

3.3.1.1 γ-ray spectroscopy

Rotational bands A few decades ago the new region of deformation at $A \approx 100$, which was found to be a strong prolate deformation zone ($\beta_2 \simeq 0.3 - 0.4$), has been mainly investigated by studying the rotational bands of mass-separated fragments from induced and spontaneous fission, see the following references [Wohn 1983, Wohn 1986, Wohn 1987, Petry 1988, Lhersonneau 1990, Lhersonneau 1995] as examples. Out of these studies was extracted information about the lowest levels of rotational bands (mainly for even-even nuclei), which is a clear indication of deformed nuclear structure. It was also demonstrated that the deformation continues with the increase of neutron number.

Low-lying excited states The spherical-like and ellipsoidal-like low-lying nuclear structure can be differentiated in even-even nuclei by the energy of their first excited state E(2_1^+), and the ratio E(4_1^+) / E(2_1^+), respectively [ENS 2016, Wang 2016]. These quantities were determined in the region $A \approx 100$. The energies of the first 2_1^+ state E(2_1^+) and the ratios $R_{4/2} = E(4_1^+) / E(2_1^+)$ are shown in Figure 3.2a and Figure 3.2b, respectively. The abrupt transition observed in these graphs at $N = 60$ is synonym to the sharp transition from spherical to highly deformed ground states. The transition in the energy of the first excited states E(2_1^+) is characterized by a sudden decrease. Unlike the E(2_1^+) plots, the transition in the ratio $R_{4/2}$ is visible via a rapid increase at $N = 60$ towards the value corresponding to a rigid quantum-mechanical rotor of 3.33. There is no clear indication in favor of a deformation in Figure 3.2a and Figure 3.2b for the krypton isotopic chain.

3.3.1.2 Mass measurements

The two-neutron separation energy S_{2N} represents the binding energy difference between two isotopes having N and $N-2$ neutrons, respectively:

$$S_{2N} = -M(A,Z) + M(A-2,Z) + 2M_N. \tag{3.19}$$

From the two-neutron separation energy, one can represent the mass surface evolution of an isotopic chain. This knowledge generally extends further than other observables in a given region, thus offering hints at possible structure evolutions. Therefore, mass measurements are important tools to probe regions of deformation.

In Figure 3.2c is represented the S_{2N} evolution in the region $A \approx 100$. The sharp decrease in the S_{2N} values at $N = 50$ is due to the magic number 50, synonym to an enhancement of stability, which can be interpreted as passing from removing neutrons from one shell to removing neutrons from shell of higher energy (hence less bound). On the contrary, the sudden jump at $N = 60$ represents an increase of the binding energy due to the appearance of deformation.

The mass measurements performed in this region show that the most sudden onset of deformation is observed for the Zr, Y and Sr cases. Furthermore, once the deformation is established at $N \approx 60$, the deformation is preserved for a higher neutron number. No further change in the isotopic chain trends is visible in Figure 3.2c. The upper limit of the deformed region is known as being the molybdenum isotopic chain as its trend is rather continuous instead of exhibiting sudden increase. One should note here that the smoothness of the trend is not a sign of sphericity, as it can equally signify a gradual onset of deformation. The isotopic chain at $Z = 44$ (ruthenium) does not show signs of deformation. The recent Penning-trap measurement of ^{96}Kr and ^{97}Kr [Naimi 2010b] seems to define the krypton isotopic chain as the lower limit of the region of deformation.

Most of the data originate from Penning-trap mass measurements [Hager 2006], with the most recent results addressing the low-Z border of the region, see [Naimi 2010b, Simon 2012, Manea 2013, Klawitter 2016].

3.3.1.3 Mean square charge radii measurements

The mean square charge radii are obtained by laser spectroscopy from isotope-shift measurements, see [Blaum 2013]. Since the contributions from the neutron distribution are excluded in the mean

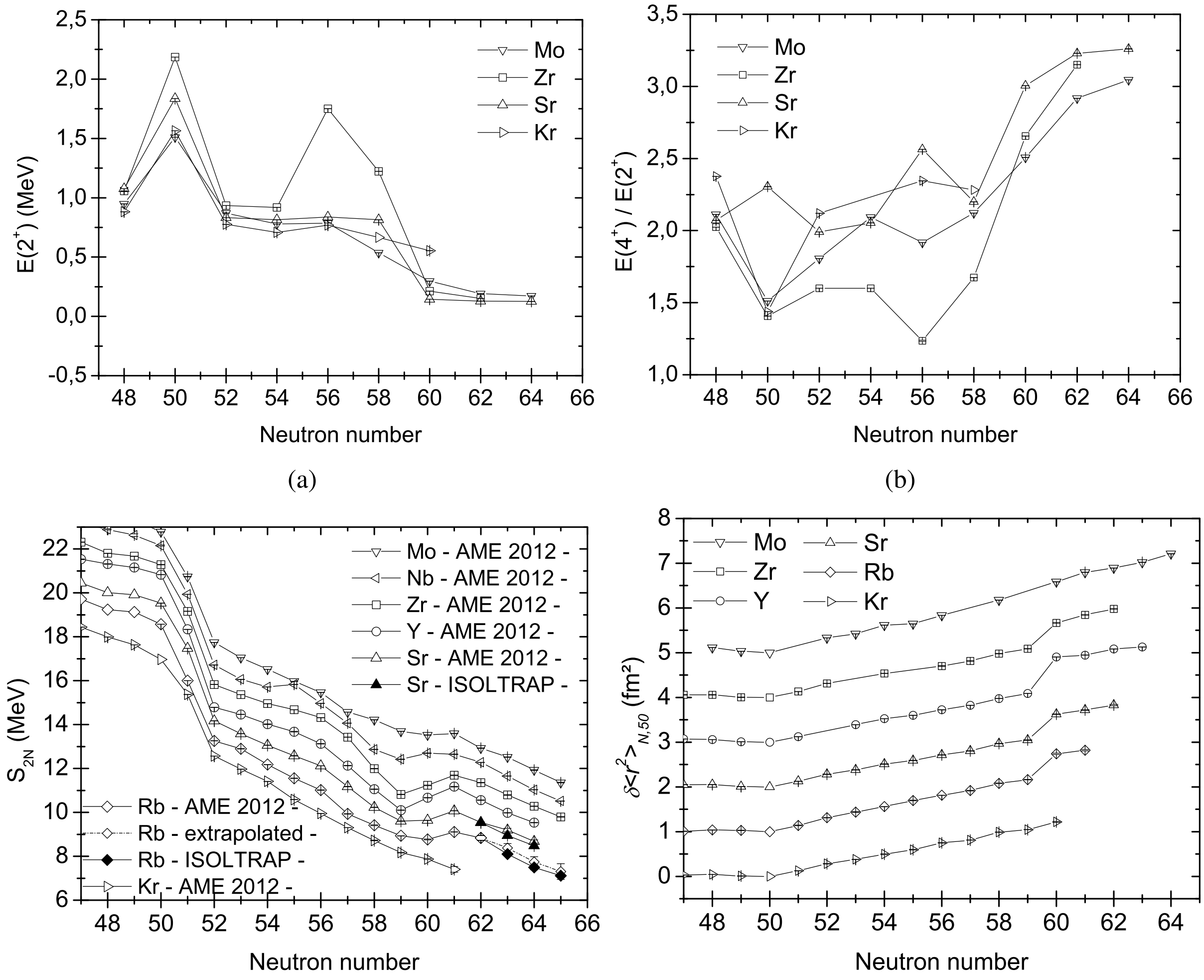

(a) (b)

(c) (d)

Figure 3.2 – Representation of nuclear data for the Mo, Nb, Zr, Y, Sr, Rb and Kr isotopic chains in the region $A \approx 100$. In (a) are represented the energies of the first 2^+ excited states of the even-even nuclei in the Mo, Zr, Sr and Kr isotopic chains. In (b) are plotted the energy ratios between the first 4^+ and 2^+ excited states in the Mo, Zr, Sr and Kr isotopic chains. The data are mainly from [ENS 2016], apart the one concerning ^{102}Sr for which the energies of the first 4^+ and 2^+ excited states are from [Wang 2016]. In (c) the two-neutron separation energy S_{2N} plots of the isotopic chains are represented. The data are from [Wang 2012], shown with empty points and half-empty points for the experimental and extrapolated values, respectively, and ISOLTRAP, shown with solid points. In (d) are shown the mean square charge radii. The Nb isotopic chain is not represented in the mean-square charge radii plot because of a lack of experimental data in the region of interest [Keim 1995, Thibault 1981, Buchinger 1990, Lievens 1991, Cheal 2007, Campbell 2002, Angeli 2013]. Each isotopic chain is set apart by 1 fm^2 for clarity.

charge radii variations, these results cannot be considered as an absolute measurement of the nuclear deformation. However, the evolution of the mean square charge radii along an isotopic chain gives additional hints for possible nuclear deformations. The mean-square charge radii of the isotopic chains around $A \approx 100$ are shown in Figure 3.2d as differences from the isotope having $N = 50$. The values are taken from [Keim 1995, Thibault 1981, Buchinger 1990, Lievens 1991, Cheal 2007, Campbell 2002, Angeli 2013]. Similarly to the S_{2N} plot, a sudden increase is visible at $N = 60$ in Figure 3.2d, except in the krypton isotopic chain, which supports the conclusion from the mass measurement. Again the krypton isotopic chain can be considered as the lower limit of the region of sudden shape transition.

3.3.2 Theoretical description

The sudden onset of deformation at $N \approx 60$ has been firstly studied via microscopic calculations, nuclear shell model and HFB, on zirconium isotopes [Federman 1977, Federman 1978, Federman 1979] by P. Federman and S. Pittel. An inert core of Sr was assumed with a restricted valence space. For the calculations via the shell model, the inert core was chosen to be ^{88}Sr, see Figure 3.3, while for the HFB calculations, the inert core was ^{94}Sr.

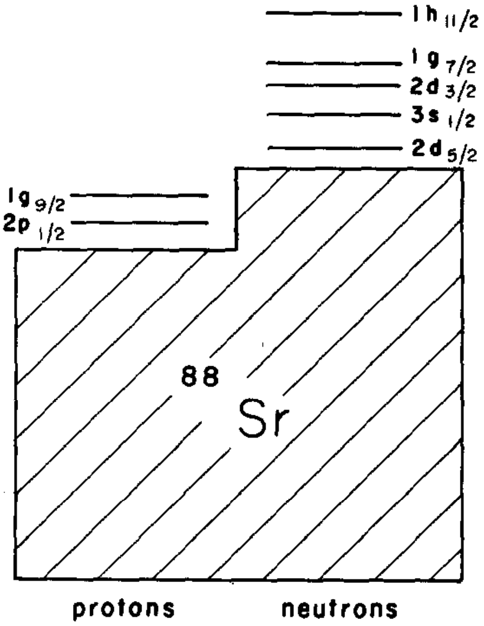

Figure 3.3 – Single-particle levels used to describe the Zr-Mo region. Figure from [Federman 1977].

P. Federman and S. Pittel have interpreted the deformation as the result of the proton-neutron correlation between the $\pi 1g_{9/2}$ and $\nu 1g_{7/2}$ spin-orbit partner orbitals. However, they also stated that beyond $A = 104$ the $\nu 1g_{7/2}$ orbital seems to play a gradually less important role in producing deformation, while the $\nu 1h_{11/2}$ needs to be included in the calculations in order to reproduce the features of the deformed orbitals [Federman 1978].

HFB calculations were performed by A. Kumar and M. R. Gunye [Kumar 1985] with an inert core of ^{60}Ca and thus larger valence space (compared to the work of P. Federman and S. Pittel). The larger valence space helped to reproduce the trend of the experimental data in ^{98}Sr, ^{100,102}Zr and ^{104,106}Mo. It was thus concluded that ^{88}Sr and ^{94}Sr as inert cores were not satisfying. Even if the energy levels were not well reproduced with the ^{60}Ca inert core, the increase of the valence space helped to reproduce the sudden onset of deformation.

In the 90's global FRDM calculations with a folded Yukawa single particle potential have been performed [Moller 1995]. A gradual shape transition, from spherical to well-deformed, in the range $N = 54 - 64$ was exhibited. The onset of deformation was not perfectly reproduced, however, after the transition gap ($N \geqslant 60$) a better agreement with the experimental data was found.

The Skyrme and the Gogny nucleon-nucleon interactions are continuously improved in order to achieve better agreement between the data and HFB calculations. The most recent parameterizations of the Skyrme interaction are UNEDF0 (adjusted on spherical and deformed nuclei) [Kortelainen 2010], and UNEDF1 (optimized also on the excitation energies of fission isomers) [Kortelainen 2012]. The

D1S parametrization of the Gogny interaction [Dechargé 1980, Berger 1991] was used for a beyond mean-field calculation using a five-dimensional collective Hamiltonian (5DCH) [Clément 2016]. A comparison between these recent HFB calculations and the nuclear data in the region $A = 100$ is presented in section 3.7.1.

The regions of shape transition are usually subject to shape coexistence. According to the definition given by J. L. Wood and K. Heyde [Heyde 2011], the shape coexistence is the result of the equilibrium between the tendencies to stabilize the nucleus with spherical or ellipsoidal shapes. In a shape coexistence framework, the nucleon configurations (orbitals) are almost degenerated which leads to the observation of several shapes in a short energy range. In the region of deformation $A = 100$, the presence of shape coexistence has been proven for the $N = 58$ isotones ^{96}Sr and ^{98}Zr [Wu 2004, Simpson 2006], for example. According to the mean field calculations of S. Hilaire and M. Girod [Hilaire 2007], using a HFB approach based on the Gogny effective nucleon-nucleon interaction for axially symmetric nuclei, a scenario of shape coexistence for the Rb isotopic chain is also possible.

3.4 The ISOLTRAP mass spectrometer

The masses of the neutron rich $^{100-102}$Sr and $^{100-102}$Rb presented in this work were measured with the ISOLTRAP mass spectrometer at ISOLDE [Kugler 2000]. Two of the ISOLTRAP traps were used for the measurements, the precision trap [Mukherjee 2008] for the strontium masses, and the multi-reflection time-of-flight mass spectrometer (MR-TOF MS) [Wolf 2013] for the rubidium masses. In the following, the ion production, the experimental setup and the results will be presented.

3.4.1 Beam production at ISOLDE

In general there are two main methods to produce radioactive ion beam (RIB); the isotope separation on line (ISOL) and the in-flight technique. For both methods a high-intensity primary beam, produced by an accelerator, is sent on a target. The interactions between the beam and the target induce nuclear reactions, which results in the production of radioactive ions. With both the ISOL and in-flight methods, nuclei over the whole mass range can be produced.

3.4.1.1 Introduction to beam production techniques

The ISOL production technique The ISOL-method (also called precision frontier) consists of sending a primary beam on a thick hot target. From the resulting nuclear interactions, neutral products are created, which are extracted by the process of thermal diffusion. The chemical properties of the hot target material determine some refractory or quasi-refractory elements which cannot diffuse out of the target. For all the others, after the diffusion, the products are transported to an ion source to be ionized (process of effusion). However, even for non-refractory elements the diffusion time can be rather long, and the nuclei having very short half-lives do not have time to get out of the target-ion source before decaying. Despite the disadvantages of the ISOL-technique, the use of a thick target induces a high production rate and the resulting ion beams have excellent optical properties, which is very useful for mass spectrometry. Indeed, high quality beams can easily be transfered to mass spectrometers and ion traps. Many installations are using the ISOL-technique worldwide, such as ISAC at TRIUMF (Canada), ISOLDE at CERN (Switzerland), SPIRAL at GANIL (France) and others. They are referenced in [Lindroos 2004].

The in-flight production technique The method (also known as the discovery frontier) mainly uses fragmentation of intense heavy-ion beams in a thin target. Unlike the ISOL-method, the beam is not stopped in the target (only slowed down), and the momentum of the primary beam is transfered to the fragments produced by the nuclear reactions. With this technique all the elements can be produced, since there is no dependence on chemical properties, as well as very short-lived species. However, unlike the ISOL production technique, the production rate is lower, due to the use of a thin target, and the optical properties of the so-formed ion beam are not so well defined. Several in-flight facilities have been built around the world, such as GANIL in Caen (France), GSI in Darmstadt (Germany), MSU in Michigan (USA) and RIKEN in Tokyo (Japan).

3.4.1.2 Production of the neutron-rich rubidium and strontium

The exotic nuclei studied in this work were provided via the ISOL-method by the ISOLDE radioactive ion beam facility [Kugler 2000] at the European Organization for Nuclear Research (CERN). The high-intensity primary beam of proton (1.4 GeV) provided by the CERN's proton-synchrotron booster (PSB) is sent on a thick uranium carbide target which creates neutral fission products. These products are extracted from the hot target (ca. 2000 °C) by diffusion via a transfer line (heated to similar temperature as the target) connected to the ion source. The neutral atoms are then surface ionized on a heated tantalum cavity (ca. $1800-2000$ °C).

The surface ionization technique is one of the three ionization techniques which are available at ISOLDE, and it is very effective for alkali ions, such as rubidium, due to their low work function. The resonance-ionization laser ion source (RILIS) is another ionization technique, see [Marsh 2013] for a recent overview, in which the neutral atoms are ionized by the interaction with laser beams. The atoms of interest experience two or three atomic transitions. As they are element-specific, the RILIS method is highly selective. The third ionization method uses the plasma created by the forced electron beam induced arc discharge (FEBIAD) ion source installed at ISOLDE (with the recent VADIS variation [Penescu 2010]). This method is highly efficient for gas ionization or dedicated to other species with no efficient laser ionization schemes. It can produce high yields of ions of interest, but non-selectively.

To accelerate the ions, the ISOLDE ion source is floated to a high voltage. When extracted from the ion source, the singly-charged ions are thus accelerated to the corresponding kinetic energy. In this work the floating potential was 30 kV, so that the singly-charged ion kinetic energy was equal to 30 keV. After the beam production a mass separation is needed. At ISOLDE two on-line magnetic mass separators are available [Kugler 2000]: the general purpose separator (GPS) and the high resolution separator (HRS). The GPS, having a resolving power $R = m/\Delta m \sim 1000$, can be used to select one set of isobars, among the whole range of ions extracted from the ion source. The HRS can achieve a higher resolving power ($R =\sim 6000$), but it depends strongly on the beam properties. Via the HRS, the isobaric contamination can thus also be reduced to a certain extent. In the framework of the experiment discussed in this work, the ion beam was sent through the HRS magnets.

After the mass separation, the ion beam can be distributed to various experiments via the electrostatic beam-transport system of the ISOLDE hall. The ISOLTRAP mass spectrometer is located on the low-energy beam line.

3.4.2 The ISOLTRAP mass spectrometer

The ISOLTRAP mass spectrometer [Mukherjee 2008, Kreim 2013], shown in Figure 3.4, consists of four ion traps: a radio-frequency quadrupole (RFQ) cooler and buncher [Herfurth 2001], see section 3.4.2.1, a multi-reflection time-of-flight mass separator (MR-TOF MS), see section 3.4.2.2 [Wolf 2013] and two Penning traps, a cylindrical one for ion beam preparation and a hyperbolic one for precision mass spectrometry, see section 3.4.2.3 [Savard 1991].

The ion beam delivered to ISOLTRAP by ISOLDE is quasi-continuous. It consists of the ions of interest and the isobaric contaminants not cleaned by the HRS. Generally speaking, the yield of the

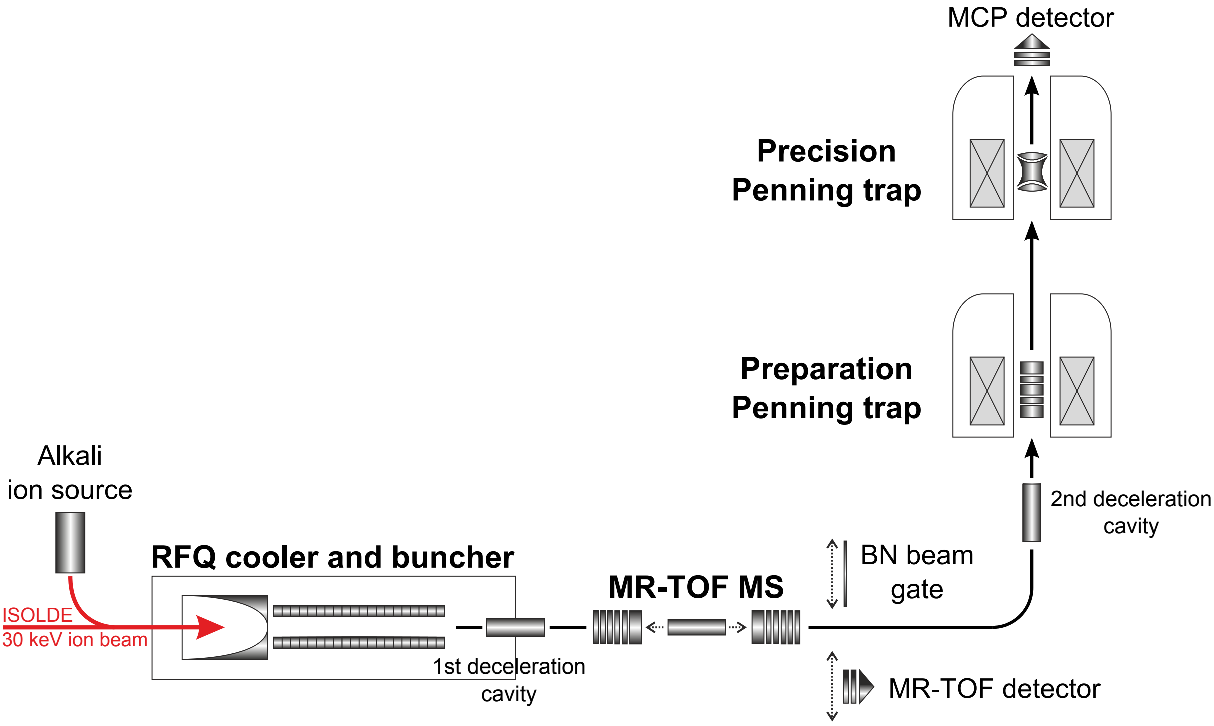

Figure 3.4 – Scheme of the ISOLTRAP mass spectrometer. For details, see text.

contaminants is much higher that the yield of the ions of interest. A mass measurement with the MR-TOF MS does not need highly pure beams. In fact, the close isobars are even used in the process of mass determination as calibrants. However, for precise mass measurements with the Penning trap, the beam needs to be purified from the contaminants. Furthermore, Penning traps require ion bunches with an axial energy as low as possible (near zero), and a reduced longitudinal and transverse emittance. These requirements are achieved by bunching and cooling the ion beam with the RFQ.

3.4.2.1 RFQ cooler and buncher

Prior to the mass measurements, the ISOLDE ion beam is prepared with the ISOLTRAP RFQ cooler and buncher, see Figure 3.4. The RFQ is installed on a HV platform. It is floated to a potential slightly lower than the kinetic energy of the singly-charged ions, so that, when the ions approach the RFQ they lose most of their kinetic energy, while still being able to enter the linear Paul trap. Once in the device, the ions are cooled and bunched (the RFQ principle is discussed in more detail in section 2.3.3.2). When the newly formed ion bunch is ejected from the RFQ, it has almost no kinetic energy and is attracted in the first deceleration cavity, see Figure 3.4 which is floated to a potential of ≈ 3 kV lower than the RFQ. In the cavity, the ions have thus a kinetic energy of ≈ 3 keV. The cavity is switched to ground potential while the ions are still inside, so that upon their exit from the cavity (and the HV area), their kinetic energy remains at ≈ 3 keV. This is a very convenient alternative to having the whole experimental setup installed on a HV platform.

3.4.2.2 MR-TOF MS and Bradbury-Nielsen gate

After the RFQ the ions enter the MR-TOF MS where, once trapped, they undergo multiple reflections. Their flight path is extended until a time-of-flight separation is reached between the ion species (due to their different mass-over-charge ratios) [Wolf 2012b]. The resolving power of the MR-TOF MS can reach values higher than $m/(\Delta m) \approx 10^5$ for a trapping time of about 25 ms (this time corresponds to an ion having a mass $A \approx 100$ u after roughly 1000 oscillations). See section 2.4 for a detailed discussion about the MR-TOF MS principle.

Once the ions have undergone enough revolutions to be mass separated, they are ejected from the MR-TOF MS towards the electron multiplier detector, see Figure 3.4. The ion time of flight is function of its mass, therefore, each ion species will reach the detector at different times. By knowing precisely the time of flight of an ion species, one can thus determine precisely its mass. The measurements of the rubidium masses were performed with the MR-TOF MS. A discussion about these measurements is made in section 3.5.

For the strontium masses determination, the MR-TOF MS was used as a beam purifier. After the time-of-flight separation in the MR-TOF MS, the ions can be ejected towards a Bradbury-Nielsen Gate (BNG). The electrostatic gate can be switched on/off very quickly so that only the species of interest can go through. The contaminants arriving before and after the ions of interest see a closed gate and are thus deflected from the beam axis. A pure ion bunch is then transported to the Penning traps for mass determination, see [Wolf 2012b] for a more detailed discussion about the BNG.

3.4.2.3 Penning traps

After the 90° bender and the second deceleration cavity the ions enter the last transport section of ISOLTRAP. It consists of two Penning traps (the preparation and the precision trap) and an MCP detector, see Figure 3.4. The trapping potentials of the preparation trap and the precision trap are ≈ 100 V and 10 V, respectively. Therefore the singly-charged-ion kinetic energies have to be of a few electron-volts (less than 10 eV) before the precision trap. To do so, the second deceleration cavity is first used, which decrease the kinetic energy of the ions to less than 100 eV, so that they can be trapped in the first trap, the preparation trap. In the latter the ions are cooled, decreasing their axial energy spread energy to less than 10 eV. The ions can then be transfered to the precision trap.

The preparation trap It is a cylindrical trap, see Figure 3.5, filled with helium buffer gas. The trap electrodes are placed in a strong magnetic field of 4.7 T. Before the installation of the MR-TOF MS, the preparation trap was the main device dedicated to ion beam purification via mass-selective resonant buffer-gas cooling [Savard 1991]. The technique, illustrated in Figure 3.6, goes as follows: The trapped ions have first their axial motion cooled by buffer-gas collisions. Then, via a dipole excitation, the magnetron radius of all ions is increased to a value larger than 0.75 mm (1.5 mm being the diameter of the ejection aperture of the preparation trap). The ions of interest are then centered by a mass selective quadrupole excitation at the cyclotron frequency ν_c of the ion of interest. The magnetron motion of the ions of interest is thus converted into cyclotron motion, which is a stable motion, meaning that it is damped by buffer-gas collisions. The resonantly-excited ions are thus centered in the trap, while the contaminants are still orbiting on a large magnetron radius. When all the ions are ejected from the trap, the ions of interest can go through the ejection aperture, whereas the contaminants hit the aperture and are suppressed.

The resolving power of the buffer gas cooling technique can be as high as $\approx 10^5$ in a few hundreds of milliseconds. The time consumed to achieve this resolving power is one order of magnitude more than the time needed for an equivalent resolution with the MR-TOF MS. Furthermore, for mass measurements on short-lived ion species, i.e. $T_{1/2} < 100$ ms, the preparation time must be as short as possible, in order to limit the decay losses of the ions of interest. The MR-TOF MS becomes thus the tool of choice as a bunch purifier, and the preparation trap is mainly used to cool the beam. To keep a reasonable preparation time of a few tens of milliseconds in the lower trap, the pressure of the buffer gas in the trap is increased by an order of magnitude ($\sim 1 \times 10^{-5}$ mbar).

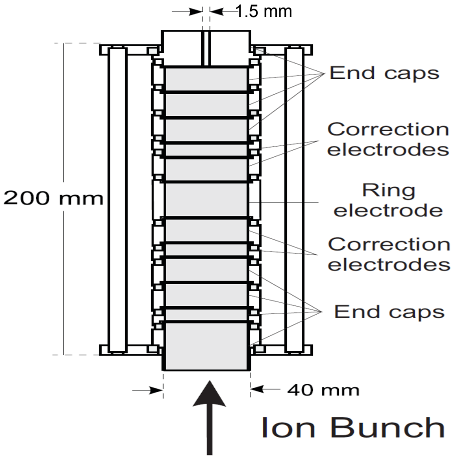

Figure 3.5 – Schematic view of the ISOLTRAP preparation trap.

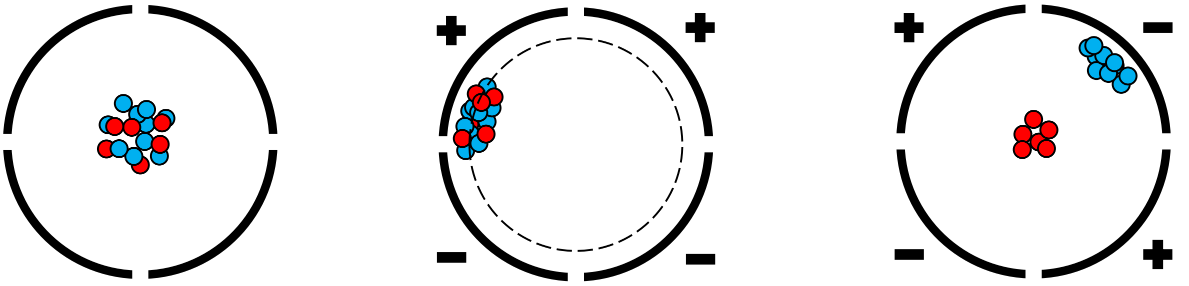

T = 0

Dipole excitation at ν_- (Mass independent)

Quadrupole excitation at ν_c (Mass dependent)

Figure 3.6 – Representation of the resonant buffer gas cooling technique in a Penning trap. Two ion species are trapped (labeled in red and blue). The ring electrode is four times radially segmented, and the trap is filled with buffer gas. The two ion species constituting the initial ion bunch are the contaminants, in blue, and the ions of interest, in red. Once the axial motion of the trapped ions is cooled by buffer-gas collisions, a short dipole excitation is applied to increase the magnetron motion of all ions in the trap. Then a mass selective quadrupole excitation is applied at the cyclotron frequency of the ions of interest. It converts their magnetron motion into cyclotron motion. The buffer gas damps the cyclotron motion and thus keeps the ions of interest in the center of the trap. The contaminants are still orbiting on a large magnetron radius, i.e. off center.

The precision trap After being ejected from the preparation trap, the ions are sent to the precision trap, shown in Figure 3.7, for high-precision mass measurement. It is a hyperbolic Penning trap placed in ultra-high vacuum and a strong homogeneous magnetic field of 5.9 T. The mass measurement consists on the determination of the cyclotron frequency ν_c via the TOF-ICR technique. A detailed discussion about the mass determination from the measured cyclotron frequency is presented in section 3.5.1.

3.4.2.4 Reference ion source

The ion transport section of ISOLTRAP starting from the 90° bender to the MCP detector is mass dependent (because of the two superconducting magnets). Prior to a measurement, this transport section needs to be optimized. This is usually performed with a stable ion beam which can be produced by an off-line ion source. Furthermore, reference ions are also needed for the mass determination process. The

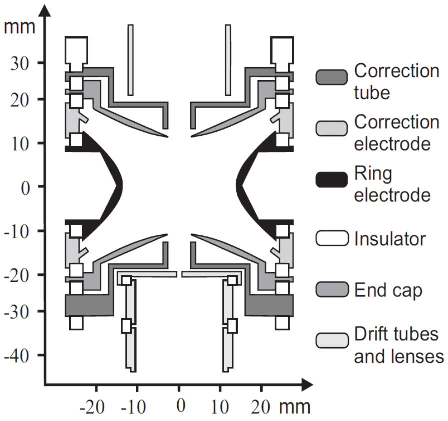

Figure 3.7 – Schematic representation of the ISOLTRAP precision trap.

ISOLTRAP setup includes two off-line ion sources used to create reference ions [Kreim 2013]. There is an alkali ion source, shown in Figure 3.4, which delivers sodium, potassium, cesium and rubidium ions from surface ionization (doped pellet heated to $\approx 1000°$). The second one is a laser-ablation ion source, delivering carbon-cluster ions (from C_2 to $C_{>20}$). The laser-ablation ion source was not involved in the mass measurements discussed in this work and it is not represented in Figure 3.4. This ion source is located between the MR-TOF MS and the 90° bender.

The alkali ion source The alkali ion source produces stable low ion currents (50 pA – 1 nA). However this ion source does not produce a large mass range of nuclei. A transport optimization with a reference ion too far in mass from the ion of interest can have a strong impact on the ISOLTRAP transmission efficiency. Indeed, the transport efficiency between the MR-TOF MS and the Penning trap can vary from 100% (when the optimization is performed with a reference ion close in mass to the ion of interest) to below 10% (when the mass difference is too important).

The laser-ablation ion source The laser ion source can produce carbon clusters over the full mass range of the studied radioactive nuclei. However, it presents count rate fluctuations linked to the laser power and the target conditions. This source was mainly used for a systematic study of the precision of ISOLTRAP. The systematic studies and the subsequent determination of the mass-dependent and residual uncertainties of ISOLTRAP were performed using carbon clusters covering the full mass range of interest, produced using this ion source [Kellerbauer 2003]. Since the maintenance operations of the ISOLTRAP magnets in 2013, the systematic errors of the ISOLTRAP setup might have changed, which calls for the repetition of these studies.

3.5 Mass measurement principle

3.5.1 Penning-trap mass measurement

As discussed in section 2.2.4, a mass measurement with a Penning trap consists of determining the cyclotron frequency of the ion of interest. To do so, the quadrupole excitation frequency is varied in steps around the assumed cyclotron frequency. After each quadrupole excitation, the ion bunch is released and its time of flight from the trap to the MCP detector is measured, see equation (2.14). Once the scan is over, a so-called TOF-ICR resonance is obtained. An example of TOF-ICR resonance of the singly-charged ^{102}Sr is shown in Figure 3.8.

3.5.1.1 Determination of the cyclotron frequency

The quadrupole excitation of the ions of interest is applied at a constant amplitude for a fixed interval T_{rf}. The Fourier transformation of this rectangular excitation amplitude gives the theoretically expected shape of the TOF resonance. The obtained function is similar to the square of the $\mathrm{sinc}(x) = \sin(ax)/ax$ function [Bollen 2004], but reversed due to the conversion into a time-of-flight resonance. The resonance shape presents a large minimum in the middle (corresponding to the cyclotron frequency) and small side bands. The width of the signal and the resolving power are Fourier limited by the duration of the quadrupole excitation. The resolving power is linked to the excitation time by the relation:

$$R = \frac{m}{\Delta m} = \frac{\nu_c}{\Delta \nu_c} \approx \nu_c T_{rf} \tag{3.20}$$

The TOF-ICR type excitation is the traditional way to apply a quadrupole excitation with a rectangular function. The Ramsey type excitation represents another time pattern for the quadrupole excitation [George 2007a, George 2007b]. It consists of two short rectangular pulses separated by a waiting time. The new resonances obtained from the Fourier transformation of the excitation amplitude in the Ramsey scheme are symmetric and have narrower fringes (Figure 3.10b and Figure 3.10c are examples of a Ramsey resonance for the singly-charged ^{101}Sr and ^{102}Sr, respectively). As all the fringes are as deep as the central one, it becomes ambiguous to determine which time-of-flight minimum corresponds to the cyclotron frequency. Therefore, prior to the use of the Ramsey technique, the cyclotron frequency needs to be determined by the regular TOF-ICR method. The Ramsey type excitation allows to reduce the statistical error in the frequency determination by a factor of three, while keeping the number of ions and the excitation time constant [George 2007b].

A data analysis software is used to fit the TOF resonances obtained via the regular TOF-ICR method or via the Ramsey type excitation. The software called EVA was developed by Stefen Schwarz for ISOLTRAP and it is now maintained by Ryan Ringle. For both types of resonances, parameters are used to fit the theoretical line shape to the experimental data. Some of these parameters are fixed:

- the damping due to the rest gas collision (expressed in s^{-1})
- the excitation time (equal to a few hundreds of ms maximum for radioactive nuclei and equal to 1.2 s for the reference ion)

Others are free:

- the cyclotron resonance frequency (about 0.9 MHz for radioactive nuclei and 1 MHz for the reference ion)
- the initial magnetron radius before the quadrupole excitation (ideally about 0.7 mm)
- the number of conversions between the radial modes (ideally equal to 1)
- the time-of-flight offset (corresponding to the initial axial energy of the ions)

3.5.1.2 From the cyclotron frequency to the mass

In section 2.2.1 was introduced the equation: $\nu_c = qB/2\pi m$ which relates the cyclotron frequency of an ion to its charge-over-mass ratio and the magnetic field at the center of the Penning trap. To perform a precise mass measurement, one has to know precisely the magnetic field strength. However, it was mentioned in section 2.2.2 that the magnetic field suffers from imperfections e.g. due to the flux

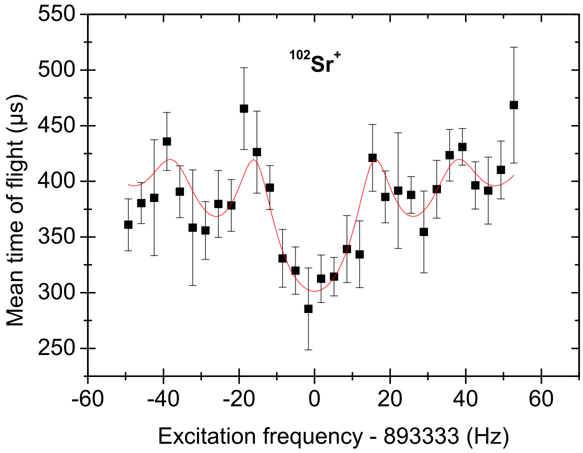

Figure 3.8 – Time-of-flight ion cyclotron resonance of ^{102}Sr ions with the fit curve for determining the cyclotron frequency.

creep phenomenon, which induces a linear drift of the field. Furthermore, the helium pressure and temperature fluctuations induce a non-linear drift of the magnetic field. Its magnitude has been quantified by [Kellerbauer 2003], see section 3.5.1.3. In order to determine precisely the magnetic field, before and after each ion of interest mass measurement, one uses the cyclotron frequency formula in reverse, i.e. one measures the cyclotron frequency of a reference ion (singly-charged and delivered by the ISOLTRAP alkali ion source) having a precisely known mass, and interpolates the resulting strength of the magnetic field to the measurement time. For all the mass measurements presented in the following, the reference mass is $^{85}\mathrm{Rb}^{+}$. The determination of the magnetic field via the reference singly-charged ion is thus given by:

$$\nu_{c,ref} = \frac{qB}{2\pi(m_{ref} - m_e)} \Rightarrow B = 2\pi\nu_{c,ref}\frac{(m_{ref} - m_e)}{q}, \tag{3.21}$$

with m_e the electron mass, $\nu_{c,ref}$ the interpolated cyclotron frequency of the reference ion and m_{ref} the mass of the reference ion. The electron binding energy is neglected, it is for singly-charged ions much smaller than the achievable precision of the measurement technique. The cyclotron frequency of the unknown singly-charged ion can be written as:

$$\nu_{c,x} = \frac{qB}{2\pi(m_x - m_e)} = \nu_{c,ref}\frac{m_{ref} - m_e}{m_x - m_e} \tag{3.22}$$

where $\nu_{c,x}$ and m_x are the cyclotron frequency and the mass of the unknown ion, respectively. From the introduction of the ratio $r_{ref,x}$:

$$r_{ref,x} = \frac{\nu_{c,ref}}{\nu_{c,x}}, \tag{3.23}$$

one can write the expression of the unknown ion mass:

$$m_x = r_{ref,x}(m_{ref} - m_e) + m_e. \tag{3.24}$$

From equation (3.23), it is shown that what one calls a Penning-trap mass measurement consists of the determination of the cyclotron frequency ratio between the ion of interest and the reference ion.

3.5.1.3 The measurement uncertainties

The total uncertainty of a mass determination takes into account the statistical and the systematic errors. The different contributions are discussed in the following.

Statistical uncertainty The mass of the ion of interest can be calculated via equation (3.24). The statistical uncertainty of this equation is linked to the error in determining the cyclotron frequencies (of the ion of interest and of the reference ion, constituting the ratio $r_{ref,x}$), and to the uncertainty of the reference mass. The statistical uncertainty of a cyclotron frequency measurement has three contributions: the amount of data acquired, the quality of the experimental resonance data and the excitation time [Bollen 2001].

The amount of data acquired: For each quadrupole excitation pulse a number of events are acquired. As an experiment is time-limited, the number of detected events should be optimized, but keeping the limited production rate in mind. The second limiting factor is the ISOLTRAP transport efficiency, which is usually around 1%, see section 3.4.2.4. For short lived species, one to ten events are detected per proton pulse on the ISOLDE target.

The quality of the experimental resonance data: Different factors can reduce the quality of the experimental resonance data, e.g. the rest gas in the trap can be ionized via decay radiation creating in-trap charges. Furthermore, the experimental parameters can vary, such as the dc and ac signals applied on the electrodes, or the digital signals from the electronic devices. The variation of these parameters can induce scattering around the best-fit theoretical line-shape. This effect is enhanced when a strong amount of contaminants is present in the ion bunch. Indeed, the contaminants have a different frequency response to the quadrupole excitation signal. From all of these effects results a perturbation of the average time of flight of the ion of interest. This also leads to systematic effects discussed in the following.

The excitation time: The excitation time scales inversely proportional with the width. As an example, from an excitation time of ∼ 1 s results a full width at half maximum (FWHM) of the resonance curve of ∼ 1 Hz. Therefore, the longer the excitation time is, the narrower the resonance peak is, and the better the peak center is constrained. The cyclotron frequency is thus more precisely determined. However, when the species of interest have short half-lives (below 1 s) the excitation time has to be shorter to minimize the decay losses.

The three effects listed above were translated into the empirical law for the statistical uncertainty $\delta\nu_c$ of a cyclotron-frequency measurement [Bollen 2001]:

$$\left(\frac{\delta\nu_c}{\nu_c}\right)_{stat} = \frac{1}{\nu_c}\frac{C}{\sqrt{N}T_{\mathrm{rf}}}, \tag{3.25}$$

where $C \approx 0.9$ is a parameter which slightly depends on the quality of the experimental data, see [Kellerbauer 2003], and N is the number of events.

The reference ions used at ISOLTRAP are non-radioactive nuclei, abundantly produced and can be easily purified with the MR-TOF MS. The reference TOF spectra are thus high-statistics, pure data sets taken at long excitation times (usually 1.2 s). The reference cyclotron-frequency measurement gives then only a small contribution to the uncertainty of the measured frequency ratio. Furthermore, the mass of the reference ion is typically known with a much higher precision compared to the mass of the ion of interest. The statistical uncertainty of the final mass value is thus dominated by the statistical uncertainty on the cyclotron frequency measurement of the ion of interest.

Systematic errors The systematic errors of TOF-ICR measurements have been extensively studied for ISOLTRAP. They usually end up being lower than the statistical uncertainty for exotic nuclei. Three sources of systematic uncertainty can be distinguished: the drift of the magnetic field, the number of ions constituting the trapped ion bunch, and the imperfections of the trap electrostatic field.

Drift of the magnetic field: As already discussed in section 2.2.2 the magnetic field drifts over time. One component of the drift is linear (due to the flux creep phenomenon), the other one is non-linear (due to temperature and pressure fluctuations of the helium inside the cryostat). The correction of the linear drift is performed via a linear interpolation of the magnetic field between the two reference measurements surrounding the measurement of interest, see section 3.5.1.2. The resulting value is the one used to compute the frequency ratio (equation (3.23)). The non-linear drift fluctuation has been quantified and its magnitude was evaluated in [Kellerbauer 2003]:

$$\left(\frac{\delta\nu_c}{\nu_c}\right)_B = 6.35\mathrm{x}10^{-11}\ /\mathrm{min}\times\Delta\mathrm{T}. \tag{3.26}$$

Number of ions: The Coulomb interaction between the trapped ions perturbs their motion with respect to the single-particle case, see section 2.2.2. One way to minimize the Coulomb interactions is to constrain the number of ions present in the Penning trap at the same time. An average of $3-4$ events detected after ejection is a good limit. Another way to reduce the Coulomb effect is the Z-class analysis. It consists of a study of the resonance-frequency variation as a function of the number of detected events. The data set is divided in equal subsets corresponding to different averaged numbers of events. For each subset, the obtained resonance frequency is fitted. An extrapolation to zero detection events is then performed, which is chosen as the final value of the cyclotron frequency. The Z-class analysis technique is powerful, however, it is only possible if the amount of collected data allows it.

Imperfections of the electrostatic field: The deviation of the electrostatic field from the a quadrupole field and the misalignment of the trap electrodes (with respect to the axis of the magnetic field), see section 2.2.2, lead to the so-called "mass-dependent shift". It is linked to the mass difference between the reference ion and the ion of interest. Because of this effect a deviation of the cyclotron-frequency ratio from its real value is induced. A systematic study using carbon cluster ions of different masses, produced by the ISOLTRAP laser-ablation ion source (section 3.4.2.4), has been performed in order to determine this shift [Kellerbauer 2003]. It was determined to be:

$$\left(\frac{\delta r_{ref,x}}{r_{ref,x}}\right)_m = 1.6\times 10^{-10}(\mathrm{m}-\mathrm{m}_{\mathrm{ref}})\ /\mathrm{u} \tag{3.27}$$

Residual systematic uncertainty: This uncertainty is not due to a specific cause, but is determined as the limit of the systematic accuracy [Kellerbauer 2003]. It was determined from the observation that after the corrections of the systematic errors resulting from the magnetic field fluctuations and electrostatic field imperfections, the scattering of the frequency ratios around the expected values leads to a reduced χ^2 still greater than one. This was interpreted as the residual systematic uncertainty of the ISOLTRAP mass spectrometer and it was estimated to:

$$\left(\frac{\delta r_{ref,x}}{r_{ref,x}}\right)_{res} = 8\times 10^{-9}\ . \tag{3.28}$$

The total uncertainty By definition, a frequency-ratio measurement implies two cyclotron-frequency measurements. The first one is used as a reference in order to determine precisely the magnetic field strength (result of an interpolation between two reference measurements before and after the measurement of the ion of interest), the other one is the measurement of the cyclotron frequency of the ion of interest. As mentioned before, the latter carries most of the statistical uncertainty. Furthermore, for every frequency ratio $r_{ref,x}$, the systematic uncertainty due to the magnetic field fluctuations is calculated, since it depends on the total measurement time for the specific data file. The uncertainty of each frequency-ratio $\delta r^i_{ref,x}$ is thus:

$$\delta r^i_{ref,x} = \sqrt{\left(\delta r^i_{ref,x}\right)^2_{stat} + \left(\delta r^i_{ref,x}\right)^2_B}. \tag{3.29}$$

The mean frequency ratio is calculated as:

$$\bar{r}_{ref,x} = \frac{\sum_i \left[r^i_{ref,x} / \left(\delta r^i_{ref,x}\right)^2\right]}{\sum_i \left[1 / \left(\delta r^i_{ref,x}\right)^2\right]}, \tag{3.30}$$

and its uncertainty is expressed as follows:

$$\delta \bar{r}_{ref,x} = \sqrt{\frac{1}{\sum_i \left[1 / \left(\delta r^i_{ref,x}\right)^2\right]}}. \tag{3.31}$$

The mean frequency ratio $\bar{r}_{ref,x}$ is then corrected by the mass-dependent systematic error and by the residual systematic error. The total uncertainty is calculated as [Kellerbauer 2003]:

$$(\delta \bar{r}_{ref,x})_{total} = \sqrt{(\delta \bar{r}_{ref,x})^2 + (\delta r_{ref,x})^2_m + (\delta r_{ref,x})^2_{res}} \tag{3.32}$$

3.5.2 MR-TOF MS mass measurement

A mass measurement with the MR-TOF MS consists of determining the total time an ion has spent flying in the MR-TOF MS device up to the TOF detector. This time can be expressed as a function of the ion mass-over-charge ratio by the simple relation:

$$t = a\sqrt{\frac{m}{q}} + b \tag{3.33}$$

where a and b are device-specific parameters. a is a device dependent parameter which increases with the number of revolutions the ions undergo inside the device. It is thus proportional to the trapping time. b is an independent parameter [Wolf 2013]. While a Penning-trap mass measurement requires a pure ion bunch, this is not the case for a measurement with the MR-TOF MS. Indeed, the multiple oscillations the ions undergo inside the device allow a time-of-flight separation as a function of their respective mass-over-charge ratios, see equation (3.33). The time-of-flight difference between two ion species grows linearly [Wolf 2013] with the number of revolutions. Furthermore, the isobaric contaminants of known masses can even be used to determine the mass of the ion of interest, see section 3.5.2.1. Once the separation between the species is reached, the ions are ejected and are detected on the TOF detector.

To compute the mass of the ion of interest, one needs to determine the a and the b parameters from equation (3.33). This process involves the time-of-flight measurement of two reference ions.

3.5.2.1 Reference ions

Two types of reference ions can be distinguished, either "internal" or "external". The internal reference ion is an isobaric contaminant delivered in the beam. It is recorded in the same time-of-flight spectrum as the ion of interest. The external reference is provided by an off-line ion source.

Two internal references: The ideal situation for an MR-TOF MS measurement is to have two distinct internal reference ions of well-known masses. In this situation, all the species have encountered the same fluctuations in time of flight, which might have been induced by the device itself (like drifts of the mirrors potentials). In Figure 3.9a is shown an example of the impact of voltage drifts on the data. To illustrate this, the events are not binned into a single time-of-flight histogram, but grouped in several histograms which are represented as a function of the ion's time of flight (horizontal axis) and the experimental time (vertical axis) in a 2D plot. The mean TOF of the different histograms is shifting with time. Assuming that the TOF drifts have the same direction and the same magnitude, it is possible to use one of the internal reference peaks to correct the TOF of all ions in the spectrum. The first histogram of the reference peak (corresponding in the figure to measurement time 0) is fitted and its mean TOF is taken as a reference value for correction. For every subsequent histogram (corresponding to higher measurement time) the whole spectrum is shifted so that the average TOF of the reference histogram is equal to the reference mean value. The result is a spectrum with less significant TOF fluctuations. One notes that the method does not work in case of very strong drifts. In Figure 3.9a one can see that the measurements number 3 and 4 suffer from a very strong drift, and they are not fully corrected in Figure 3.9b.

One internal reference: If only one internal reference is available, there are two possibilities. Two TOF spectra (which include the ion of interest and the reference) can be obtained with two different time-of-flight values, i.e. two different numbers of revolutions inside the MR-TOF MS. The other possibility is to have the second reference as an external reference delivered by an off-line ion source. The first method is possible because the parameter b can be eliminated from equation (3.33) by subtracting the time-of-flight values obtained at two different revolution numbers [Wolf 2013]. Therefore, only the time-of-flight differences and the mass of the reference ion are needed to compute the mass of the ion of interest. The second method requires that the external reference is treated in the same way as the ion of interest. The preparation in the RFQ should be the same, as well as the number of revolutions in the MR-TOF MS. In order to minimize the systematic uncertainty, the reference measurement has to be performed before and after the ion of interest measurement with a delay time as short as possible. The internal reference is used to correct the TOF drifts via the method mentioned in the previous paragraph.

Two external references: When no internal reference ion is available, only external references, having a mass as close as possible to the ion of interest, can be used. To minimize the systematic drifts as much as possible the TOF measurements of the reference and of the ion of interest have to be as short as possible. However, the TOF drift corrections (discussed at the beginning of the section) cannot be applied, as the measurements of the ion of interest and of the reference ions are not performed simultaneously. The chapter 4 is dedicated to an ion source which was developed in order to provide a broad mass renge of external reference ions to a MR-TOF MS.

The three different mass determination possibilities, discussed above, have been tested over a wide mass range. They all allow to reduce the systematic uncertainties. However, it was proven that the achievable relative uncertainty can be on the order of the ppm to the sub-ppm region when at least one internal reference is available [Wolf 2013].

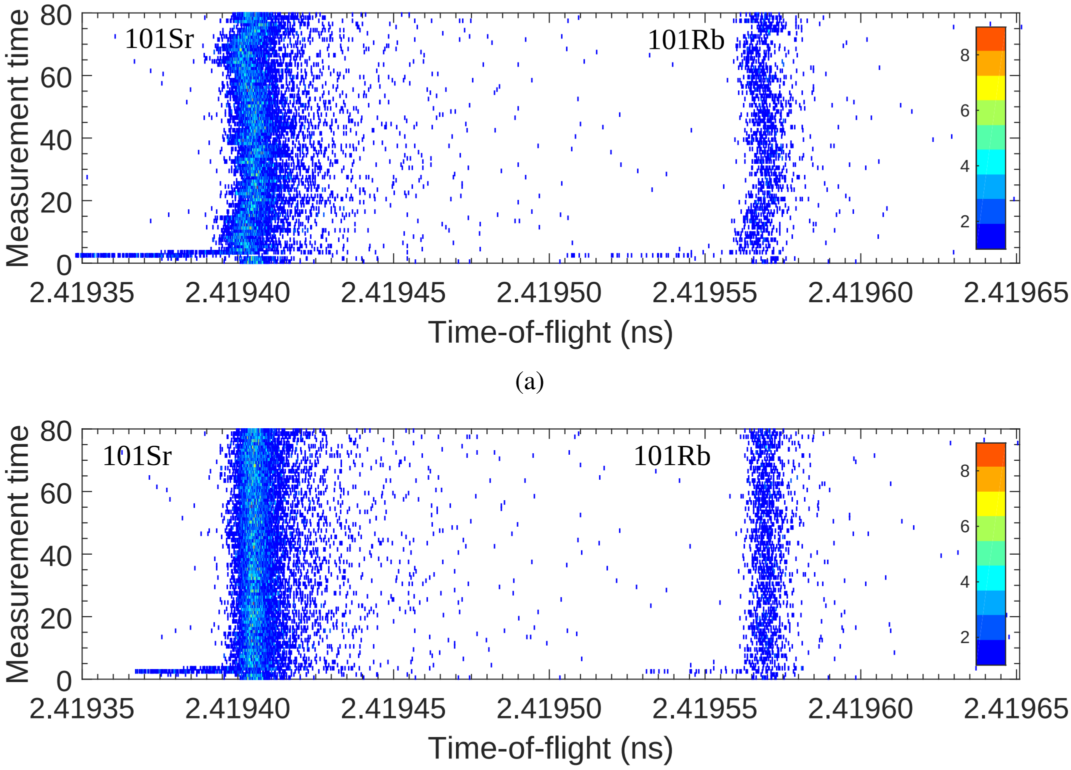

(a)

(b)

Figure 3.9 – 2D color-coded intensity plot of a time-of-flight spectrum of singly-charged ^{101}Sr and ^{101}Rb. The number of ion counts is represented as a function of the time of flight (horizontal axis) and as a function of the measurement time (vertical axis). (a) corresponds to the uncorrected time-of-flight data. The corrected spectrum with respect to $^{101}\mathrm{Sr}^{+}$ is shown in (b).

3.5.2.2 Mass evaluation with the MR-TOF MS

For the mass determination of the neutron-rich rubidium isotopes, one internal reference was available, the strontium isobars delivered from ISOLDE. It was thus used to correct the TOF drifts, see Figure 3.9. Furthermore, the strontium masses are well known since they were previously determined with the precision trap, see section 3.6. The external reference was $^{85}\mathrm{Rb}^{+}$ provided by the ISOLTRAP alkali ion source.

The relation used to compute the mass of the ion of interest is:

$$\begin{aligned}\sqrt{m} &= C_{tof} \times (\sqrt{m_{ref,1}} - \sqrt{m_{ref,2}}) \\ &\quad + \frac{1}{2} \times (\sqrt{m_{ref,1}} + \sqrt{m_{ref,2}}),\end{aligned} \tag{3.34}$$

with $m_{ref,i}$ and $t_{ref,i}$ the mass and the time of flight of the reference ions, respectively. The parameter C_{tof} is calculated from equation (3.33) [Wienholtz 2013]:

$$C_{tof} = \frac{t}{t_{ref,1} - t_{ref,2}} - \frac{t_{ref,1} + t_{ref,2}}{2(t_{ref,1} - t_{ref,2})}. \tag{3.35}$$

equation (3.34) relates the mass of the ion of interest to the mass of the two reference ions, furthermore, this equation also allows a re-evaluation of the data in case the internal reference mass is evaluated to a different value by another experiment.

3.5.2.3 Contribution of the uncertainties

The mass of the ion of interest is calculated with equation (3.34). The uncertainties in the mass calculation come from the mass uncertainty of the reference ions and from the C_{tof} uncertainty. The uncertainties of the reference ion masses result either from the AME 2012 [Wang 2012] (for ^{85}Rb and ^{100}Sr), or from the Penning-trap mass measurements (for ^{101,102}Sr)[1]. The statistical and systematic uncertainties of the C_{tof} values are presented in the following.

The statistical uncertainty This uncertainty is linked to the error in determining the time of flight of the ion of interest and of the two reference ions (equation (3.35)). The respective time-of-flight peaks are fitted with Gauss functions, via a dedicated software developed by F. Wienholtz. The error of each Gauss fit is then propagated in the C_{tof} formula and yields a statistical uncertainty $\delta c_{tof,stat}$.

The systematic uncertainty Within the framework of this experiment, despite the strontium, well-known isotopes could not be clearly identified in the spectra containing the ion of interest. It was thus chosen to determine the systematic uncertainty via the measurements of several well known isotopes performed before and after the mass measurements of interest.

For these studies, the stable ^{56}Mn, ^{58,61}Ni and ^{63}Cu isotopes were used, as well as ^{56,58}Cr. In the AME 2012 [Wang 2012] ^{56,58}Cr are not well known. However, the mass of these two isotopes were later measured with a precision Penning trap, they were thus considered as well known for the systematic error determination process. The ^{56,58}Cr masses will be published in an article by M. Mougeot. For each of these isotopes, equation (3.34) was used in reverse and a $C_{tof,\,AME}$ was calculated. Via a comparison between the $C_{tof,\,AME}$ and the C_{tof} (equation (3.35)), one can compute an average relative deviation of the C_{tof} from the expected value. The relative error obtained is: $C_{tof,\,rel} = 2.13 \times 10^{-6}$. This relative error is then multiplied by the C_{tof} value of the rubidium isotopes of interest, which gives a systematic error for each isotope of $\delta c_{tof,sys} = 1.07 \times 10^{-6}$. The total error on the C_{tof} is thus:

$$\delta c_{tof} = \sqrt{(\delta c_{tof,stat})^2 + (\delta c_{tof,sys})^2}. \tag{3.36}$$

3.5.3 The atomic mass evaluation

The masses studied in this work are not determined directly but relatively to the respective references. The cyclotron frequency ratios (for Penning-trap measurements) and the C_{tof} values (for MR-TOF MS measurements) act as links (constraints) between the masses of different nuclei. There exists only one absolute mass which is the mass of the isotope Carbon-12. This is the mass which was chosen to define the atomic mass unit: $1\ \mathrm{u} = M(^{12}\mathrm{C})/12$. The ^{12}C atomic mass is then 12 and its mass excess is zero. The links presented in this work are added to the links provided by other mass spectrometry techniques, which also require reference nuclei (Schottky, rigidity etc.), or from decay and reaction energies [Wang 2012]. All the masses and the links together can be pictured as a surface 2D plane (N, Z) with one fixed point, the ^{12}C mass. In this picture, the links are described by linear equations with the atomic masses as variables. As the mass measurement methods are various, many masses were measured multiple times generating many corresponding links. All the links are taken into account via a least-square method weighted by the precision of the different measurements. Thanks to this method, the adjusted masses can be determined. Regularly, the whole mass surface is adjusted with the new measurements, and all masses can be influenced by the new links depending on their weight. The masses determined with

---

[1] The mass measurement of the ^{100}Sr presented in this work has a larger uncertainty compared the one presented in the AME 2012, see Table 3.2. Therefore, the ^{100}Sr mass and uncertainty values benchmarked in the AME 2012 were used to calculate the error on the ^{100}Rb mass.

very high precision (like Penning-trap mass measurements) usually carry the largest weight of all links attached to a certain nuclide and thus put the strongest constraint on its mass. All these results, including further details and information, are summarized in the atomic mass evaluation [Wang 2012].

3.6 Experimental results

The mass measurements of the strontium and rubidium isotopes were originally not foreseen, the beam time was supposed to be dedicated to the mass determination of the $^{52-55}$Sc isotopes. The ISOLTRAP transport efficiency was optimized with a stable ^{52}Cr ion beam from ISOLDE and the excitation schemes were tuned for nuclei with half-lives of a few seconds. However, the neutron-rich scandium isotopes could not be delivered by ISOLDE for reasons which are still not fully understood, possibly related to in-target chemistry or a very slow release. The physics case thus changed in favor of the neutron-rich rubidium and strontium isotopes.

As mentioned in section 3.4.2.4, the transport optimization is mass dependent because of the magnetic fields generated by the two superconducting magnets. When the physic case of the experiment was changed in favor of $^{100-102}$Sr and $^{100-102}$Rb, the transport optimization with the stable ^{52}Cr ion beam was not valid anymore. An ion beam of singly-charged ^{95}Rb delivered by ISOLDE was used to quickly re-optimize the ISOLTRAP ion transport.

The excitation scheme in the preparation Penning traps also had to be changed because it was too long for the half-lives of the new ions of interest. A shorter preparation trap cycle was implemented, 70 ms instead of $100-150$ ms. However, a shorter preparation cycle implies less cooled ion bunches. Additional losses were therefore noted during the transport between the preparation trap and the precision trap. Because of this reason, the ^{100}Rb mass measurement, which had already been performed with the precision trap [Manea 2013], could not be repeated. Obviously, due to the lower count rates, associated to their shorter half-lives, the ^{101,102}Rb masses could not be measured with the precision trap either.

The masses of $^{100-102}$Sr were measured with the precision trap and the masses of $^{100-102}$Rb with the MR-TOF MS. In the MR-TOF MS spectra, both rubidium and its strontium isobar were present. As mentioned before, the strontium masses were determined by the Penning-trap measurements, it was thus possible to use them as on-line references for the determination of the rubidium masses.

The experimental results are summarized in Table 3.1 (Penning-trap measurements) and Table 3.2 (MR-TOF MS measurements), which also present the existing literature values, if applicable. A more detailed discussion of each measurement is also presented separately in the following.

3.6.1 ^{100}Sr and ^{100}Rb

The ^{100}Sr mass was determined via a TOF-ICR resonance of 200 ms excitation time, see Figure 3.10a. The resulting mass excess is $-59820(27)$ keV, as shown in Table 3.1. The result is in agreement with two other Penning-trap mass measurements performed at JYFLTRAP [Hager 2006] (the corresponding mass excess is: $59828(10\,\mathrm{keV}/c^2)$ and more recently at TITAN [Klawitter 2016].

The ^{100}Rb mass was already measured once at ISOLTRAP in 2012 [Manea 2013] using the Penning trap. In this experiment, however, the Penning trap part of the setup was optimized for ions of other mass and half-life range and hence could not be used to measure the very-short lived rubidium species.

^{100}Rb^{+} was thus measured with the MR-TOF MS. The ^{100}Sr^{+} ions were used as on-line reference, while for off-line reference ^{85}Rb^{+} ions were used. Six time-of-flight spectra were taken. For five of them, the ions have undergone 500 revolutions in the MR-TOF MS, for the last spectra, the number of revolutions was 1000. The latter is shown in Figure 3.11a. The evaluated ^{100}Rb mass excess is $-46288(22)$ keV. It agrees within two standard deviations with the previous ISOLTRAP measurement [Manea 2013], and with the recent Penning-trap measurement from TITAN [Klawitter 2016].

3.6.2 ^{101}Sr and ^{101}Rb

Two regular TOF-ICR, of 100 ms excitation time, and two Ramsey-type measurements, of 10 ms excitation time and 80 ms waiting time, were taken with the precision trap for ^{101}Sr^{+}. An example of a Ramsey resonance is shown in Figure 3.10b. The corresponding mass excess of $-55315(20)$ keV agrees with the mass measurement performed recently at TITAN [Klawitter 2016]. It also confirms the 3σ deviation from AME2012 observed at TITAN.

Here is reported the first mass measurement of ^{101}Rb. Two time-of-flight spectra were taken with the MR-TOF MS, both with a number of revolutions of 1000. A time-of-flight spectrum is shown in Figure 3.11b. The resulting mass excess is $-42554(30)$ keV. The value adopted in the AME2012 is extrapolated using β-endpoint measurements [Balog 1992]. The ^{85}Rb^{+} and the ^{101}Sr^{+} ions were used for off-line and on-line references, respectively.

3.6.3 ^{102}Sr and ^{102}Rb

The first direct mass measurement of ^{102}Sr and the first mass measurement of ^{102}Rb are presented here. The ^{102}Sr mass was determined via a regular TOF-ICR measurement of 80 ms excitation time, and a Ramsey-type measurement of 10 ms excitation time and 40 ms waiting time. The Ramsey resonance is shown in Figure 3.10c. The corresponding mass excess is $-52159(66)$ keV. The AME2012 value of ^{102}Sr is a result of a β-endpoint measurement for ^{102}Sr (β^{-}) ^{102}Y.

Concerning ^{102}Rb six time-of-flight spectra were taken, two with a number of revolutions of 500, and four with a number of revolutions of 1000. A time-of-flight spectrum obtained after 1000 revolutions is shown in Figure 3.11c. The resulting mass excess is $-37286(71)$ keV. The AME2012 value of ^{102}Rb is extrapolated using β-endpoint measurements from [Balog 1992].

Due to the low statistics of ^{102}Rb in the spectrum, the Gauss fit with the χ^2 method do not reproduce the data and overestimate the peak width. An additional evaluation of the data was thus performed with the maximum likelihood method (which is more adapted to low statistics data). The time-of-flight value obtained with the maximum likelihood method, shown in Figure 3.11c, agrees within one standard deviation with the time-of-flight value obtained via the Gauss fit with the χ^2 method. The result from the χ^2 method was thus kept as a reference for the ^{102}Rb mass determination.

Isotope	Half-life (ms)	$r = \nu_{c,ref}/\nu_c$	ME_{ISOLTRAP} (keV/c^2)	ME_{AME2012} (keV/c^2)	$\Delta_{\text{ISOLTRAP-AME2012}}$ (keV/c^2)	ME_{TITAN} (keV/c^2)
^{100}Sr	202(3)	1.176937584(344)	-59821(27)	-59830(10)	10(29)	-59816(11)
^{101}Sr	113.8(1.7)	1.188771552(259)	-55315(21)	-55560(80)	245(83)	-55327.6(9.8)
^{102}Sr	69(6)	1.200588455(847)	-52160(67)	-52360(70)	201(96)	

Table 3.1 – Frequency ratios of ^{100,101,102}Sr^{+}, relative to ^{85}Rb^{+}, measured with the precision Penning trap. The corresponding mass excess (ME_{ISOLTRAP}) values are shown. The half-lives, from NUBASE2012 [Audi 2012], and mass excess values (ME_{AME2012}), from AME2012 [Wang 2012], are also given. The results of a recent publication (2016) from the TITAN experiment, not in the AME2012, are also shown [Klawitter 2016]. The difference between the ISOLTRAP and the AME2012 values for each isotope are shown in the $\Delta_{\text{ISOLTRAP-AME2012}}$ column.

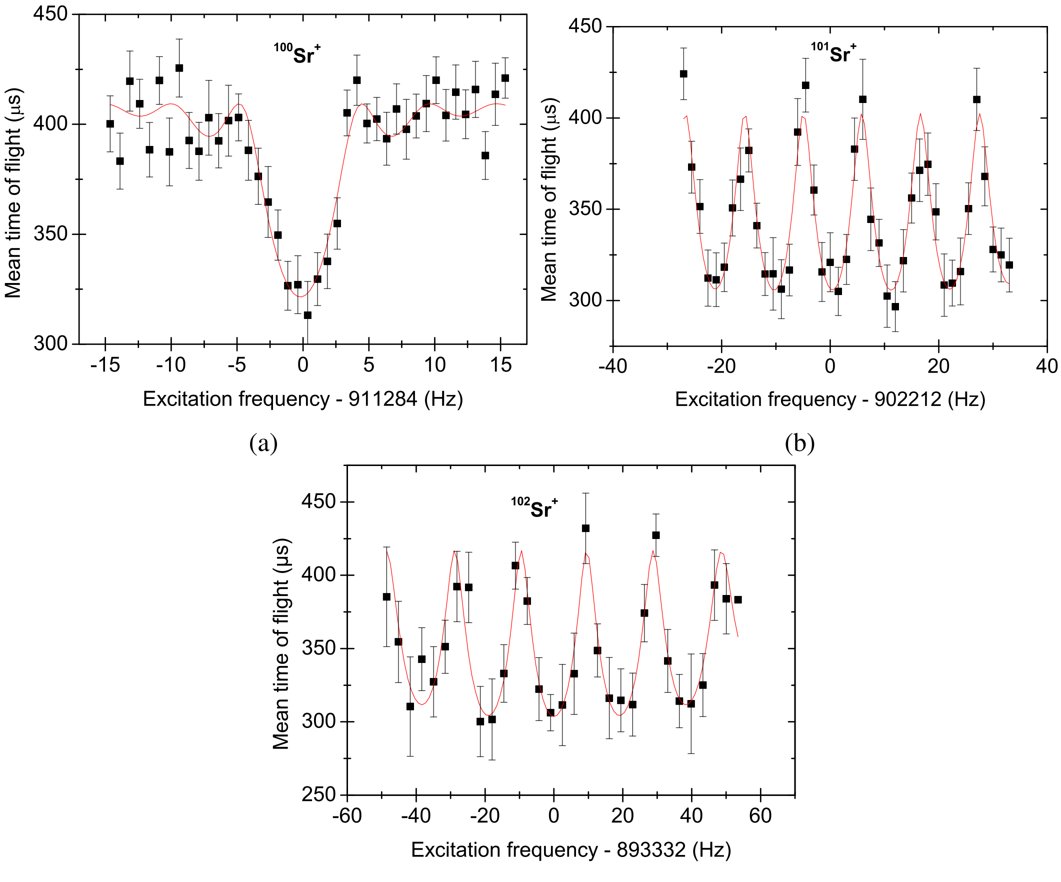

(a) (b)

(c)

Figure 3.10 – (a) Time-of-flight ion cyclotron resonance of ^{100}Sr for an excitation time of 200 ms. (b) Ramsey-type resonance of ^{101}Sr of 10 ms excitation time and 80 ms waiting time. (c) Ramsey-type resonance of ^{102}Sr of 10 ms excitation time and 40 ms waiting time. For all three resonances the corresponding fit curve is represented in red.

3.7 Discussion

In Figure 3.12a is shown the evolution of the mass surface along the Sr, Rb and Kr isotopic chains via the two-neutron separation energies (S_{2N}) in the region of nuclei of $A \approx 100$ [Wang 2012]. The new S_{2N} values calculated from the new mass measurements are added. In Figure 3.12b are plotted the mean-square charge radii in the same region, represented as differences to the isotope with $N = 50$ [Keim 1995, Thibault 1981, Buchinger 1990, Lievens 1991, Cheal 2007, Campbell 2002]. For clarity, the $\delta < r^2 >_{N,50}$ are plotted with an arbitrary offset with respect to the krypton isotopic chain.

In Figure 3.12a, the increase of the two-neutron separation energy at $N = 60$ for the Sr and Rb isotopic chains signals the sudden onset of collectivity in the ground state. The new S_{2N} values of the Sr and Rb isotopes show that the trend set at $N = 60$ continues at least as far as $N = 65$ without major structural changes. The shape transitions and the persistence of the ground-state deformations, up to $N = 62$, are visible also in the evolution of the mean-square charge radii, as shown in Figure 3.12b. Here it should be noted that $N = 66$ is the mid-shell between the magic neutron numbers $N = 50$ and $N = 82$.

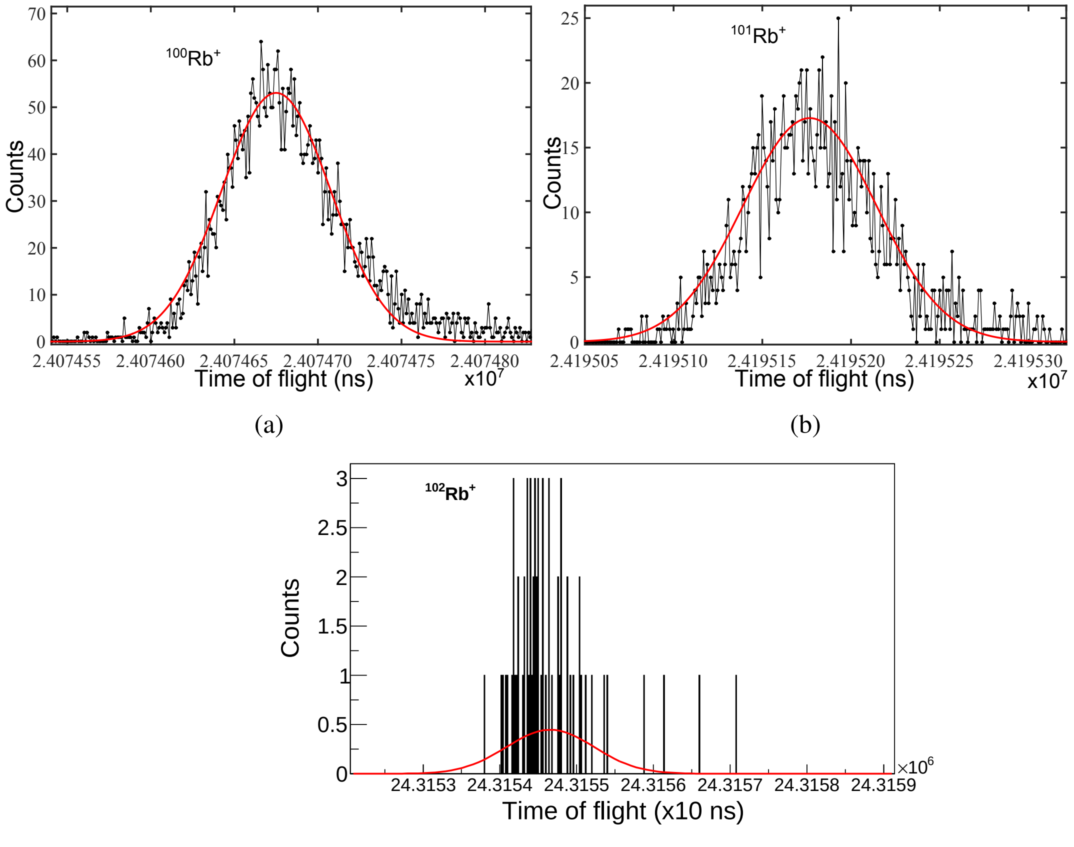

(a) (b)

(c)

Figure 3.11 – Time-of-flight spectra of ^{100}Rb (a), ^{101}Rb (b) and ^{102}Rb (c). For each time-of-flight spectrum, the number of revolution is 1000. The fit curves are represented in red.

Isotope (On-line ref.)	Half-life (ms)	C_{tof}	ME_{ISOLTRAP} (keV/c^2)	$ME_{AME2012}$ (keV/c^2)	$\Delta_{\text{ISOLTRAP-AME2012}}$ (keV/c^2)	ME_{TITAN} (keV/c^2)
^{100}Rb (^{100}Sr)	48(3)	0.50092961(112)	-46290(19)	-46550#(200#)	262(201)	-46190(140)
^{101}Rb (^{101}Sr)	31.8(3.3)	0.50081901(123)	-42558(28)	-42810#(220#)	256(222)	
^{102}Rb (^{102}Sr)	37(3)	0.50089852(295)	-37253(83)	-37710#(300#)	424(311)	

Table 3.2 – C_{tof} values of ^{100,101,102}Rb^{+} measured with the MR-TOF MS. The corresponding on-line reference is shown in brackets, the off-line reference is always ^{85}Rb^{+}. The corresponding mass excess (ME_{ISOLTRAP}) values are presented. The half-lives from NUBASE2012 [Audi 2012], and mass excess values (ME_{AME2012}) from AME2012 [Wang 2012] (# indicates extrapolated values) are also given. The ^{100}Rb mass has recently been measured by Penning-trap spectrometry, first by ISOLTRAP [Manea 2013] (the corresponding mass excess is $-46247(20)$ keV$/$c^2), and by TITAN [Klawitter 2016]. The mass excess value from the TITAN experiment ME_{TITAN} is shown in the table. These two recent mass excess values from ISOLTRAP and TITAN are not in the AME2012.

3.7.1 Comparison to theoretical models

In Figure 3.13 the experimental S_{2N} and $\delta < r^2 >_{N,50}$ for even-even nuclei are compared to theoretical models. The presented calculations are available only for even-even nuclei, therefore, the odd nuclei are not shown (and the evolution looks different). The presented models belong to the class of self-consistent mean-field approaches [Bender 2003] with two different effective interactions between

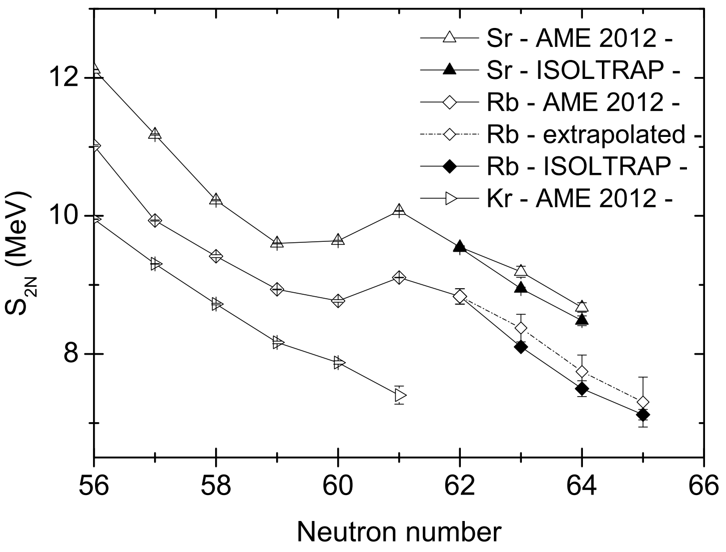

(a)

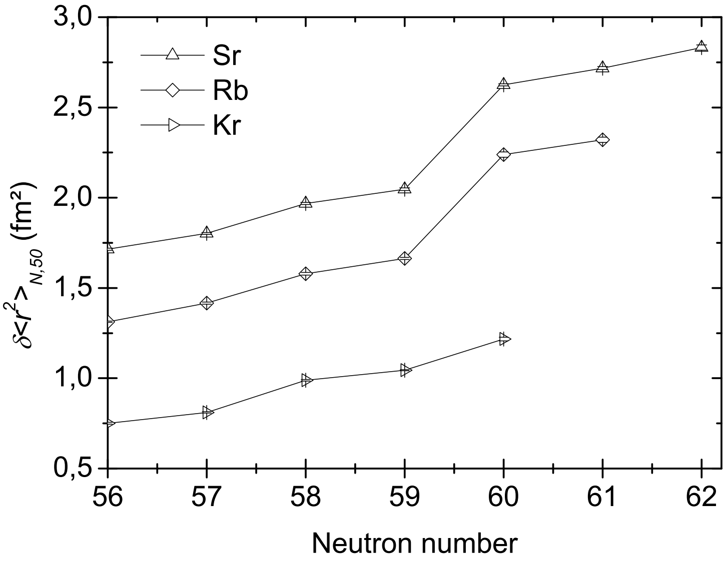

(b)

Figure 3.12 – (a) Experimental two-neutron separation energies in the $A \approx 100$ region. The experimental values from the AME2012 [Wang 2012] are shown with empty points, the newly reported values of strontium and rubidium are shown with solid points, the extrapolated values are shown with half-emptied points. (b) The changes in experimental mean-square charge radii $\delta < r^2 >_{N,50}$, relative to the corresponding $N = 50$ isotopes, in the same region [Keim 1995, Thibault 1981, Buchinger 1990, Lievens 1991]. To avoid the superposition of the $\delta < r^2 >_{N,50}$ curves, they are plotted with an arbitrary offset with respect to the krypton chain (+1 for the rubidium isotopic chain, +2 for the strontium isotopic chain).

nucleons: Skyrme and Gogny. Two parameterizations of the Skyrme interaction are shown: UNEDF0 (adjusted on spherical and deformed nuclei) [Kortelainen 2010], and UNEDF1 (optimized also on the excitation energies of fission isomers) [Kortelainen 2012]. For the Gogny interaction, only the D1S parametrization is shown [Dechargé 1980, Berger 1991]. The Gogny D1S+5DCH is a beyond mean-field calculation, which uses a five-dimensional collective Hamiltonian (5DCH) [Clément 2016].

Of the Skyrme effective interactions, the parametrization which gives the best description is UN-

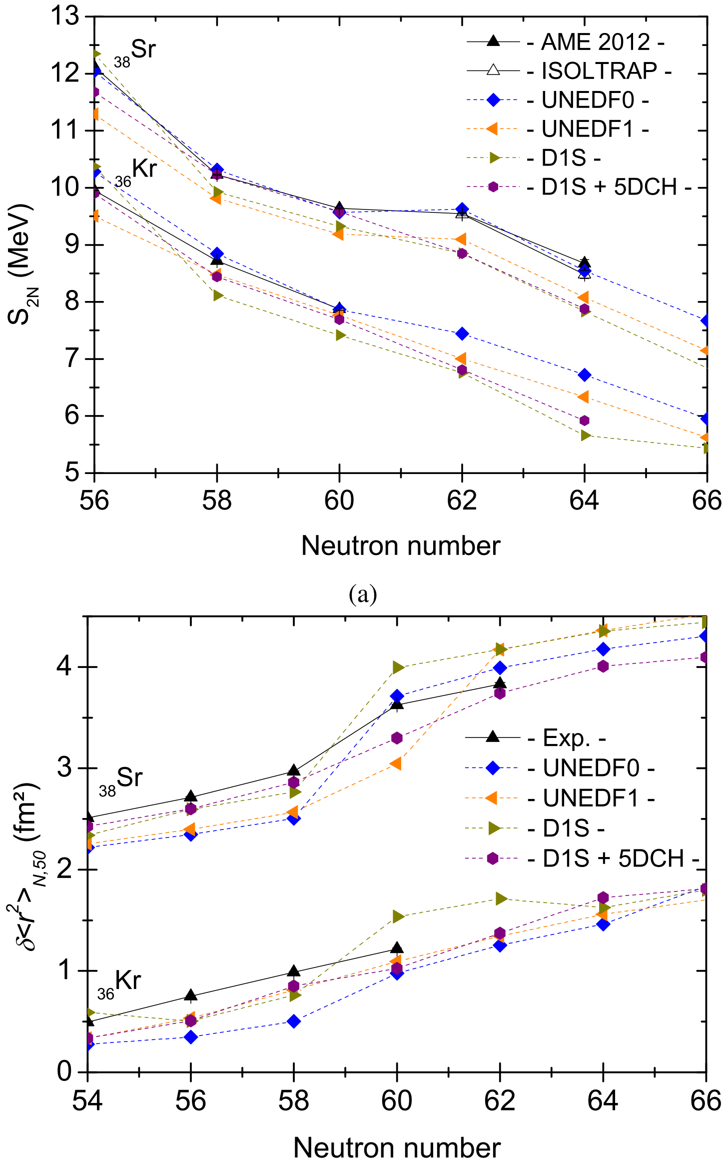

(a)

(b)

Figure 3.13 – Experimental two-neutron separation energies (a) and mean-square charge radii (b) of the even-even strontium and krypton nuclei. The data are compared to three self-consistent HFB calculations and one beyond mean-field calculation. Two models use the Skyrme nucleon-nucleon interaction, one with the UNEDF0 parametrization [Kortelainen 2010] and the second one with the UNEDF1 [Kortelainen 2012] parametrization. The two other models used the Gogny interaction with the D1S parametrization [Dechargé 1980, Berger 1991]. The beyond-mean-field calculation D1S+5DCH [Bertsch 2007] uses a mapping to a five-dimensional collective Hamiltonian.

EDF0. One can see in Figure 3.13 an excellent agreement between the experimental data and the model in the strontium isotopic chain (especially in what concerns S_{2N}). A less good agreement is found with the UNEDF1 model. Indeed, even if an onset of deformation can be noticed in the S_{2N} values of Sr, there is an offset of the calculated results from the experimental data.

The calculations with the Gogny effective interaction give a less good description of the onset of deformation. A sudden increase is predicted at $N = 60$ for the strontium charge radii, but not for the two-neutron separation energy. Furthermore, the introduction of the beyond mean-field calculations D1S+5DCH do not help to reproduce the onset of deformation.

The Skyrme density functional theory calculations predict that the shape transition taking place in the strontium isotopic chain is not existent (or at least much weaker) in the krypton isotopic chain. In the mean-field calculation D1S, a clear transition is predicted for ^{96}Kr $\delta < r^2 >_{N,50}$ (visible as a small increase of the ^{96}Kr charge radius). However, when including the beyond mean-field calculation, this effect vanishes.

3.7.2 Comparison to HFODD calculations

The state-of-the-art calculations presented so far allow discussing the overall trend of the ground-state properties along the isotopic chains of interest. However, in order to better understand this trend, it is worth also revealing the evolution with neutron number of the major intrinsic configurations in the region. Furthermore, the fact that odd nuclei are not computed limits somewhat the possibility of completely quantifying the strength of the increase in two-neutron separation energies across $N = 60$. In order to provide this missing information, HFB calculations were performed for the Sr and Kr isotopic chains. The time-reversal and symmetry-unconstrained HFODD [Schunck 2012] code and the SLy4 parametrization (of the Skyrme family) [Chabanat 1998], with a contact volume-pairing force, were used. The HFODD solver uses the expansion of the wave function in a harmonic-oscillator (HO) basis. Extensive documentation about the code can be found in the user's guide [Dobaczewski 2009a].

For this work a spherical basis of a maximum of 500 HO functions was used. The region of deformation was already studied with the HFODD solver and the SLy4 interaction in [Manea 2013]. But there the odd-A and the odd-odd nuclei were calculated in the so-called false vacuum interaction, meaning with fully paired wave functions [Duguet 2001]. As an extension to this work, here the odd-A nuclei are computed in the blocking approximation. This method, detailed in [Dobaczewski 2009b], allows a complete description of an odd nucleus via the overlap approximation. For each iteration of the code, the quasi-particle presenting the largest overlap with a single-particle state is blocked, i.e. a quasi-particle state in the HFB wave function is replaced with the state of opposite energy. It induces an occupation amplitude of one of the single-particle states equal to one. Therefore, this state no longer contributes to the pairing field and in this sense it is "blocked". Several different calculations of the same nucleus are required (in this case 11), each using a different single-particle state for the overlap criterion. At the end, the ground state of the odd nucleus is chosen as the solution of lowest energy.

3.7.2.1 Pairing interaction

The calculations were chosen to be performed with the SLy4 parametrization of the Skyrme interaction [Chabanat 1998] for the particle-hole part of the energy functional. The choice on this interaction was carried by its extensive use for the description of nuclei properties across the entire nuclear chart. Indeed, with the SLy4 parametrization, global calculations including particle/angular-momentum projection and configuration mixing for systematic studies of quadrupole correlation in even-even nuclei [Bender 2006] were performed. Systematic studies of pairing interactions were also performed for the particle-particle part of the energy functional [Dobaczewski 2001], as well as exploration of the limits of the nuclear chart in the super-heavy region [Cwiok 2005] and towards the drip lines [Erler 2012]. From all these existing results a solid reference basis is constituted which can be used for discussing the calculations presented in this work.

The density-dependent delta interaction (DDDI) [Dobaczewski 2001, Bender 2003] is an usual choice for the pairing interaction, responsible of the particle-particle part of the energy functional. It is expressed as follows:

$$V_{pair}(r_1,r_2) = V_0 \left\{ 1 - \left(\frac{\rho(r_1)}{\rho_c} \right)^{\beta} \right\} \delta(r_1 - r_2), \tag{3.37}$$

where $\rho(r_1)$ is the nuclear density. The pairing interaction (equation (3.37)) is function of three parameters, V_0 (which gives the overall strength of the interaction), and ρ_c and β which together define the distribution of the pairing strength as a function of the nuclear density. However, based on available data, it is very difficult to constrain the three parameters. Therefore, β is commonly chosen to be equal to 1 [Bender 2003]. From this approximation three types of pairing interaction can be identified, depending on the ρ_c value. For $\rho_c = 0.16\,\mathrm{fm}^{-3}$, the pairing becomes of surface type. For $\rho_c \to \infty$, the density dependence disappears and the pairing is of volume type. In the intermediate situation, the pairing is of mixed type. Here, the pairing was chosen to be of volume type. Equation (3.37) can thus be simplified:

$$V^{vol}_{pair}(r_1,r_2) = V_0 \delta(r_1 - r_2). \tag{3.38}$$

For the calculations presented in this work, the pairing interaction was adjusted in order to reproduce the odd-even staggering of the binding energies of Sn isotopes between $N = 67$ and $N = 73$, in a spherical calculation. This is the standard method and profits from the fact that, being a magic chain of isotopes, its structure can be computed more accurately in a spherical approximation. Therefore, without computing all the deformed solutions, one can get a good description of the odd-even staggering. Furthermore, the contributions of the pairing interaction are separated from the other parameters of the interaction, which are coupled in case of a deformed nucleus. Finally, the Sn isotopic chain is medium-mass, thus close to the region of interest.

An equal pairing interaction was chosen for protons and neutrons. The pairing interaction was calculated with values from $-150\,\mathrm{MeV\,fm}^3$ to $-200\,\mathrm{MeV\,fm}^3$, in steps of $10\,\mathrm{MeV\,fm}^3$, and the results were compared to the experimental data. The comparison between the experimental and calculated values for a pairing interaction of -180, -190 and $-200\,\mathrm{MeV\,fm}^3$ is shown in Figure 3.14. To make the comparison, the three-point estimator of the odd-even staggering is used, given by:

$$\Delta_{3N}(Z,N) = \frac{(-1)^N}{2} \left(B(Z,N-1) - 2B(Z,N) + B(Z,N+1) \right), \tag{3.39}$$

where B(Z,N) is the binding energy of the nucleus taken with a negative sign. The best agreement between experimental and calculated data was expected to appear for a pairing interaction of $-180\,\mathrm{MeV\,fm}^3$. However, it emerged that the best agreement was found for a value of $-200\,\mathrm{MeV\,fm}^3$ of the pairing interaction. The excellent agreement between the experimental and calculated data did not call for computing a lower value of the pairing interaction.

3.7.2.2 HFODD results

In Figure 3.15a the two-neutron separation (S_{2N}) energies resulting from the HFB calculations are compared to the available experimental data. In the calculations, both oblate and prolate solutions were found lying close in energy, in agreement with the results presented in [Rodríguez-Guzmán 2010a, Rodríguez-Guzmán 2010b], for a Gogny-type interaction, and with the results presented in [Manea 2013] for a Skyrme-type interaction.

Similarly to the HFODD calculations presented in [Manea 2013], the prolate solution describes the best the observed systematics of the two-neutron separation energies and mean charge radii beyond $N = 60$ for the strontium isotopic chain. In general, from the calculation outputs, two prolate configurations are found, depending on the neutron number range: one state for smaller deformation of $N < 60$, and one at larger deformation emerging at $N \sim 60$. One way to explain the shape transition is thus a change around $N = 60$ from low-deformation to high-deformation prolate shapes. Another explanation is that the shape

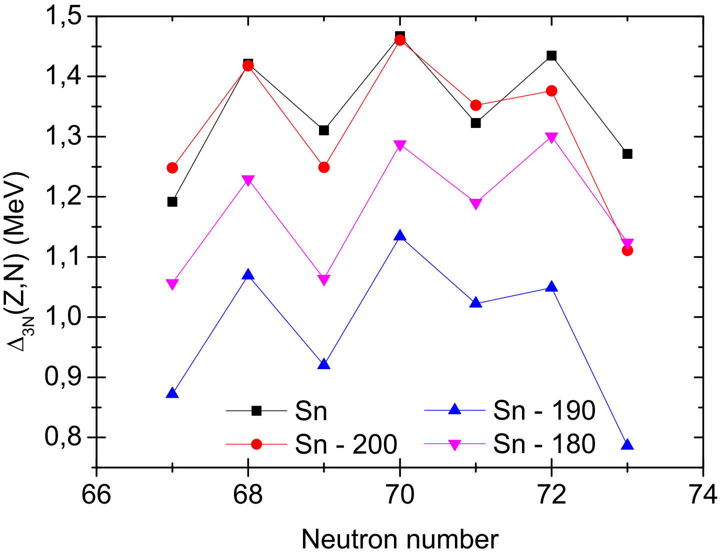

Figure 3.14 – Comparison between the experimental and calculated three-point estimator of the odd-even staggering for a volume pairing interaction of -180, -190 and -200 MeV fm^3.

transition takes place as a change between an oblate and a prolate shape. The calculations presented in Figure 3.15 favor the latter situation, because the oblate configuration is predicted to be lower in energy for $N < 60$. However, if one simply assigns the ground state of each isotope to the configuration of lowest energy the strength of the effect in S_{2N} at $N = 60$ is underestimated. This is because the change in binding energy which accompanies the oblate-prolate transition is not strong enough.

Concerning the krypton isotopic chain, the oblate solution describes best the observed systematics of the two-neutron separation energy and mean-square charge radii. This is in agreement with the UNEDF0 and UNEDF1 calculations which predict oblate shapes for the krypton isotopes with $N < 60$.

One must note however that the spectroscopic quadrupole moments determined by laser spectroscopy [Keim 1995, Thibault 1981, Buchinger 1990] are positive for $N < 60$, indicating a prolate nature of the ground state. This could point to the fact that the ordering in energy between the two configurations is incorrectly predicted by the HFB calculations, or that beyond-mean-field configuration mixing is very important for the nuclei with $N < 60$. We note that the UNEDF0 and UNEDF1 calculations predict almost spherical shapes for strontium isotopes with $N < 60$.

The krypton isotopes are predicted to have an oblate deformation, see Figure 3.15. Nevertheless, a transition between weakly deformed and strongly deformed shapes is still predicted to take place in the prolate solution for higher neutron number: $N = 61, 62$, see Figure 3.15b. Measurements of heavier krypton isotopes (^{98}Kr and further) are thus mandatory in order to clarify their shape evolution towards the neutron mid-shell ($N = 66$) and to establish whether the krypton chain is indeed the critical boundary of the prolate shape transition of the region of deformation [Naimi 2010b, Manea 2013].

The evolution of the intrinsic deformation of even-even krypton isotopes [Rodríguez 2014] has been studied via the so-called symmetry-conserving configuration-mixing (SCCM) method with the Gogny D1S interaction. The purpose was to explore the triaxial degree of freedom of the krypton isotopes beyond the mean field. It was found that at the mean-field level the triaxiality of ^{98}Kr is low and that beyond the mean field, the wave functions of the bands built on the ground and first excited 0^+ states are dominated by the oblate and prolate configuration, respectively. This means that the fingerprints of the static intrinsic shapes of the krypton isotopes might be traceable at the level of the ground-state observables beyond $N = 60$.

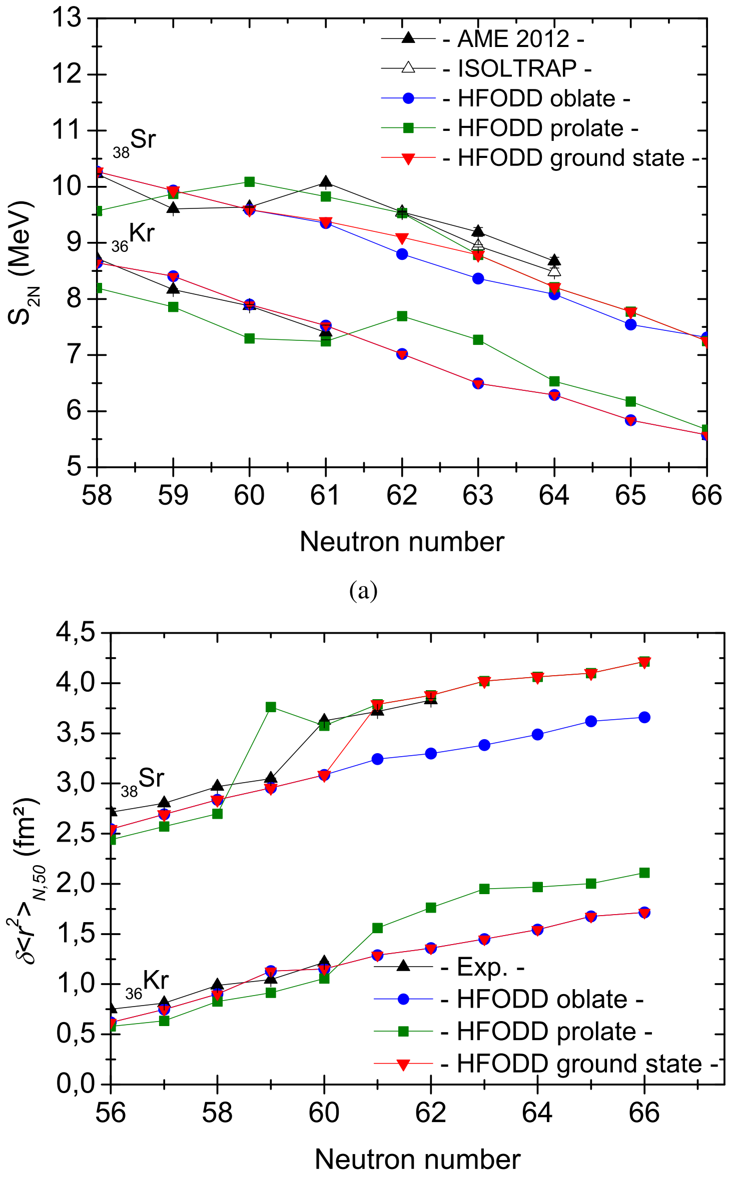

(a)

(b)

Figure 3.15 – Comparison of the experimental two-neutron separation energy (a) and mean-charge square radii (b) in the region $A \approx 100$ with HFODD calculations. The experimental values from the AME2012 [Wang 2012] are shown with black solid points, the newly reported values of strontium and rubidium with empty points, and the calculated values with colored solid points. The ground state, prolate-deformed and oblate-deformed solutions are shown.

3.8 Conclusions and outlook

In this work we presented the mass measurements of ^{100,101,102}Rb and ^{100,101,102}Sr performed at the ISOLDE/CERN facility with ISOLTRAP by using the MR-TOF MS for the rubidium masses, and the precision Penning trap for the strontium masses. The masses of isotopes ^{102}Sr, ^{101}Rb and ^{102}Rb were measured for the first time. The measured rubidium and strontium masses confirm the trend in the region of deformation well beyond $N = 60$, approaching the nuclear mid-shell.

The new S_{2N} values of the Sr and Rb isotopes show that the trend set at $N = 60$ continues at least as far as $N = 65$ without major structural changes. This conclusion is also supported in the strontium isotopic chain by the recent identification of the level scheme in ^{102}Sr [Wang 2016].

The identification of whether the "southwest" border of the region of deformation is in the krypton isotopic chain or the rubidium isotopic chain is an open question. The masses of ^{96,97}Kr were precisely measured for the first time in 2010, see [Naimi 2010b], and no sign of deformation was found. Therefore, ^{97}Rb has been defined as the lightest deformed $N = 60$ isotone, a fact also supported by the recent article from C. Sotty *et al.* [Sotty 2015].

Different self-consistent mean-field approaches (including a beyond mean-field approach) with different Skyrme and Gogny effective interactions are presented. The calculations with the different nucleon-nucleon interactions (namely Skyrme and Gogny) tend to reproduce the even-even nuclei in the region of interest. Furthermore, HFB calculations with the HFODD solver and the SLy4 Skyrme interaction were shown for the odd-N krypton and strontium isotopes. The prolate solution gives a good agreement with the experimental strontium data and the oblate solution gives a good agreement with the krypton isotopic chain, but the calculation predicts the oblate solution to be lower in energy for $N < 60$, which attenuates a lot the increase in S_{2N} at the shape transition point. Furthermore, these calculations exclude the krypton chain from the region of strong deformation, but a transition between weakly deformed and strongly deformed shape is still predicted to take place in the prolate solution for higher neutron number: $N = 61, 62$.

The region of deformation is a hot topic since many years. Recently, results of studies carried out by [Rodríguez 2014, Sotty 2015, Clément 2016, Wang 2016], including the one presented in this work, are confirming the continuity of the nuclear ground-state deformation beyond $N = 60$ in the isotopic chains of zirconium, yttrium, strontium and rubidium. Up to now, no shape transition was observed in the isotopes of krypton. However, the recently published results from [Rodríguez 2014] predict shape coexistence to occur in ^{98}Kr. The measurement of heavier krypton isotopes is the next step in order to highlight whether the "southwest" border of the deformation is ^{97}Rb or ^{98}Kr. The determination of the border will allow to better constrain models dedicated to nuclear deformation.

CHAPTER 4

Development of an electrospray ionization ion source

Contents

4.1 Introduction

At the end of the 1960's, M. Dole and his colleagues developed a method to form gas-phase of charged macromolecules by evaporation without heating process (heating a macromolecule always degrades it before the evaporation). The idea was to use the electrospray ionization process, which consists of applying a high voltage to a liquid to create an aerosol containing charged droplets. A dilute solution of the wanted molecules was thus electrosprayed into an evaporation chamber containing nitrogen. The volatile solvent evaporates, and the macroions (charged macromolecules) were suspended in the gas-phase as a mixture of solvent and nitrogen molecules [Dole 1968, Mack 1970, Clegg 1971, Teer 1975]. The technique was demonstrated to be very effective and from polystyrene molecules, ranging in mass from 200 to 860000 u, an ion current from 10^{-14} to nearly 6×10^{-13} A was obtained.

Nowadays, the production of molecular ion beams of any masses via the electrospray ionization technique is commonly used in different fields (biology, chemistry, physics...). The development of this technique for the purpose of analyzing biological macromolecules was rewarded with the attribution of the Nobel Prize in Chemistry to John Bennett Fenn in 2002.

Recently, an MR-TOF MS has been developed for mass measurements of short-lived nuclei at the RIKEN accelerator facility [Ishida 2004, Ishida 2005, Schury 2009]. The MR-TOF MS is installed at the gas-filled recoil separator GARIS and is dedicated to mass measurements of super heavy elements. As explained in section 3.5.1, the mass determination with an MR-TOF MS requires at least one isotope of well-known mass as reference. In the best scenario two well-known isobars of the species of interest present in the beam are used as references. However, the trans-uranium elements (for example) do not have atomic isobars with half-lives long enough and/or a mass sufficiently well known to be used as references. Therefore, one has to use an off-line ion source to provide these references. Furthermore, the smaller is the mass difference between the ion of interest and the reference ion, the smaller are the mass dependent systematic uncertainties. An ion source producing reference ions, being isobars of the species of interest, would thus be a tool of choice.

By electrospraying a solution made out of alcohol and tap water, one can expect a broad mass range production of stable molecular ions, from 10 u to 1000 u, at least. With this method, the mass range is wide, and one can easily select one of the produced molecular ions as reference for a mass measurement. Such an electrospray ionization (ESI) ion source has been developed at RIKEN [Naimi 2013]. An example of the mass production range obtained is shown in Figure 4.1.

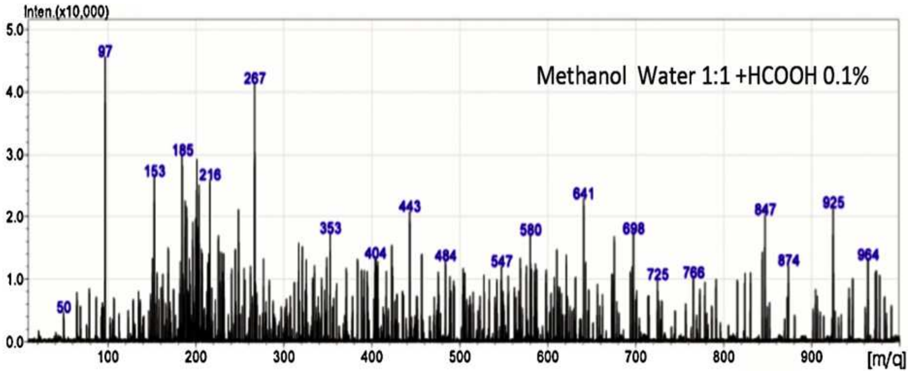

Figure 4.1 – Molecular ions produced from a solution of methanol and tap water (1:1) and formic acid (0.1% of the total volume) obtained via the ESI ion source installed at RIKEN. Figure from [Naimi 2013].

In a conventional ESI ion source, the molecular ions are created via the electrospray process and they are regrouped as a beam and transfered to the high vacuum region by a skimmer. This device is an rf ion-guide having a funnel shape and made of ring electrodes to which rf and dc voltages are applied to drive the ions. The fundamental principle is the same as for a linear Paul trap, see section 2.3. However, after the RIKEN ESI ion source a radiofrequency carpet (rf-carpet) [Wada 2003, Takamine 2005] has been installed instead of a skimmer. The rf-carpet, via its small aperture ($\sim$ 0.5 mm), allows to negate the need for a sophisticated pumping system. Furthermore, it also has the advantage of having a simple geometry and being a very small device (comparable size to a CD) as compared to a skimmer.

The RIKEN ESI ion source coupled to the rf-carpet was demonstrated to be efficient in the beam production and extraction of molecular ions. Furthermore, the mass production range was large enough to use the molecular ions produced as isobaric reference ions for the MR-TOF MS. One should note here that in the following the two terms "isotope" and "isobar" are used to differentiate the mass of two molecular ions. Two molecules are defined as isotopes if their mass difference is of 1 u, or as isobar if they have the same atomic mass number.

An upgraded version of the RIKEN ESI ion source was developed at the Max-Planck-Institut für Kernphysik at Heidelberg. This new ESI ion source is designed to be adaptable at ISOLTRAP at ISOLDE/CERN [Mukherjee 2008] where it can provide reference ions for MR-TOF MS mass measurements. It is also planned to install it at the CSR (cryogenic storage ring) at MPIK [von Hahn 2016], where it will be used to produce and investigate biomolecules. In the following the experimental setup will be described and the first characterization of the source will be presented.

4.2 Experimental setup

The ESI ion source is constituted of an electrospray ionization system, an rf-carpet and a quadrupole mass spectrometer (QMS). Photos of the experimental setup are shown in Figure 4.2, and a scheme of the setup is presented in Figure 4.3. The principle is the following: A solution is electrosprayed by the

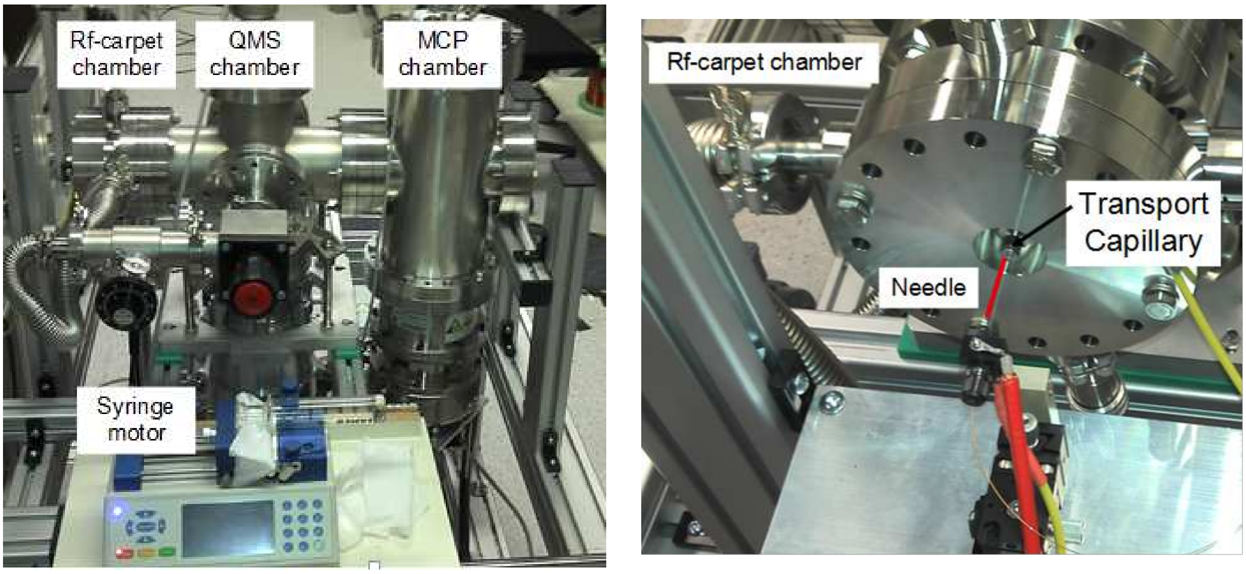

(a) (b)

Figure 4.2 – (a) Photo of the ESI setup. One can see a glass syringe with its driving motor and the three vacuum chambers: the rf-carpet chamber, the QMS chamber and the MCP chamber. (b) Zoom on the electrospray ionization part and the transport capillary in front of the rf-carpet chamber. The needle is highlighted in red, which makes it more visible on the photo.

ESI system, the rf-carpet collects the ions and guides them into the QMS for mass separation. At the end, the ion beam is detected with a combination of an MCP and a phosphor screen. Every part of the set-up will be described in the following.

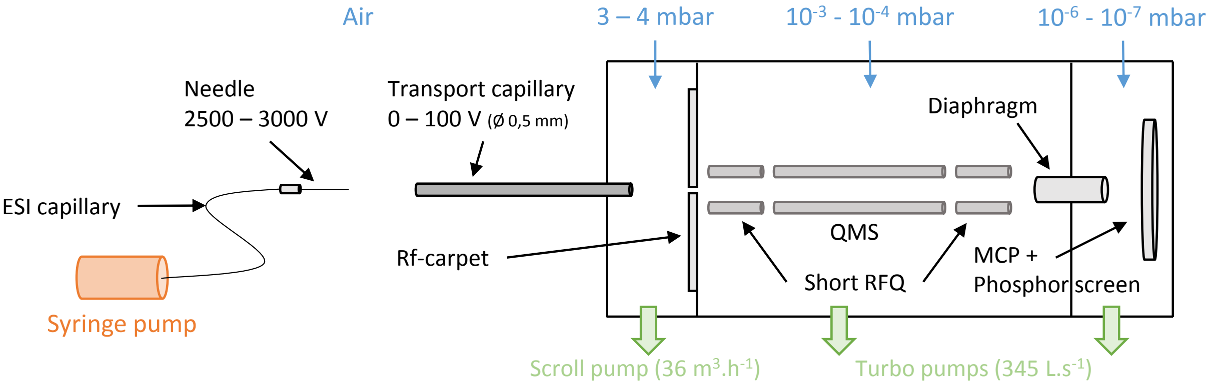

Figure 4.3 – Sketch of the ESI source. The solution is pushed from the syringe to the needle by a motor. A high voltage is applied on the needle and a few tens of volts can be set on the transport capillary. The created electric field, as high as 10^6 V/m, attracts the ions inside the transport capillary. The rf-carpet allows to transport the ions to the carpet's exit hole. The short RFQs are ion guides and the QMS is dedicated to the isotopic mass separation. The detection is performed with an MCP.

4.2.1 ESI section

The molecular ions production starts with the preparation of a solution. A sample (deionized water or tap water) is dissolved in a solvent (methanol or isopropanol) with a ratio of (1:1) and formic acid is added (1% of the total volume) to favor positively charged ions. A motor driven syringe pump injects the solution through the ESI capillary up to a needle (inner diameter of 100 µm) on which a high voltage is set ($\approx 2.5 - 3$ kV). The applied potential polarizes the molecules near the exposed surface, forcing the liquid to point downfield and to form a so-called Taylor cone [Taylor 1965, De La Mora 1994]. At the tip of the cone the repulsion between positive charges increases, causing instabilities thus forming droplets, with approximately the same size as the cone's tip. The electric field created between the needle and the transport capillary (as high as 10^6 V/m) attracts these charged droplets. During the transport the solvent evaporates, reducing the droplets size up to the Rayleigh limit radius [F.R.S. 1882]. The Coulomb repulsion overcomes then the surface tension and droplet explosions occur. It leads to jets of even smaller charged droplets, which undergo cycles of evaporation until the gas-phase ions are formed [Iribarne 1976]. A schematic representation of the droplets formation is shown in Figure 4.4. The pressure gradient transports the ions through the transport capillary up to the rf-carpet. The transport through this capillary was studied and optimized. This work is summarized in section 4.3.1.2.

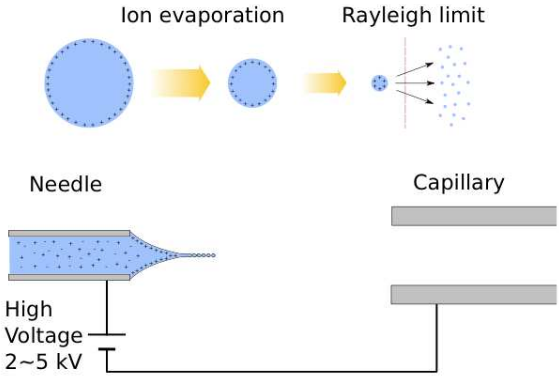

Figure 4.4 – Schematic representation of the droplets formation via the electrospray process. For details, see text.

4.2.2 Transport, selection and detection

4.2.2.1 Rf-carpet

The rf-carpet consists of a planar printed circuit board with 54 concentric ring electrodes, each of them having a radius of 0.15 mm, with a pitch of 0.3 mm, as shown in Figure 4.6. The rf-carpet stops the scattered molecular ions above its electrodes and drives them to its center exit hole, an aperture of 0.5 mm diameter.

The rf signals are applied on the electrodes such that adjacent electrodes are 180° out of phase. Via the combination of the inhomogeneous rf-field, a dc gradient between the outermost and inner electrodes, and the gas pressure in the chamber, the ions are transported to the center of the carpet. The double effect of the rf-signal and the pressure keeps the ions slightly above the electrodes. If the pressure is too high, the ions crash onto the electrodes. If the rf-amplitude is too high, the ions are repelled and lost in the chamber. Finally, if the rf-frequency is not adapted to the expected mass range, the ions will not be guided, their motion being unstable. The dc gradient superimposed to the rf-signal guides the ions to the aperture. As an example, a simulation of $^{11}\mathrm{Li}^+$ trajectory above rf-carpet electrodes is shown in Figure 4.5. This simulation was performed in the framework of the ESI ion source development at RIKEN by Takamine [Takamine 2007]. The rf-signal frequency is 16 MHz with an amplitude of $V_{rf} = 190\ V_{pp}$. The superimposed dc gradient is 12 V/cm. The pressure is 146 mbar of He gas at 300 K.

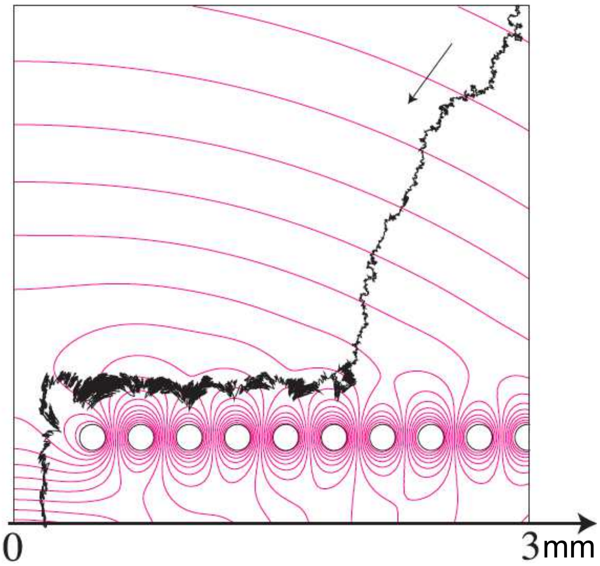

Figure 4.5 – Simulated $^{11}Li^{+}$ trajectory above the rf-carpet electrodes. The rf-frequency applied on the carpet electrode is 16 MHz at $V_{rf} = 190\ V_{pp}$. The superimposed dc gradient is 12 V/cm. The pressure is 146 mbar of He gas at 300 K. Figure from [Takamine 2007].

Similarly to a linear Paul trap, the ion motion above the rf-carpet electrodes is stable within a limited parameter space of dc and rf voltages, and can be described by the well-known Mathieu's equations (see section 2.3.2). However, the gas pressure must also be taken into account to find the stability region, which is determined by the two dimension-free parameters $(a - p^2)$ and q defined as [Takamine 2007]:

$$a - p^2 = \left(\frac{2eU_{\text{dc}}}{mr_0^2\omega_{\text{rf}}^2}\right) - \left(\frac{e}{m\mu\omega_{\text{rf}}}\right)^2 \tag{4.1}$$

$$q = \frac{4eV_{\text{rf}}}{mr_0^2\omega_{\text{rf}}^2}, \tag{4.2}$$

where e, m and μ are the electric charge, mass and mobility of the ion, respectively, and U_{dc}, V_{rf} and ω_{rf} are the dc voltage, rf-amplitude and angular frequency applied on the electrodes, respectively. r_0 is related to the distance between adjacent electrodes. The inhomogeneous rf-field can be described by electric pseudo-potential wells with a maximum average effective force approximated in high pressure by [Wada 2003]:

$$\bar{F}_{\text{hp}}^{\text{max}} = -\frac{1}{4}m\mu^2\frac{V_{\text{rf}}^2}{r_0^3}. \tag{4.3}$$

The rf-carpet pseudo-potential makes a corrugated shape, with the troughs being centered on the electrodes. In order for the pseudo-potential approximation to be valid, an ion must spend several oscillations of the field in the vicinity of a single trough. Efficiently transporting ions to the rf-carpet exit hole by having the required pseudo-potential depth makes the pressure and rf fields critical parameters for stable ion motion. A detailed discussion about the ion motion stability above the rf-carpet can be found in [Schwarz 2011].

From the Mathieu's parameters (Equation 4.1 and equation (4.2)) it can be inferred that the transmission of molecular ions having a mass between 1 u and 300 u requires a gas pressure of a few millibars (between 1 and 5 mbar), a frequency between 1 and 5 MHz with a maximum rf-amplitude of 450 V between neighboring electrodes, and a dc gradient of maximum 3 V/mm to guide the ions to the aperture.

In this work, to operate the rf-carpet, a toroidal coil was used to create the two opposite phases of the rf at a resonance frequency of 1.71 MHz. A dc gradient lower or equal to 3 V/mm was superimposed to the rf-signals between the outermost ring and the center ring electrode. A voltage divider was mounted around the carpet electrodes (via the resistors - Figure 4.6), to create the dc gradient. The coupling between the rf and dc signals was made by capacitors.

The pressure level in the chamber of $3-4$ mbar is obtained with an oil scroll pump of $36\,\mathrm{m}^3\,\mathrm{h}^{-1}$ pump power. The gas pressure cannot be decreased (due to the pump power), nevertheless, a valve has been added to the vacuum chamber which can be used to increase slightly the pressure if needed. When the ions reach the rf-carpet exit hole, they are pulled into the second chamber, where the QMS will provide a mass selection.

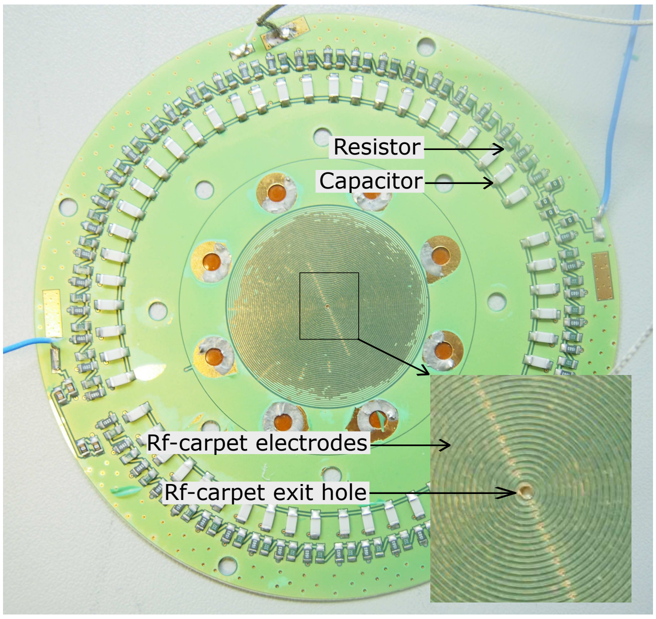

Figure 4.6 – Photo of the rf-carpet. The resistors and the capacitors needed for the dc gradient and the coupling between the dc and rf are all around the carpet. The electrodes are gold plated. The exit hole in the middle of the rf-carpet (see insert) has a diameter of 0.5 mm.

4.2.2.2 Quadrupole mass spectrometer

As mentioned in the introduction, this source is suited to deliver a large range of isobaric reference ions for mass calibration purposes. Nevertheless, all the masses are produced at the same time. A mass selection with a sufficiently high resolution to separate isotopes is thus needed. One should note here that many molecules can have the same atomic mass number. Therefore, after an isotopic mass separation the different molecules produced by the ion soure are not identified. To do so, one would need an isobaric mass separation, which can be performed with an MR-TOF MS for example. In this work, only the isotopic mass selection is considered.

Coming back to the isotopic mass selection, the rf-carpet frequency can be tuned for a specific mass range [Naimi 2013] but it cannot be used as an isotopic mass separator. This is why a QMS is located after the carpet, in the so-called QMS chamber. It has been designed and machined to be relatively short; 200 mm length with an inner radius of 3.55 mm. As shown in Figure 4.7, it is surrounded by two short RFQs, which are ion guides helping to inject and eject the ions.

The rf-carpet exit hole, acting like a pumping barrier, does not allow a pressure lower than 10^{-4} mbar in the QMS chamber. This vacuum quality has a strong impact on the QMS transmission and resolution. Simulations were performed with SIMION® [D. Manura 2008], for particles with a mass of 50 u, to estimate the effects of the gas pressure. For a gas pressure of 10^{-5} mbar the transmission is estimated around 80%. If it increases up to 10^{-4} mbar only 25% of transmission is expected. A pressure of 10^{-4} mbar in the chamber induces a maximum theoretical resolution of a few hundreds, which is sufficient to separate isotopes. This resolution could not be achieved with the actual setup. The justification as well as solutions to improve the resolution are discussed later.

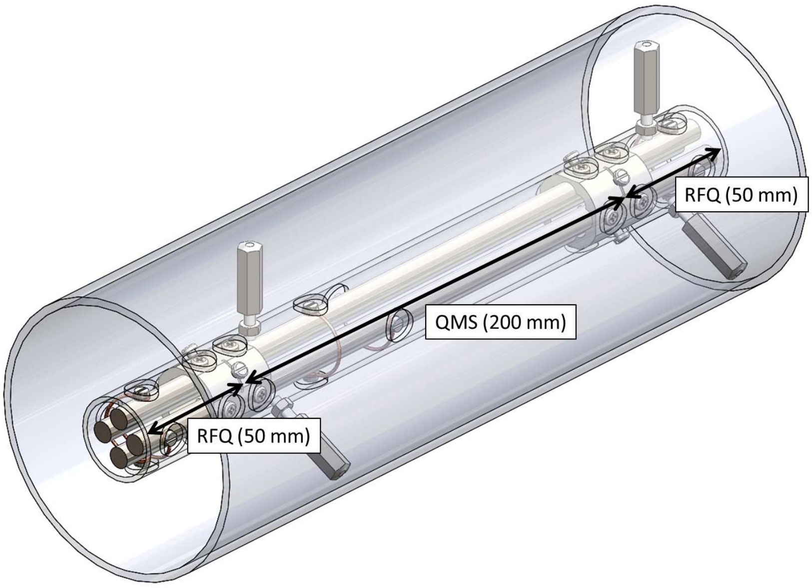

Figure 4.7 – Design of the QMS. At the entrance and the exit two small RFQs of 50 mm length are attached. The QMS is 200 mm long and its inner radius is 3.55 mm.

4.2.2.3 Diagnostics

Faraday cup Two Faraday cups were especially made to monitor the ion beam after the transport capillary and after the rf-carpet, see Figure 4.8a and Figure 4.8b, respectively. The Faraday cup used after the transport capillary is fixed with four rods on the flange in place of the rf-carpet. Using fixation rods for this Faraday cup allowed a tunable position. This helped to define a gap between the exit of the capillary and the Faraday cup. The second Faraday cup can be inserted just behind the rf-carpet, so that the ions current can be picked up after the rf-carpet exit hole.

MCP detector As it will be mentioned in section 4.3.1.2, a maximum of 20 pA could be transmitted by the carpet, i.e. reaching the QMS entrance. Therefore, considering the maximum QMS transmission of 25% (see previous paragraph), a maximum signal of 5 pA without mass separation is expected after the QMS. It becomes obvious that a Faraday cup associated to a picoAmperemeter would not be sensitive enough for the detection of mass separated ions. Therefore, an MCP detector associated to a phosphor screen was used for the ESI source commissioning.

The MCP and the phosphor screen located in the last chamber are shown in Figure 4.9. A positioning system was designed, the position can thus be defined and the gap between the diaphragm's end and the MCP can be tuned. The idea is to put the MCP as close as possible to the diaphragm, (10 mm in this case) which reduces ion losses due to the dispersion.

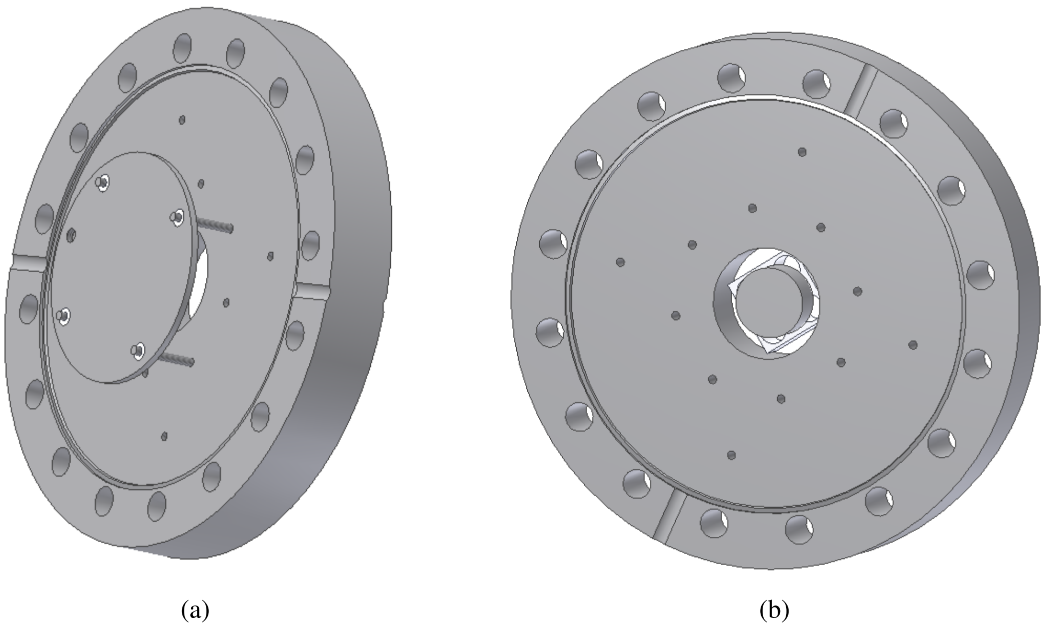
(a) (b)

Figure 4.8 – Homemade Faraday cups. (a) The Faraday cup is screwed on the flange where the rf-carpet is supposed to take place. It is used to detect the ion beam at the exit of the transport capillary. (b) The Faraday cup can fit a few millimeters behind the rf-carpet. It is used to detect the ion beam after the rf-carpet exit hole.

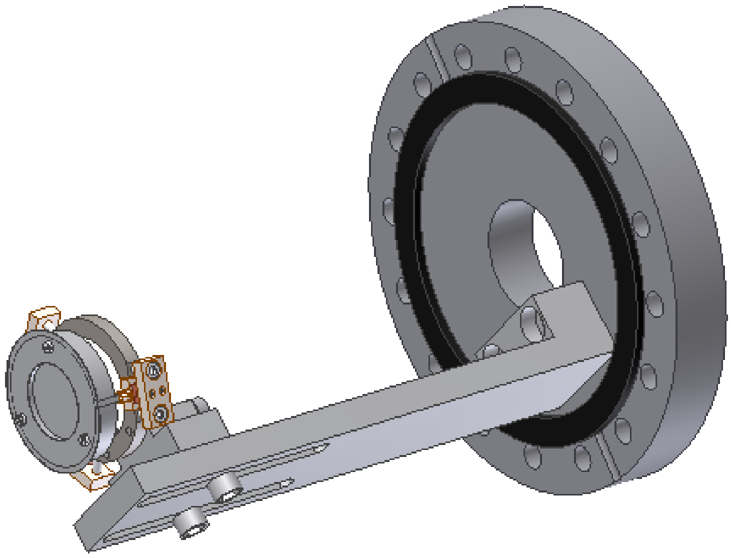

Figure 4.9 – An Inventor LT™ view of the MCP support. It is attached to the last CF100 flange of the setup. One can see two rails with two screws on the bottom side for the axial positioning system.

Diaphragm The maximum pressure required for the MCP operation is 10^{-5} mbar. Therefore a diaphragm has been installed between the QMS and the MCP chambers, to act as a pumping barrier. The diaphragm consists of an M8 rod with an inner diameter of 4 mm and a length of 140 mm, screwed in the middle of a CF 100 flange. The installation of this diaphragm allowed a reduction of the gas pressure in the MCP chamber down to 10^{-7} mbar. The diaphragm is insulated from the setup by a PEEK component, so that it can be used as a lens.

CCD camera A window flange CF40 was installed at the end of the setup. The early beam optimization was done by visualizing at the phosphor screen. Thereafter, the combined use of the window flange and a mirror permitted an installation of a CCD camera, which led to the possibility of automatic mass scans. This will be discussed later.

4.3 Ion source commissioning

4.3.1 Characterization of the electrospray ionization section

This section concerns studies on the electrospray ionization part of the set-up. First of all, the transport capillary geometry has been studied. This is indeed crucial for the transmission and the evaporation of the ions but also for the differential pumping, the capillary being the transition part between ambient air and vacuum. A first characterization of the beam has been performed by testing different parameters of the setup. The stability of the beam intensity was also studied.

4.3.1.1 The pressure in the setup

The ESI setup is divided in four parts (Figure 4.3) with different pressures:

- The ESI part in ambient air
- The rf-carpet chamber separated from ambient air by the transport capillary
- The QMS chamber separated from the previous one by the rf-carpet
- The MCP chamber separated from the previous one by the diaphragm

A differential pumping between the chambers is created by an oil scroll pump (36 m^3h^{-1}) for the rf-carpet chamber and two turbo pumps (345 Ls^{-1}), one for the QMS chamber, one for the MCP chamber. As mentioned in section 4.2.2.1, for a proper operation of the rf-carpet, a pressure between 1 and 5 mbar is mandatory. The transport capillary being the transition part from air to the first low pressure region, the gas pressure in the rf-carpet chamber is linked to the capillary geometry. A comparison of the pressure gradient obtained with three different capillary lengths is shown in Table 4.1. The transport capillary geometries were chosen to be 50 mm, 100 mm and 300 mm length keeping an inner diameter of 0.5 mm. As expected, a lower pressure in the rf-carpet chamber is measured when a longer transport capillary is used, 2.6 mbar for a 300 mm capillary length. A shorter capillary (50 mm) induces a pressure increase in the rf-carpet chamber to 4.9 mbar. This gas pressure is at the edge of the maximum pressure allowed (5 mbar) for a good operation of the rf-carpet. A transport capillary of 50 mm length is thus the shortest length one can use.

One can see that the pressure level in the rf-carpet chamber has an impact on the pressure level in the QMS chamber. In other words, the transport capillary length has an influence on the QMS transmission (see section 4.2.2.2).

All three capillaries shown in Table 4.1 can be used for the upcoming tests. The pressure condition for the rf-carpet chamber (between 1 and 5 mbar) is reached with all three capillaries. Despite the increase of the pressure in the QMS chamber as a function of the capillary length (maximum of pressure for a capillary of 50 mm length), the QMS can be operated in any cases.

The pressure in the MCP chamber is also impacted, however it is not discussed as the required minimum gas pressure for an MCP ($1x10^{-5}$ mbar) was reached in any case, independently of the capillaries length.

Capillary	*Rf carpet chamber*	*QMS chamber*	*MCP chamber*
300 mm	2.6 mbar	$5.5\text{x}10^{-4}$ mbar	$7.4\text{x}10^{-6}$ mbar
100 mm	3.9 mbar	$9.4\text{x}10^{-4}$ mbar	$7.9\text{x}10^{-6}$ mbar
50 mm	4.9 mbar	$1.2\text{x}10^{-3}$ mbar	$9.7\text{x}10^{-6}$ mbar

Table 4.1 – Pressure reached in the three different chambers as a function of the capillary length.

4.3.1.2 Ion transmission studies

First of all, every time the ESI source is in use, one question has to be kept in mind: is the ion signal observed coming from the ionized solution? If the high voltage set on the needle is too high (more than 3 kV) there are indeed more chances to ionize the ambient air surrounding the needle, starting another electrospray process on top of the one from the ionized solution. A simple way to avoid any suspicion when a signal is observed is to turn off and on again the syringe motor. When the motor is off the signal should vanish and come back when the motor is on again. A typical example of these kinds of tests is shown in Figure 4.10. It takes a few minutes for the signal to appear/disappear after the motor is on/off, respectively. Even if the syringe motor is turned off, a part of the solution remains inside the needle. As the high voltage is continuously applied on the needle, the ESI process is still ongoing and molecular ions are produced. Once the needle has been emptied, the ion signal vanishes. When the motor starts, the opposite effect occurs; it takes some time for the needle to be filled again with the solution. These effects due to the on/off switching of the motor are the fluctuations pointed out by the red circles in Figure 4.10. This test was done every time the high voltage and/or the position of the needle were changed.

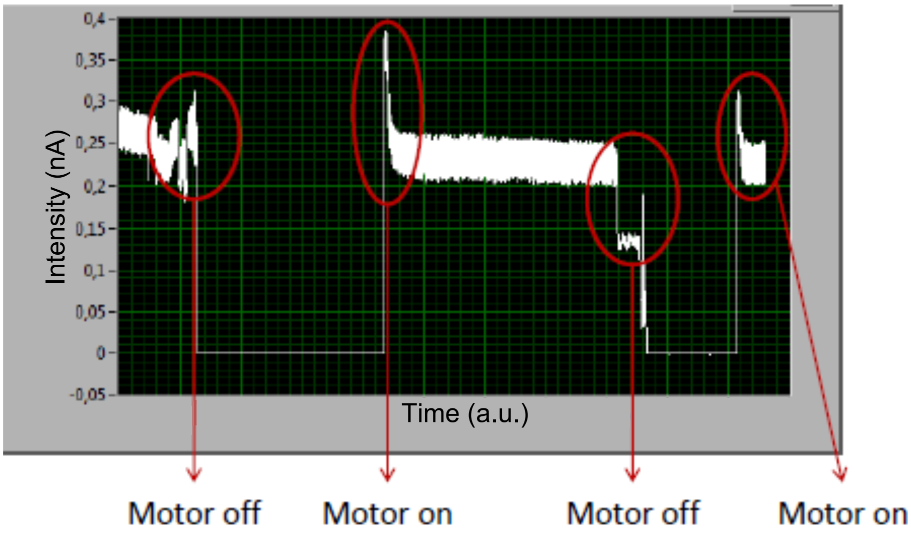

Figure 4.10 – Ion current picked up with a Faraday cup as a function of time. The vertical axis is the intensity (nA) of the signal recorded by the picoAmperemeter. When the syringe motor is turned off, it takes some time ($1-2$ minutes) before the signal decreased. When the motor is started again, it also takes time for the signal to be stable again (shown by the red circles).

The influence of the following parameters linked to the electrospray ionization process was investigated:

- the length of the capillary
- the flow rate $Q_{syringe}$, which defines the amount of available solution in the needle

- the voltage on the needle V_{needle} and the gap between the needle and the capillary $Gap_{needle-capillary}$, which define the electric field attracting the droplets.

All these studies were performed for different transport capillary lengths, thus for different pressures in the rf-carpet chamber. The results are shown in Table 4.2.

The detector used for these studies was the homemade Faraday cup shown in Figure 4.8a. The measurements were taken within three days. This is the reason why the pressure is not constant for a capillary length of 50 mm; the pressure decreased over the night. The solution in the syringe was: isopropanol + H2O (1:1) + 1% HCOOH. The gap from the capillary to the Faraday cup was about 13 mm. The transport capillary was set on ground for all the measurements.

It should be noted that the results displayed in Table 4.2 give only the general trends of the setup. The aim was to test the electrospray ionization part of the source and to set some limits on it. A longer capillary (300 mm) was also tested but most of the ions were lost within it, reducing the current observed on the Faraday cup to nearly zero.

$L_{Capillary}$ *(mm)*	P *(mbar)*	$Gap_{needle-capillary}$ *(mm)*	V_{needle} *(V)*	$Q_{syringe}$ *(ml/min)*	I_{FC} *(pA)*
50	4.7	~ 5	2500	0.01	890
				0.05	800
			3000	0.01	1000
				0.05	1100
	4.4	~ 15	2500	0.01	280
				0.05	350
			3000	0.01	370
				0.05	270
100	4	~ 5	2500	0.01	750
				0.05	800
			3000	0.01	700
				0.05	700
		~ 13	2500	0.01	260
				0.05	250
			3000	0.01	350
				0.05	300
150	3.4	~ 5	2500	0.01	300
				0.05	500
			3000	0.01	370
				0.05	500
		~ 15	2500	0.01	200
				0.05	180
			3000	0.01	240
				0.05	280

Table 4.2 – Ion beam intensity for different parameters, i.e. the capillary length, the pressure, the distance between the needle and the capillary, the voltage on the needle and the flow rate on the syringe.

From Table 4.2 one can see that, for each transport capillary, the ion current measured on the Faraday cup is higher when the gap between the needle and the transport capillary is shorter. The voltage applied on the needle and the flow rate do not have a strong influence on the ion current.

4.3.1.3 Evaporation process in the transport capillary

The previously observed trends allowed to choose different ESI configurations propagating different molecular flows. A similar study was then attempted for the rf-carpet transmission with the second Faraday cup, Figure 4.8b, placed a few millimeters behind the rf-carpet. Nevertheless, whatever the high voltage on the needle, the gap from the needle to the capillary, the capillary geometry or the voltages set on the carpet, the ion signal remained at a few tens of pA (maximum 20 pA), and could not be significantly increased, probably because of a too broad mass range production (as a reminder, the solution in the syringe was chosen because it can lead to a molecular ion production of many masses). Before the QMS there is no way to control the production of the different masses. As mentioned in section 4.2.1 the ions are transmitted through the capillary only by the gas flow. During this transport the evaporation process is still ongoing. If the time spent by the ions in the transport capillary is too short, the gas-phase might not be fully reached, inducing production of larger molecules. These molecules are too heavy to be sensitive to the rf settings, and they are not rejected by the rf-carpet. Furthermore, if the alignment of the transport capillary and the carpet is correctly made they can be transported through the carpet by the gas flow. All kinds of molecules can thus be detected with the Faraday cup behind.

The temperature helps to reduce the size of molecules via evaporation. The transport capillary was thus warmed up. An observation of an ion current increase would mean that the heavy molecules broke up while the temperature has raised. To warm up the transport capillary, a tungsten filament was used. Visible in Figure 4.11, the outside part of the capillary was wrapped with a Teflon tape and a tungsten wire (the Teflon is used as an electric insulator between the wire and the capillary). A current was applied on the tungsten wire which led to an increase of the temperature on the capillary (Ohm law). In order to make the test easier, a long transport capillary was used. It gave more space on the capillary to do the wrapping.

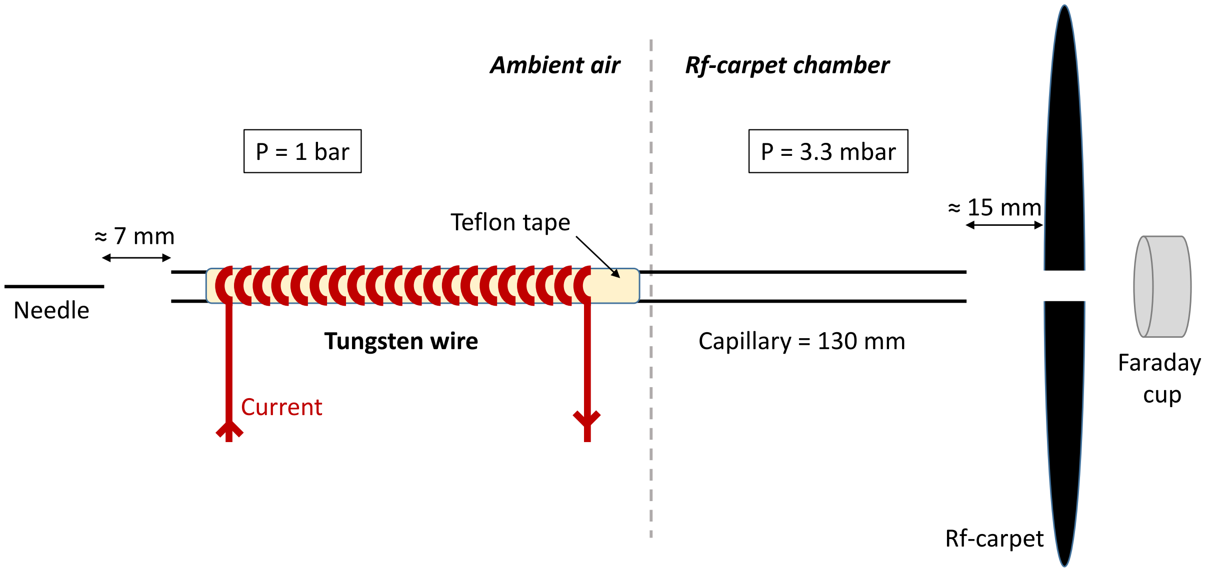

Figure 4.11 – Scheme of the transport capillary. The outside part is wrapped with a Teflon tape and a tungsten wire. A current was applied on the tungsten wire which warmed the transport capillary.

A maximum of 172°C was reached before the wire broke, see Figure 4.12. The increase of the temperature has an effect on the transmission up to ≈ 70°C. Thereafter the transmission remains stable up to ≈ 100°C. For higher temperature, the error bars become too important and one cannot conclude on the trend. The production of heavy molecular ions has thus been highlighted, and a heating of more than 70°C is no longer helping to increase the ion current. This test was performed with a transport capillary length of 130 mm, one can thus expect higher yields of heavy molecules for a shorter capillary. In the following, it was decided to remain with capillaries of about the same length, in this case 150 mm length. With this configuration, one can limit the production of large molecules while not being limited by the molecular ions losses inside a too long capillary. The transport capillary was not warmed up anymore in the following work in order to study, without constraints, the mass range of produced molecular ions by using the QMS and the MCP detector.

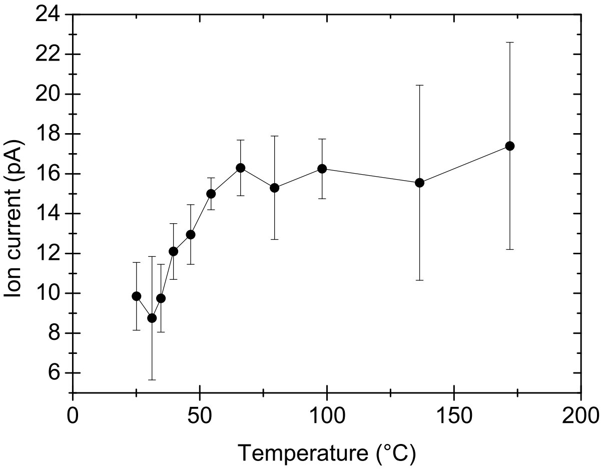

Figure 4.12 – Evolution of the ion current as a function of the temperature applied on the transport capillary.

4.3.1.4 Ion source stability

A typical ion beam intensity measured with a Faraday cup after the transport capillary is shown in Figure 4.13. The measurement performed over one hour gave a beam intensity of $I \approx 700(50)$ pA. Nevertheless, one has to take into account the huge sparks appearing randomly which can have an amplitude as high as 2 nA. These sparks might be due to the needle condition, e.g. accumulation of ions at the tip, air purity conditions, etc.

The beam intensity can also suddenly vary by a few tens of pA. One possible reason would be that the transport capillaries and/or the needle are obstructed by dust, or freed of the dust, resulting in a decrease, or an increase of the ion beam intensity, respectively. A steady cleaning with isopropanol and a regular change of the needle and capillary, would avoid such variations of the beam intensity.

4.3.2 QMS commissioning

4.3.2.1 Definition of the mass scan

In a QMS the ions are propagating along the z-axis while being confined in the x,y direction by an alternative potential V_{rf}, at the angular frequency ω_{rf}, applied on the electrodes. In addition, for mass analysis, a static electric quadrupole potential U_{dc} is also applied on the rods. The force of the field results from an equation of motion of Mathieu's type for an ion inside the QMS, see section 2.3.2. The evolution of an ion in a linear Paul trap such as a QMS, and the ability to perform a mass scan is already discussed in section 2.3. In the following only a brief reminder is given.

The stability of an ion propagating in the QMS is function of the two Mathieu's parameters: a_u (equation (2.18)) and q_u (equation (2.19)), which are related to U_{dc} and V_{rf}, respectively. The solutions for a stable trajectory in the a_u- and q_u-plane are shown in Figure 2.6. The amplitudes of the ac and

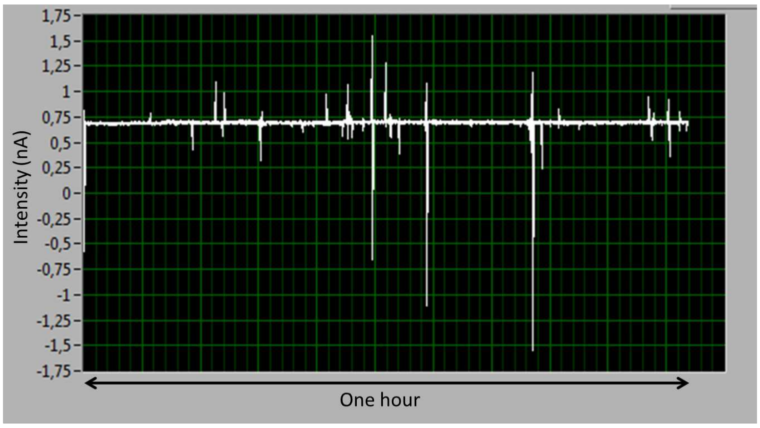

Figure 4.13 – Ion beam intensity measured after the transport capillary for the study of the stability. The measurement was performed over one hour. The intensity is $I \approx 700(50)$ pA. The sparks also visible in the graph are the result of random events around the needle.

dc potentials control the ability of the system to mass-filter the ion beam. A mass scan implies the simultaneous increase of the dc and the rf potentials, and can be represented by the so-called mass scan line shown in Figure 2.6b, and Figure 4.14. The slope of the mass scan line (equation (2.20)) defines the QMS selectivity. As shown in Figure 4.14, a stability region exists for each m/q. Therefore the mass scan line has to be defined in such a way that it is crossing the different stability regions without overlap between them.

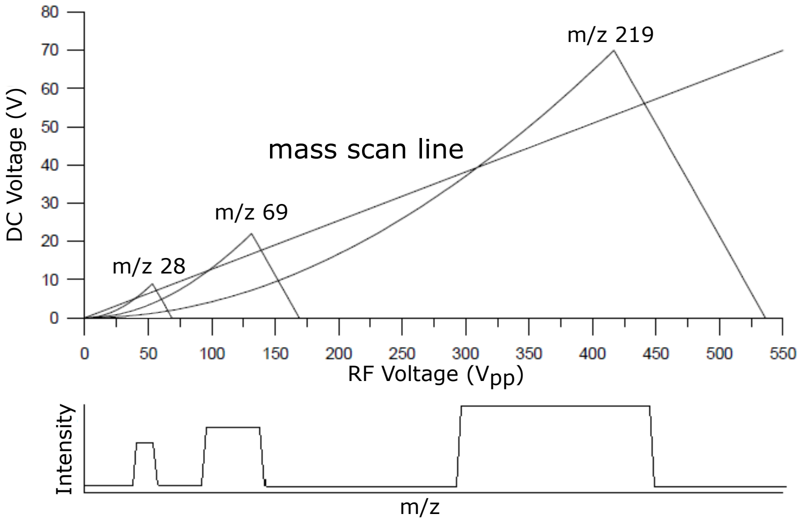

Figure 4.14 – Example of three stability diagrams for three different values of m/q. One can see that the higher the ratio gets, the larger the stability region is. The lower part of the figure represents the beam intensity resulting from the scan line crossing the corresponding stability diagrams [Pedder 2001].

To define the slope, one way is to fix the parameters a_u and q_u so that equation (2.20) becomes a linear equation; U_{dc} as a function of V_{rf}. To have a mass selectivity during the scan, the mass scan line has to cross only the tip of each stability region, see Figure 4.14. The tip of a region (shown in Figure 2.6b) is when a_u and q_u are optimum, 0.237 and 0.706, respectively. The line slope has been calculated as follows: q_u was always fixed to the optimum value: 0.706. a_u was fixed to a value slightly lower to its optimum. When the ratio $a_u/2q_u$ is fixed, the mass scan is actually a scan of the dc amplitude as a function of the ac amplitude, or vice-versa.

However, a linear definition of the mass scan line has some experimental limits in the selectivity of the QMS. As shown in the lower part of Figure 4.14, the signal intensity increases as a function of the mass-to-charge ratio, but the resolution decreases at the same time. Within the framework of this work the mass scan line has been defined as a linear equation, therefore a loss in resolution is expected for higher masses. A better definition of the mass scan line giving a constant resolution [Pedder 2001] could be a very good improvement for the source.

4.3.2.2 Experimental performance of the QMS

As explained in section 4.3.2.1, at the beginning of each mass scan, the ratio $a_u/2q_u$ was fixed to a value (for example 0.297 with $a_u = 0.21$ and $q_u = 0.706$). For a fixed rf frequency the input rf-amplitude (from the waveform generator) was scanned linearly. The rf signal was sent to the rf-amplifier, and to a homemade toroidal coil (creation of the two opposite phases and additional amplification). The applied dc voltage was then $U_{\text{dc}} = V_{\text{rf}} \times a_u/2q_u$. For every scan step, the signal intensity on the phosphor screen was recorded with the CCD camera, a typical example in shown in Figure 4.15. The signal was averaged on fifteen measurements for each scan step. The time lapse between each measurement was set arbitrary but fixed.

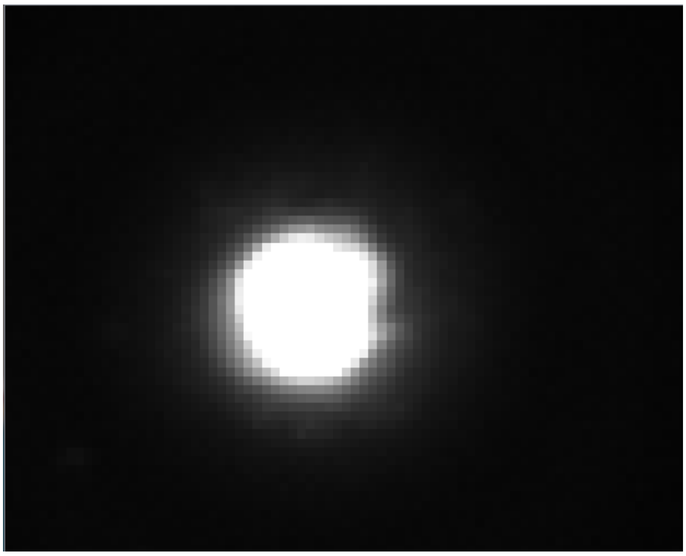

Figure 4.15 – Photo taken with the CCD camera of the ion spot on the phosphor screen. The spot diameter is ≈ 2 mm.

For all the scans presented in the following, some parameters of the ion source are fixed, the rf frequency (f_{carpet}) and amplitude applied on the rf-carpet, the rf-carpet dc-gradient ($V_{gradient}$), the dc applied on the two short RFQs (V_{RFQ}), the voltage applied on the diaphragm ($V_{Diaphragm}$) and on the needle (V_{needle}), and finally the flow applied on the syringe ($Q_{syringe}$). Their respective values are listed below:

- $f_{carpet} = 1.71$ MHz at 50 V_{pp}
- $V_{gradient} = 40.9$ V
- $V_{RFQ} = 0$ V

- $V_{Diaphragm} = -460$ V
- $V_{needle} = 2990$ V
- $Q_{syringe} = 0.04$ mL/min

The rf signals applied on the two short RFQs are equal to the rf signal applied on the QMS.

The two graphs shown in Figure 4.16 are mass scans performed with the QMS for a solution of isopropanol + H2O (1:1) + 1% HCOOH with an rf frequency of $f_{QMS} = 1.667$ MHz. The rf amplitude $V_{rf,QMS}$ and the dc $U_{dc,QMS}$ were varied from 12 $\mathrm{V_{pp}}$ to 700 $\mathrm{V_{pp}}$ and from 0.8 V to 50 V, respectively.

Everything remained the same between the two scans, except the a_u parameter which was equal to 0.20 and 0.21 in Figure 4.16a and Figure 4.16b, respectively. The x-axis represents the calculated m/q ratio. The scan was stopped when the frequency generator was at its maximum amplitude, i.e. 10 $\mathrm{V_{pp}}$, corresponding to 700 $\mathrm{V_{pp}}$ applied on the QMS rods. The y-axis is the number of counts in arbitrary units. Different peaks are visible on the graphs. The mass to charge ratios indicated on the figures are obtained by Gauss fits. They are shown for indicative purposes.

Two main peaks are visible in both graphs, the peaks number 2 and 3 at $m/q = 60$ u/e and 76 u/e, respectively. In Figure 4.16a there is a peak at $m/q = 36$ u/e. However, it has almost disappeared in Figure 4.16b. Since the data were not taken the same day, several effects might have played a role in the disappearance of the peak, such as evaporation or chemical reactions.

As already mentioned earlier, if the value of a_u increases the mass selection increases. The difference in the mass selection is visible between the two graphs. For a higher a_u value (Figure 4.16b) an increase of the signal-to-noise ratio is observed and a slight increase in mass selection for the heavier mass-to-charge ratios. Indeed, a fifth peak has appeared at $m/q = 121$ u/e. In both graphs there is a prominent peak centered at $m/q = 60$ u/e which corresponds to the mass of singly-charged isopropanol (n(C_3H_8O) mass = 60 g/mol). Therefore the probability that it is isopropanol is relevant. However, an isotopic mass resolution was not reached with the QMS, it will be discussed in the following. One cannot thus firmly claim that isopropanol is the only species in this peak.

To reach a resolution which allows to separate isotopes, the mass scan line slope should have been more accurately defined. In Figure 4.17 is represented a zoom on the apex of the theoretical Mathieu's diagram for a mass-to-charge ratio of 58, 59, 60, 61 and 62. One can see that an isotopic mass resolution between the three mass-to-charge values requires a mass scan line defined with $a_u = 0.235$ (q_u being at its optimal value of 0.706). For a lower value of a_u, no isotopic mass resolution can be expected. But unfortunately, no scans were done with this optimum value.

Another mass scan with the same solution was performed with a lower resonance frequency: $f_{QMS} =$ 920 kHz, allowing to observe higher masses in the spectrum. The result is shown in Figure 4.18. The rf amplitude $V_{rf,QMS}$ and the dc $U_{dc,QMS}$ were varied from 8 $\mathrm{V_{pp}}$ to 300 $\mathrm{V_{pp}}$ and 0.6 V to 21 V, respectively. The a_u parameter was set to 0.2. The same peaks around $m/q \approx 62, 79, 96$ u/e are visible. Similarly to Figure 4.16, the mass resolution is not at the isotopic level, there is still a probability that the peak centered at 62 u/e contains isopropanol. One can see the huge increase of the signal above $m/q =$ 150 u/e. According to Figure 4.14 one expects an intensity increase in the higher mass range, however the increase is very strong compared to the expectations. As the maximum input amplitude was reached by the frequency generator, the scan was stopped. One cannot conclude on whether it is a peak at ≈ 200 u/e or a sudden increase of the noise level.

Another series of mass scans for different values of a_u were performed for a solution of isopropanol + tap water (1:1) + 1% HCOOH. The advantage of changing the sample from deionized water to tap water is that the tap water contains many more chemical elements, which are thus included in the solution. Therefore, the probability to form various sorts of molecular ions with the ESI process increases. The mass range of produced molecular ions becomes larger. The results are shown in Figure 4.19. The scans

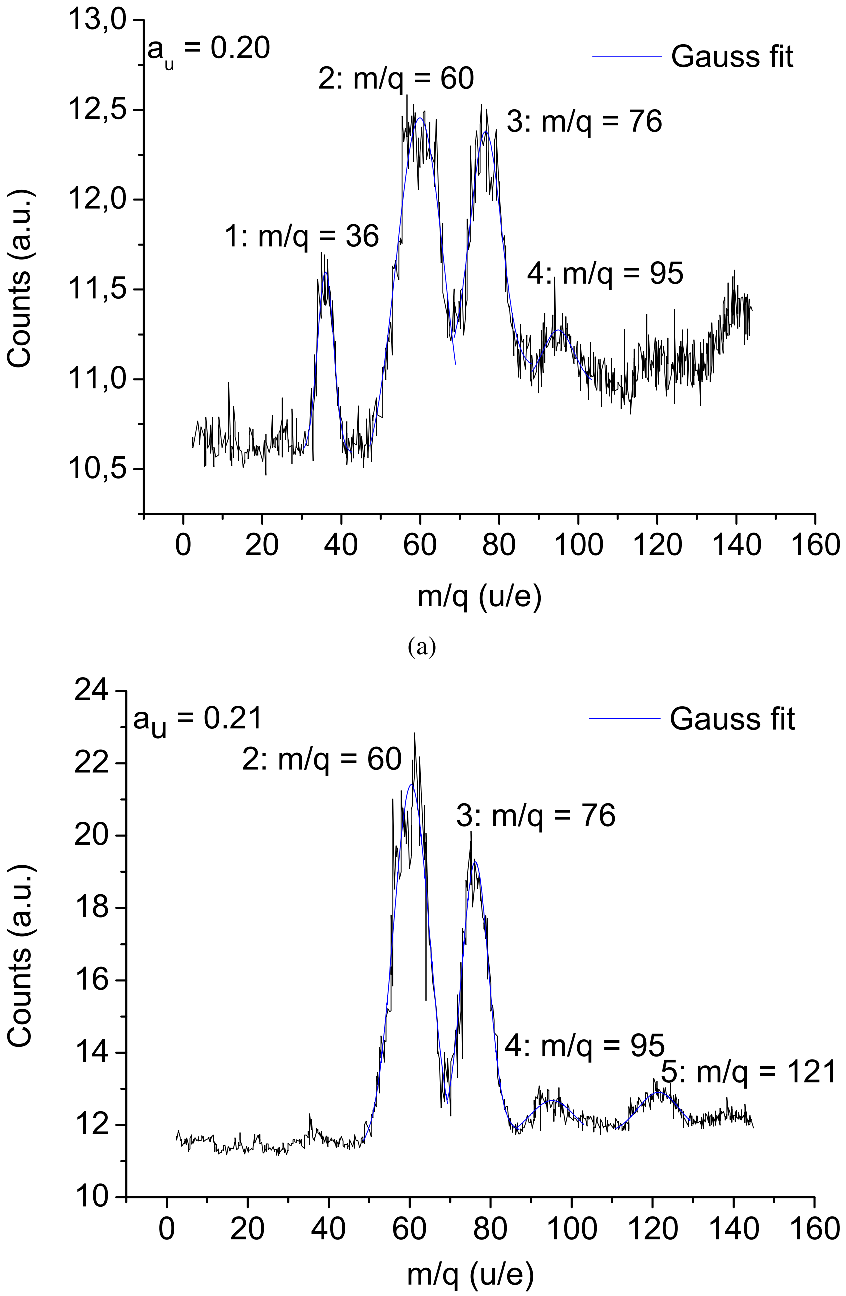

(a)

(b)

Figure 4.16 – Mass scan of the solution: isopropanol + H2O (1:1) + 1% HCOOH with a QMS frequency of $f_{QMS} = 1.667$ MHz. In Figure (a) and Figure (b) the a_u parameter was set to be 0.20 and 0.21, respectively.

were performed with an rf frequency of $f_{QMS} = 890$ kHz. The rf amplitude $V_{rf,QMS}$ and the dc $U_{dc,QMS}$ were varied from 8 V_{pp} to 355 V_{pp} and 0.6 V to 26 V, respectively.

The four scans were done one after the other. This helps to reduce the systematic errors and allows a more trustable comparison between the results. The signal dropped back to the noise level (in Figure 4.19d) as the syringe was emptied.

Two main peaks are visible on each graph, one at $m/q \approx 80$ u/e, one at $m/q \approx 220$ u/e. One can see that with the increase of the resolution (increase of a_u) the centroid of the first peak is shifting to

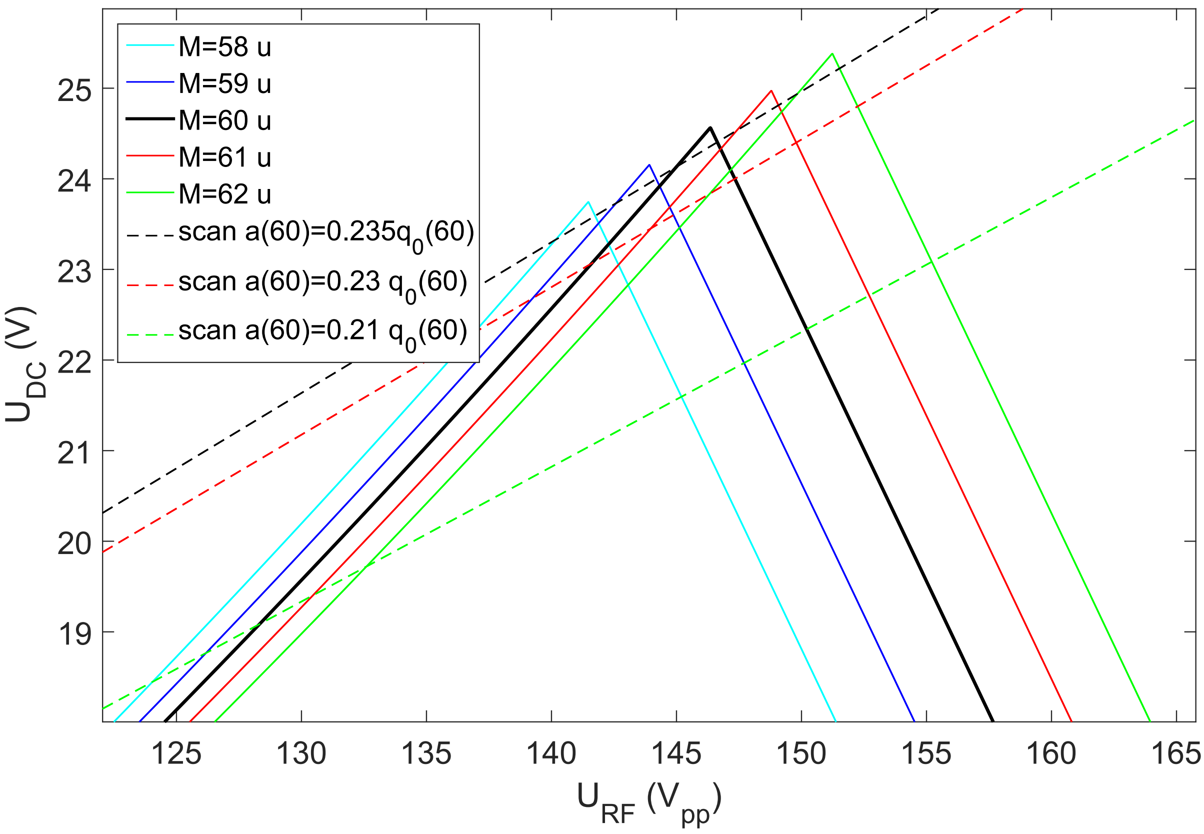

Figure 4.17 – Theoretical representation of the Mathieu's diagram for a mass over charge ratio centered on $m/q = 60 \pm 2\,\mathrm{u/e}$. Three mass scan lines are represented, each having a different value of the Mathieu's parameter a_u.

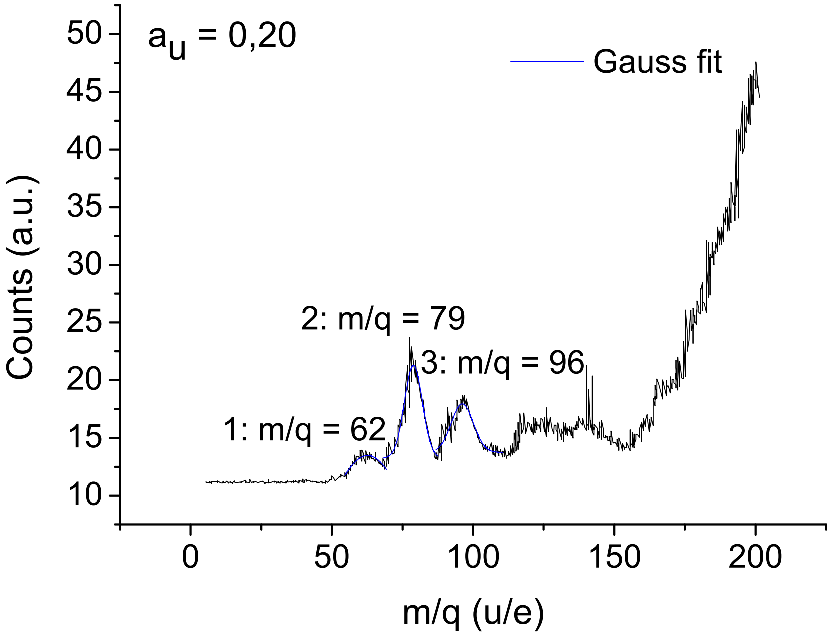

Figure 4.18 – Mass scan of the solution: isopropanol + H2O (1:1) + 1% HCOOH with: $f_{QMS} = 920\,\mathrm{kHz}$. The a_u parameter was set to be 0.2.

higher values of m/q, from $m/q = 79$ u/e for $a_u = 0.20$ to $m/q = 83$ u/e for $a_u = 0.23$. As explained in section 4.3.2.1, for a lower value of a_u, the slope of the scan line is reduced, which induces wider mass peaks and due to the tail on the left side of the stability diagram, the center of the mass peaks are shifting to the lower apparent masses [Pedder 2001]. This effect is also observable for the second peak, but less significantly because of the non-complete fourth scan.

One can estimate the QMS resolving power in Figure 4.19d with the peak centered at $m/q = 83$ u/e, $R = m/\Delta m \approx 47$. This peak could be an acetonitril (CH_3CN) signature (the molecular ion is formed via the association of two acetonitril molecules plus one hydrogen atom), however, as no clear molecular identifications are performed, one cannot conclude on whether the peak in constituted by only acetonitril, or if there are other molecules constituting this peak. In other words, with this resolution, one cannot be sure if in this peak are present only counts for $m/q = 83$ u/e, or if there are counts corresponding to $m/q = 83 \pm 1$ u/e. In this context, the resolution given here can be considered only as a lower limit of the QMS resolving power.

One can notice that the isopropanol peak ($m/q = 60$ u/e) present in Figure 4.16 is much less important in Figure 4.18 and even not visible anymore in Figure 4.19. This effect can be explained by the QMS frequency, which was decreased from 1.667 MHz to 890 kHz and thus led to an optimization on the higher mass transmission of the QMS. It is thus possible that the isopropanol is not properly transmitted anymore by the QMS.

4.4 Conclusion and outlook

An electrospray ion source has been developed at the Max-Planck-Institut für Kernphysik in Heidelberg, Germany. The purpose of this source is to deliver a large range of isobaric masses for calibration purposes. It is based on the one developed at RIKEN.

The impact of the transport capillary lengths on the produced beam was studied and a compromise was found between a length allowing a good transmission and an evaporation time long enough to produce light molecules. The heating of the transport capillary seemed to be an effective improvement to work with light molecules as intended, however a permanent fixation system would have to be installed to gain in reliability. This could be done in the future.

A signal was observed behind the carpet (a few tens of pA) and the ions were transported through the QMS. Out of the first mass scans presented a peak at $m/q = 60$ u/e could be identified. This peak can be associated to isopropanol (the solvent of the solution), however, the resolution of the QMS was too low for an isotopic mass identification and no one could confirm that the isopropanol was the only species in this peak. There are different explanations for the low resolution. One is that the mass scan line was defined with a too small a_u parameter (0.2 or 0.21). It was shown that, theoretically, a mass resolution which allows an isotopic mass separation can be achieved with a mass scan line defined with $a_u = 0.235$ (with the q_u parameter fixed at 0.706).

In case an isotopic mass resolution can be achieved, a way to characterize the QMS with a known mass would be to use the peak at $m/q = 60$ u/e. Indeed, one could verify if this peak really corresponds to the isopropanol by using the natural isotopic abundance of ^{13}C, which is $\approx 1\%$. The chemical formula of isopropanol is C_3H_8O, therefore, the probability to have one atom of ^{13}C among the three constituting on molecule of isopropanol is $\approx 3\%$. The natural isotopic abundance of $^{17,18}O$ and ^2H are not considered here as they are too low. Therefore, with a mass scan line properly defined ($a_u = 0.235$ and $q_u = 0.706$), it should be possible to distinguish a second less abundant peak at $m/q = 61$ u/e and thus confirm the presence of isopropanol, and use it to characterize the QMS. However, in all the results presented here, the signal to noise ratio s/r is too low and the isopropanol peak with ^{13}C would not be visible ($s/r = 1.8$ in Figure 4.16b).

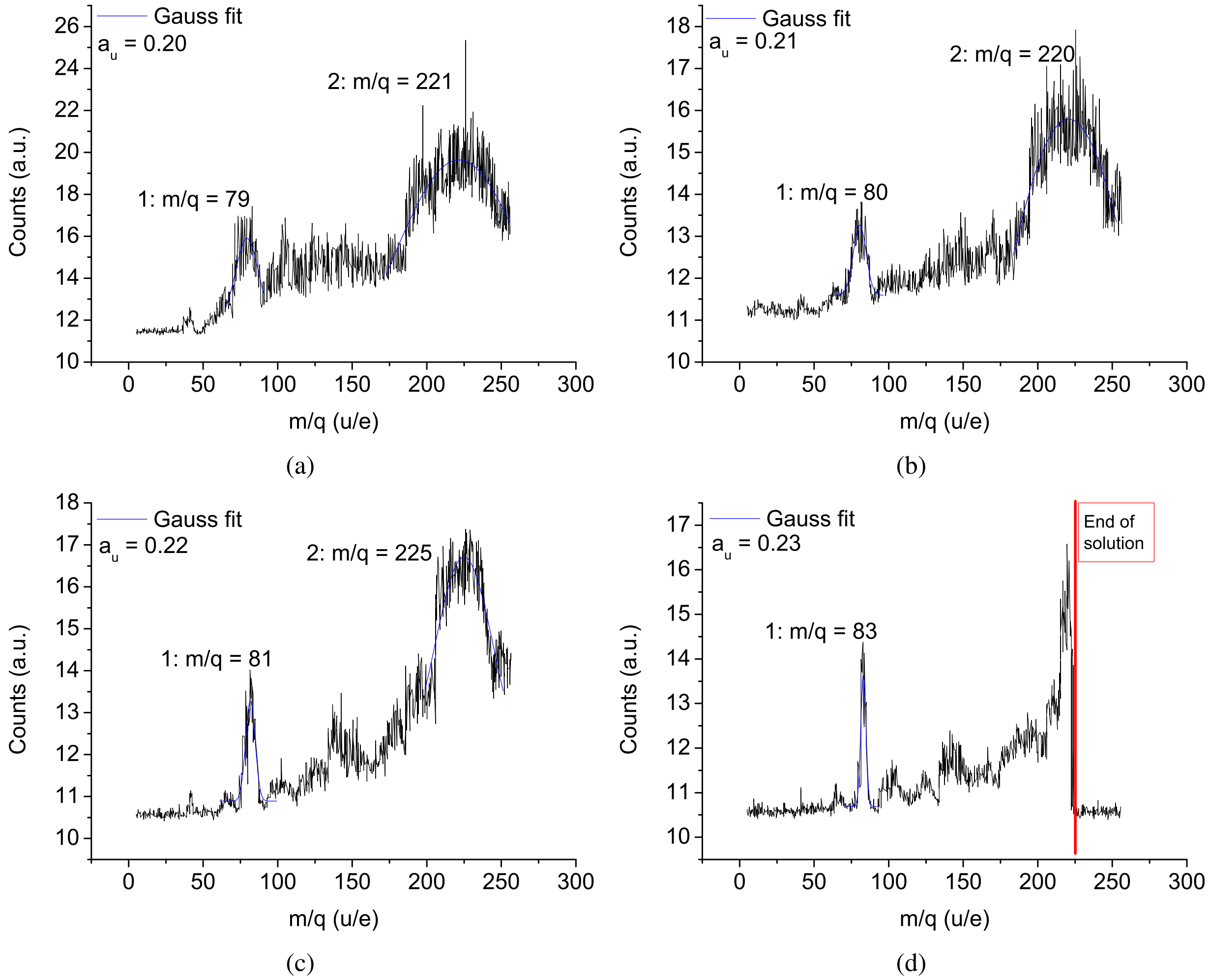

(a) (b) (c) (d)

Figure 4.19 – Series of mass scans for different values of the a_u parameter. $a_u = 0.20, 0.21, 0.22, 0.23$ for (a), (b), (c) and (d), respectively. The sample of the solution was changed from de-ionized water to tap water while keeping the same proportion; isopropanol + tap water (1:1) + 1% HCOOH with: $f_{QMS} = 890\,\mathrm{kHz}$.

As no clear mass identification could be performed with the two solutions used in this work (isopropanol + H2O (1:1) + 1% HCOOH, or isopropanol + tap water (1:1) + 1% HCOOH), other scans were started with a specific solution made of 0, 1% PXE in cyclohexane. The m/q ratios of the PXE molecule fragments are: $165, 180, 195, 210\,\mathrm{u/e}$. The idea was to use these peaks to characterize the QMS, and determine its resolution. However, no significant signal was observed on the MCP detector. A signal on the phosphor screen was observed only in the transmission mode. Apart from problems with applying the dc and rf amplitudes, one explanation could be that the motor driving the syringe was too slow. Indeed, if the motor is too slow, not enough solution is present at the tip of the needle and less droplets are formed, therefore not enough molecules created at the same time. The ESI part of the source will have to be tuned with this new solution to create and detect enough molecules of interest.

The noise reduction is an important part of further developments of the source. The signal was recorded with a CCD camera, but the insulation from the day-light was not optimum. A better insulation would result into a major decrease of the noise level. Another improvement for the source would be to decrease the pressure level in the QMS chamber. This could lead to a better resolution with the QMS. Finally, in this setup, the electrospray process is occurring in ambient air. An electrospray ionization in an insulated chamber, filled with nitrogen at atmospheric pressure, would help to control the ionization and to reduce the ionization of unwanted species, such as elements present in ambient air.

The ESI ion source is still at its early stage of commissioning. However, the results are promising, and many solutions can be investigated to better characterize the ion source, and thus being able to provide reference ions to an MR-TOF MS.

CHAPTER 5

Conclusion

On the physics side of this work, the masses of neutron-rich strontium and rubidium isotopes produced ($^{100-102}$Sr and $^{100-102}$Rb) at the ISOLDE facility [Kugler 2000] at CERN were measured with the ISOLTRAP mass spectrometer [Mukherjee 2008]. The mass measurements were performed with the precision Penning trap for the strontium isotopes, and the MR-TOF MS for the rubidium isotopes. The ^{102}Sr and ^{101,102}Rb masses were measured for the first time.

The new mass measurements reported in this work confirm the trend in the region of deformation well beyond $N = 60$, approaching the nuclear mid-shell. Indeed, in the strontium and rubidium isotopic chains the deformation continues at least as far as $N = 65$ without major structural changes. The identification of the level scheme in ^{102}Sr recently discussed in [Wang 2016] also supports this conclusion.

The experimental nuclear masses and charge radii values available in this region of deformation were compared to different mean-field approaches (including beyond mean-field). Two nucleon-nucleon interactions were used in these calculations, the Skyrme one with the UNEDF0 and UNEDF1 parametrization, see [Kortelainen 2010, Kortelainen 2012], respectively, and the Gogny one with the D1S parametrization [Dechargé 1980, Berger 1991]. The beyond mean-field calculations used the Gogny D1S interaction in a five-dimensional collective Hamiltonian (5DCH) [Clément 2016]. The success of the UNEDF0 parametrization (optimized on spherical and deformed nuclei) in reproducing the nuclear deformation was confirmed. However, the UNEDF1 parametrization, which differs from UNEDF0 by its optimization on the excitation energies of fission isomers, showed a less good reproduction of the nuclear deformation in the region of interest. The calculations with the Gogny interaction gave a less good agreement with the experimental data. Furthermore, the introduction of the beyond mean-field D1S+5DCH did not help reproducing the data.

The state-of-the-art HFB calculations with a Skyrme or a Gogny effective interaction allowed to discuss the overall trend of the ground-state properties along the isotopic chain of interest. However, the odd nuclei were not computed, which limits the possibility of completely quantifying the strength of the increase in the two-neutron separation energies and in the mean-square charge radii across $N = 60$. A Skyrme-Hartree-Fock-Bogoliubov study of the binding energies and charge radii was thus performed for the odd-N krypton and strontium isotopes. The time-reversal and symmetry-unconstrained HFODD code [Schunck 2012, Dobaczewski 2009a] with the SLy4 parametrization [Chabanat 1998] of the Skyrme interaction and contact volume-pairing force were used. The calculations of odd-nuclei were performed with a full quasi-particle blocking [Dobaczewski 2009b]. Out of these, the prolate and oblate solutions gave a good agreement with the experimental strontium and krypton data, respectively. These calculations excluded the krypton chain from the region of strong deformation. However, a transition between weakly and strongly deformed shapes is still predicted to occur in the ^{97,98}Kr isotopes.

The region of deformation $A \approx 100$ is a hot topic since many years. The recent results published in [Sotty 2015, Rodríguez 2014, Clément 2016, Wang 2016], including the one presented in this work, are confirming the continuity of the nuclear ground state deformation beyond $N = 60$. The high Z border of the region of deformation is known as being the molybdenum isotopic chain. However, the lower limit is not known. The results from [Naimi 2010b, Sotty 2015] point out the ^{97}Rb nuclide as being the lightest deformed $N = 60$ isotone. Nevertheless, the results published by [Rodríguez 2014] predict a shape coexistence to occur in ^{98}Kr. An experimental proof of nuclear deformation in ^{97}Rb or ^{98}Kr is thus the next step in order to highlight the "southwest" border of the deformation. This information will allow to better constrain models dedicated to nuclear deformation. It can also be of a great help in the framework of the *r*-process modeling.

On the technical side of this work, an electrospray ion source able to deliver a large range of isobaric masses for calibration purposes has been developed. Two different solutions (isopropanol + H2O (1:1) + 1% HCOOH and isopropanol + tap water (1:1) + 1% HCOOH) were electrosprayed. The created molecular ions were transported via an rf-carpet to a QMS for mass separation. The detection was performed with an MCP connected to a phosphor screen and a CCD camera.

The possibility to perform mass scans with the QMS has been implemented and first studies on the QMS resolution could be attempted. The highest resolution achieved with the QMS was $m/\Delta m \approx 47$. As such a resolution does not allow to identify isotopes, it can only be considered as a lower limit of the QMS resolving power. Also related to the achieved QMS resolution, no characterization of the QMS could be performed, as no molecular ion species could be clearly identified. However, the probability that isopropanol and acetonitril were observed is relevant. It was also shown that several improvements can be implemented to the source in order to improve the mass resolution. Indeed, the level of noise on the camera was very high and a better insulation from the ambient light would significantly improve the sensitivity of the ion source. The pressure in the QMS chamber is also a parameter which can be optimized. By increasing the pump speed and by working on the transport capillary geometries, one could lower the pressure, and thus reach a better resolution with the QMS. Finally, one could also improve the mass scan line definition. It was shown that the more precisely this line is defined, the better the resolution is. The mass scan line can also be modified by changing its shape from linear to exponential like shape, which would also increase the resolution.

The ion source presented in this work is still in its early stage of commissioning, however, a broad ion mass range production was observed behind the QMS, and an improvement of the QMS resolution would lead to the isobaric mass production needed to provide reference ions to an MR-TOF MS, for example.

Bibliography

[Anderson 1962] P. W. Anderson. *Theory of Flux Creep in Hard Superconductors*. Phys. Rev. Lett., vol. 9, pages 309–311, 1962.

[Angeli 2013] I. Angeli and K.P. Marinova. *Table of experimental nuclear ground state charge radii: An update*. Atomic Data and Nuclear Data Tables, vol. 99, no. 1, pages 69 – 95, 2013.

[Audi 2012] G. Audi, F.G. Kondev, M. Wang, B. Pfeiffer, X. Sun, J. Blachot and M. MacCormick. *The Nubase2012 evaluation of nuclear properties*. Chinese Physics C, vol. 36, no. 12, page 1157, 2012.

[Balog 1992] K. Balog, M. Graefenstedt, M. Groß, P. Jürgens, U. Keyser, F. Münnich, T. Otto, F. Schreiber, T. Winkelmann and J. Wulff. *Experimental beta-decay energies of very neutron-rich isobars with mass numbers A=101 and A=102*. Zeitschrift für Physik A Hadrons and Nuclei, vol. 342, no. 2, pages 125–132, 1992.

[Bardeen 1957] J. Bardeen, L. N. Cooper and J. R. Schrieffer. *Theory of Superconductivity*. Phys. Rev., vol. 108, pages 1175–1204, 1957.

[Bender 2003] M. Bender, P.-H. Heenen and P.-G. Reinhard. *Self-consistent mean-field models for nuclear structure*. Rev. Mod. Phys., vol. 75, pages 121–180, 2003.

[Bender 2006] M. Bender, G. F. Bertsch and P.-H. Heenen. *Global study of quadrupole correlation effects*. Phys. Rev. C, vol. 73, page 034322, 2006.

[Berger 1991] J.F. Berger, M. Girod and D. Gogny. *Time-dependent quantum collective dynamics applied to nuclear fission*. Computer Physics Communications, vol. 63, no. 1, pages 365 – 374, 1991.

[Bertsch 2007] G. F. Bertsch, M. Girod, S. Hilaire, J.-P. Delaroche, H. Goutte and S. Péru. *Systematics of the First* 2^+ *Excitation with the Gogny Interaction*. Phys. Rev. Lett., vol. 99, page 032502, 2007.

[Bethe 1936] H. A. Bethe and R. F. Bacher. *Nuclear Physics A. Stationary States of Nuclei*. Rev. Mod. Phys., vol. 8, pages 82–229, 1936.

[Blaum 2006] K. Blaum. *High-accuracy mass spectrometry with stored ions*. Physics Reports, vol. 425, no. 1, pages 1 – 78, 2006.

[Blaum 2013] K. Blaum, J. Dilling and W. Nörtershäuser. *Precision atomic physics techniques for nuclear physics with radioactive beams*. Physica Scripta, vol. 2013, no. T152, page 014017, 2013.

[Bohr 1951] A. Bohr. *On the Quantization of Angular Momenta in Heavy Nuclei*. Phys. Rev., vol. 81, pages 134–138, 1951.

[Bollen 1990] G. Bollen, R. B. Moore, G. Savard and H. Stolzenberg. *The accuracy of heavy-ion mass measurements using time of flight-ion cyclotron resonance in a Penning trap*. Journal of Applied Physics, vol. 68, no. 9, 1990.

[Bollen 1992] G. Bollen, H.-J. Kluge, M. König, T. Otto, G. Savard, H. Stolzenberg, R. B. Moore, G. Rouleau, G. Audi and ISOLDE Collaboration. *Resolution of nuclear ground and isomeric states by a Penning trap mass spectrometer*. Phys. Rev. C, vol. 46, pages R2140–R2143, 1992.

[Bollen 2001] G. Bollen. *Radioactive Nuclear Beams Mass measurements of short-lived nuclides with ion traps*. Nuclear Physics A, vol. 693, no. 1, pages 3 – 18, 2001.

[Bollen 2004] G. Bollen. Traps for rare isotopes, pages 169–210. Springer Berlin Heidelberg, Berlin, Heidelberg, 2004.

[Brown 1982] L. S. Brown and G. Gabrielse. *Precision spectroscopy of a charged particle in an imperfect Penning trap*. Phys. Rev. A, vol. 25, pages 2423–2425, 1982.

[Buchinger 1990] F. Buchinger, E. B. Ramsay, E. Arnold, W. Neu, R. Neugart, K. Wendt, R. E. Silverans, P. Lievens, L. Vermeeren, D. Berdichevsky, R. Fleming, D. W. L. Sprung and G. Ulm. *Systematics of nuclear ground state properties in* $^{78\text{˘}100}\mathrm{Sr}$ *by laser spectroscopy*. Phys. Rev. C, vol. 41, pages 2883–2897, 1990.

[Cameron 1948] A. E. Cameron and D. F. Eggers. *An Ion "Velocitron"*. Review of Scientific Instruments, vol. 19, no. 9, 1948.

[Campbell 2002] P. Campbell, H. L. Thayer, J. Billowes, P. Dendooven, K. T. Flanagan, D. H. Forest, J. A. R. Griffith, J. Huikari, A. Jokinen, R. Moore, A. Nieminen, G. Tungate, S. Zemlyanoi and J. Äystö. *Laser Spectroscopy of Cooled Zirconium Fission Fragments*. Phys. Rev. Lett., vol. 89, page 082501, 2002.

[Chabanat 1998] E. Chabanat, P. Bonche, P. Haensel, J. Meyer and R. Schaeffer. *A Skyrme parametrization from subnuclear to neutron star densities Part II. Nuclei far from stabilities*. Nuclear Physics A, vol. 635, no. 1, pages 231 – 256, 1998.

[Chadwick 1932] James Chadwick. *Possible existence of a neutron*. Nature, vol. 129, no. 3252, page 312, 1932.

[Cheal 2007] B. Cheal, M.D. Gardner, M. Avgoulea, J. Billowes, M.L. Bissell, P. Campbell, T. Eronen, K.T. Flanagan, D.H. Forest, J. Huikari, A. Jokinen, B.A. Marsh, I.D. Moore, A. Nieminen, H. Penttilä, S. Rinta-Antila, B. Tordoff, G. Tungate and J. Äystö. *The shape transition in the neutron-rich yttrium isotopes and isomers*. Physics Letters B, vol. 645, no. 2–3, pages 133 – 137, 2007.

[Cheifetz 1970] E. Cheifetz, R. C. Jared, S. G. Thompson and J. B. Wilhelmy. *Experimental Information Concerning Deformation of Neutron Rich Nuclei in the* $A \sim 100$ *Region*. Phys. Rev. Lett., vol. 25, pages 38–43, 1970.

[Clegg 1971] G. A. Clegg and M. Dole. *Molecular beams of macroions. III. Zein and polyvinylpyrrolidone*. Biopolymers, vol. 10, no. 5, pages 821–826, 1971.

[Clément 2006] E. Clément. *Shape coexistence in neutron-deficient Krypton and Selenium isotopes studied by low-energy Coulomb excitation of radioactive ion beams*. Theses, Université Paris Sud - Paris XI, 2006.

[Clément 2016] E. Clément, M. Zielińska, A. Görgen, W. Korten, S. Péru, J. Libert, H. Goutte, S. Hilaire, B. Bastin, C. Bauer, A. Blazhev, N. Bree, B. Bruyneel, P. A. Butler, J. Butterworth, P. Delahaye, A. Dijon, D. T. Doherty, A. Ekström, C. Fitzpatrick, C. Fransen, G. Georgiev, R. Gernhäuser, H. Hess, J. Iwanicki, D. G. Jenkins, A. C. Larsen, J. Ljungvall, R. Lutter, P. Marley, K. Moschner, P. J. Napiorkowski, J. Pakarinen, A. Petts, P. Reiter, T. Renstrøm, M. Seidlitz, B. Siebeck, S. Siem, C. Sotty, J. Srebrny, I. Stefanescu, G. M. Tveten, J. Van de Walle, M. Vermeulen, D. Voulot, N. Warr, F. Wenander, A. Wiens, H. De Witte and K. Wrzosek-Lipska.

Spectroscopic Quadrupole Moments in ^{96,98}Sr*: Evidence for Shape Coexistence in Neutron-Rich Strontium Isotopes at* $N = 60$. Phys. Rev. Lett., vol. 116, page 022701, 2016.

[Comisarow 1974] M. B. Comisarow and A. G. Marshall. *Fourier transform ion cyclotron resonance spectroscopy*. Chemical Physics Letters, vol. 25, no. 2, pages 282 – 283, 1974.

[Cwiok 1987] S. Cwiok, J. Dudek, W. Nazarewicz, J. Skalski and T. Werner. *Single-particle energies, wave functions, quadrupole moments and g-factors in an axially deformed woods-saxon potential with applications to the two-centre-type nuclear problems*. Computer Physics Communications, vol. 46, no. 3, pages 379 – 399, 1987.

[Cwiok 2005] S. Cwiok, P.-H. Heenen and W. Nazarewicz. *Shape coexistence and triaxiality in the superheavy nuclei*. vol. 433, no. 7027, pages 705–709, 2005.

[D. Manura 2008] D. Dahl D. Manura. *SIMION (R) 8.0 User Manual (Scientific Instrument Services, Inc. Ringoes, NJ 08551)*, 2008.

[De La Mora 1994] J. F. De La Mora and I. G. Loscertales. *The current emitted by highly conducting Taylor cones*. Journal of Fluid Mechanics, vol. 260, pages 155–184, 1994.

[Dechargé 1980] J. Dechargé and D. Gogny. *Hartree-Fock-Bogolyubov calculations with the* $D1$ *effective interaction on spherical nuclei*. Phys. Rev. C, vol. 21, pages 1568–1593, 1980.

[Dehmelt 1976] H. G. Dehmelt. Atomic masses and fundamental constants, chapter A Progress Report on the g-2 Resonance Experiments, pages 499–505. Springer US, Boston, MA, 1976.

[Dehmelt 1990] H. G. Dehmelt. *Experiments with an isolated subatomic particle at rest*. Rev. Mod. Phys., vol. 62, pages 525–530, 1990.

[Dobaczewski 2001] J. Dobaczewski, W. Nazarewicz and P.-G. Reinhard. *Pairing interaction and self-consistent densities in neutron-rich nuclei*. Nuclear Physics A, vol. 693, no. 1, pages 361 – 373, 2001.

[Dobaczewski 2009a] J. Dobaczewski, B.G. Carlsson, J. Dudek, J. Engel, P. Olbratowski, P. Powałowski, M. Sadziak, J. Sarich, W. Satuła, N. Schunck*et al.* *HFODD (v2. 40h) User's Guide*. arXiv preprint arXiv:0909.3626, 2009.

[Dobaczewski 2009b] J. Dobaczewski, W. Satuła, B.G. Carlsson, J. Engel, P. Olbratowski, P. Powałowski, M. Sadziak, J. Sarich, N. Schunck, A. Staszczak, M. Stoitsov, M. Zalewski and H. Zduńczuk. *Solution of the Skyrme–Hartree–Fock–Bogolyubov equations in the Cartesian deformed harmonic-oscillator basis.: (VI) hfodd (v2.40h): A new version of the program*. Computer Physics Communications, vol. 180, no. 11, pages 2361 – 2391, 2009.

[Dole 1968] M. Dole, L. L. Mack, R. L. Hines, R. C. Mobley, L. D. Ferguson and M. B. Alice. *Molecular Beams of Macroions*. The Journal of Chemical Physics, vol. 49, no. 5, 1968.

[Duguet 2001] T. Duguet, P. Bonche, P.-H. Heenen and J. Meyer. *Pairing correlations. I. Description of odd nuclei in mean-field theories*. Phys. Rev. C, vol. 65, page 014310, 2001.

[Ebert 2012] J. Ebert, R. A Meyer and K. Sistemich. Nuclear structure of the zirconium region: Proceedings of the international workshop. Springer Science & Business Media, 2012.

[Einstein 1905] A. Einstein. *Ist die Trägheit eines Körpers von seinem Energieinhalt abhängig?* Annalen der Physik, vol. 323, no. 13, pages 639–641, 1905.

[Eliseev 2011] S. Eliseev, C. Roux, K. Blaum, M. Block, C. Droese, F. Herfurth, M. Kretzschmar, M. I. Krivoruchenko, E. Minaya Ramirez, Yu. N. Novikov, L. Schweikhard, V. M. Shabaev, F. Šimkovic, I. I. Tupitsyn, K. Zuber and N. A. Zubova. *Octupolar-Excitation Penning-Trap Mass Spectrometry for Q-Value Measurement of Double-Electron Capture in* ^{164}Er. Phys. Rev. Lett., vol. 107, page 152501, 2011.

[Eliseev 2013] S. Eliseev, K. Blaum, M. Block, C. Droese, M. Goncharov, E. Minaya Ramirez, D. A. Nesterenko, Yu. N. Novikov and L. Schweikhard. *Phase-Imaging Ion-Cyclotron-Resonance Measurements for Short-Lived Nuclides*. Phys. Rev. Lett., vol. 110, page 082501, 2013.

[ENS 2016] *Evaluated Nuclear Structure Data File*. `http://www.nndc.bnl.gov/ensdf/`, 2016. Last updated: 2016-06-24.

[Erler 2012] J. Erler, N. Birge, M. Kortelainen, W. Nazarewicz, E. Olsen, A. M Perhac and M. Stoitsov. *The limits of the nuclear landscape*. Nature, vol. 486, no. 7404, pages 509–512, 2012.

[Federman 1977] P. Federman and S. Pittel. *Towards a unified microscopic description of nuclear deformation*. Physics Letters B, vol. 69, no. 4, pages 385 – 388, 1977.

[Federman 1978] P. Federman and S. Pittel. *Hartree-Fock-Bogolyubov study of deformation in the* $Zr-Mo$ *region*. Physics Letters B, vol. 77, no. 1, pages 29 – 32, 1978.

[Federman 1979] P. Federman and S. Pittel. *Unified shell-model description of nuclear deformation*. Phys. Rev. C, vol. 20, pages 820–829, 1979.

[F.R.S. 1882] Lord Rayleigh F.R.S. *XX. On the equilibrium of liquid conducting masses charged with electricity*. Philosophical Magazine Series 5, vol. 14, no. 87, pages 184–186, 1882.

[Gamow 1930] G. Gamow. *Mass Defect Curve and Nuclear Constitution*. Proceedings of the Royal Society of London. Series A, Containing Papers of a Mathematical and Physical Character, vol. 126, no. 803, pages 632–644, 1930.

[Geiger 1909] H. Geiger and E. Marsden. *On a Diffuse Reflection of the* α*-Particles*. Proceedings of the Royal Society of London A: Mathematical, Physical and Engineering Sciences, vol. 82, no. 557, pages 495–500, 1909.

[George 2007a] S. George, S. Baruah, B. Blank, K. Blaum, M. Breitenfeldt, U. Hager, F. Herfurth, A. Herlert, A. Kellerbauer, H.-J. Kluge, M. Kretzschmar, D. Lunney, R. Savreux, S. Schwarz, L. Schweikhard and C. Yazidjian. *Ramsey Method of Separated Oscillatory Fields for High-Precision Penning Trap Mass Spectrometry*. Phys. Rev. Lett., vol. 98, page 162501, 2007.

[George 2007b] S. George, K. Blaum, F. Herfurth, A. Herlert, M. Kretzschmar, S. Nagy, S. Schwarz, L. Schweikhard and C. Yazidjian. *The Ramsey method in high-precision mass spectrometry with Penning traps: Experimental results*. International Journal of Mass Spectrometry, vol. 264, no. 2–3, pages 110 – 121, 2007.

[Gräff 1980] G. Gräff, H. Kalinowsky and J. Traut. *A direct determination of the proton electron mass ratio*. Zeitschrift für Physik A Atoms and Nuclei, vol. 297, no. 1, pages 35–39, 1980.

[Hager 2006] U. Hager, T. Eronen, J. Hakala, A. Jokinen, V. S. Kolhinen, S. Kopecky, I. Moore, A. Nieminen, M. Oinonen, S. Rinta-Antila, J. Szerypo and J. Äystö. *First Precision Mass Measurements of Refractory Fission Fragments*. Phys. Rev. Lett., vol. 96, page 042504, 2006.

[Haxel 1949] O. Haxel, J. H. D. Jensen and H. E. Suess. *On the "Magic Numbers" in Nuclear Structure*. Phys. Rev., vol. 75, pages 1766–1766, 1949.

[Herfurth 2001] F. Herfurth, J. Dilling, A. Kellerbauer, G. Bollen, S. Henry, H.-J. Kluge, E. Lamour, D. Lunney, R.B. Moore, C. Scheidenberger, S. Schwarz, G. Sikler and J. Szerypo. *A linear radiofrequency ion trap for accumulation, bunching, and emittance improvement of radioactive ion beams*. Nuclear Instruments and Methods in Physics Research Section A: Accelerators, Spectrometers, Detectors and Associated Equipment, vol. 469, no. 2, pages 254 – 275, 2001.

[Heyde 2011] K. Heyde and J. L. Wood. *Shape coexistence in atomic nuclei*. Rev. Mod. Phys., vol. 83, pages 1467–1521, 2011.

[Hilaire 2007] S. Hilaire and M. Girod. *Large-scale mean-field calculations from proton to neutron drip lines using the D1S Gogny force*. The European Physical Journal A, vol. 33, no. 2, pages 237–241, 2007.

[Hill 1953] D. L. Hill and J. A. Wheeler. *Nuclear Constitution and the Interpretation of Fission Phenomena*. Phys. Rev., vol. 89, pages 1102–1145, 1953.

[Hogg 1953] B. G. Hogg and H. E. Duckworth. *Evidence for a Region of Extra Nuclear Stability between the 82- and 126-Neutron Shells*. Phys. Rev., vol. 91, pages 1289–1290, 1953.

[Hotchkis 1991] M.A.C. Hotchkis, J.L. Durell, J.B. Fitzgerald, A.S. Mowbray, W.R. Phillips, I. Ahmad, M.P. Carpenter, R.V.F. Janssens, T.L. Khoo, E.F. Moore, L.R. Morss, Ph. Benet and D. Ye. *Rotational bands in the mass 100 region*. Nuclear Physics A, vol. 530, no. 1, pages 111 – 134, 1991.

[Iribarne 1976] J. V. Iribarne and B. A. Thomson. *On the evaporation of small ions from charged droplets*. The Journal of Chemical Physics, vol. 64, no. 6, 1976.

[Ishida 2004] Y. Ishida, M. Wada, Y. Matsuo, I. Tanihata, A. Casares and H. Wollnik. *A time-of-flight mass spectrometer to resolve isobars*. Nuclear Instruments and Methods in Physics Research Section B: Beam Interactions with Materials and Atoms, vol. 219–220, pages 468 – 472, 2004. Proceedings of the Sixteenth International Conference on Ion Beam Analysis.

[Ishida 2005] Y. Ishida, M. Wada and H. Wollnik. *A multi-reflection time-of-flight mass spectrometer for mass measurements of short-lived nuclei*. Nuclear Instruments and Methods in Physics Research Section B: Beam Interactions with Materials and Atoms, vol. 241, no. 1–4, pages 983 – 985, 2005.

[Johansson 1965] S.A.E. Johansson. *Gamma de-excitation of fission fragments*. Nuclear Physics, vol. 64, no. 1, pages 147 – 160, 1965.

[Keim 1995] M. Keim, E. Arnold, W. Borchers, U. Georg, A. Klein, R. Neugart, L. Vermeeren, R.E. Silverans and P. Lievens. *Laser-spectroscopy measurements of* $^{72\breve{}96}$*Kr spins, moments and charge radii*. Nuclear Physics A, vol. 586, no. 2, pages 219 – 239, 1995.

[Kellerbauer 2003] A. Kellerbauer, K. Blaum, G. Bollen, F. Herfurth, H.-J. Kluge, M. Kuckein, E. Sauvan, C. Scheidenberger and L. Schweikhard. *From direct to absolute mass measurements: A study of the accuracy of ISOLTRAP*. The European Physical Journal D - Atomic, Molecular, Optical and Plasma Physics, vol. 22, no. 1, pages 53–64, 2003.

[Ketter 2015] G. J. Ketter. *Theoretical treatment of miscellaneous frequency-shifts in Penning traps with classical perturbation theory*. Ph.d. dissertation, 2015.

[Klawitter 2016] R. Klawitter, A. Bader, M. Brodeur, U. Chowdhury, A. Chaudhuri, J. Fallis, A. T. Gallant, A. Grossheim, A. A. Kwiatkowski, D. Lascar, K. G. Leach, A. Lennarz, T. D. Macdonald, J. Pearkes, S. Seeraji, Simon M. C. , V. V. Simon, B. E. Schultz and J. Dilling. *Mass measurements of neutron-rich Rb and Sr isotopes*. Phys. Rev. C, vol. 93, page 045807, 2016.

[Konenkov 2002] N. V. Konenkov, M. Sudakov and D. J. Douglas. *Matrix methods for the calculation of stability diagrams in quadrupole mass spectrometry*. Journal of the American Society for Mass Spectrometry, vol. 13, no. 6, pages 597–613, 2002.

[Kortelainen 2010] M. Kortelainen, T. Lesinski, J. Moré, W. Nazarewicz, J. Sarich, N. Schunck, M. V. Stoitsov and S. Wild. *Nuclear energy density optimization*. Phys. Rev. C, vol. 82, page 024313, 2010.

[Kortelainen 2012] M. Kortelainen, J. McDonnell, W. Nazarewicz, P.-G. Reinhard, J. Sarich, N. Schunck, M. V. Stoitsov and S. M. Wild. *Nuclear energy density optimization: Large deformations*. Phys. Rev. C, vol. 85, page 024304, 2012.

[Kreim 2013] S. Kreim, D. Atanasov, D. Beck, K. Blaum, Ch. Böhm, Ch. Borgmann, M. Breitenfeldt, T.E. Cocolios, D. Fink, S. George, A. Herlert, A. Kellerbauer, U. Köster, M. Kowalska, D. Lunney, V. Manea, E. Minaya Ramirez, S. Naimi, D. Neidherr, T. Nicol, R.E. Rossel, M. Rosenbusch, L. Schweikhard, J. Stanja, F. Wienholtz, R.N. Wolf and K. Zuber. *Recent exploits of the ISOLTRAP mass spectrometer*. Nuclear Instruments and Methods in Physics Research Section B: Beam Interactions with Materials and Atoms, vol. 317, Part B, pages 492 – 500, 2013. {XVIth} International Conference on ElectroMagnetic Isotope Separators and Techniques Related to their Applications, December 2–7, 2012 at Matsue, Japan.

[Kretzschmar 1999] M. Kretzschmar. *A quantum mechanical model of Rabi oscillations between two interacting harmonic oscillator modes and the interconversion of modes in a Penning trap*. AIP Conference Proceedings, vol. 457, no. 1, 1999.

[Kugler 2000] E. Kugler. *The ISOLDE facility*. Hyperfine Interactions, vol. 129, no. 1, pages 23–42, 2000.

[Kumar 1985] Ashok Kumar and M. R. Gunye. *Nuclear structure of Sr, Zr, and Mo isotopes*. Phys. Rev. C, vol. 32, pages 2116–2121, 1985.

[Lhersonneau 1990] G. Lhersonneau, H. Gabelmann, N. Kaffrell, K. L. Kratz, B. Pfeiffer and K. Heyde. *Saturation of deformation at* $N = 60$ *in the Sr isotopes*. Zeitschrift für Physik A Atomic Nuclei, vol. 337, no. 2, pages 143–148, 1990.

[Lhersonneau 1995] G. Lhersonneau, H. Gabelmann, B. Pfeiffer and K. L. Kratz. *Structure of the highly deformed nucleus* $^{101}Sr^{63}$ *and evidence for identical K=3/2 bands*. Zeitschrift für Physik A Hadrons and Nuclei, vol. 352, no. 3, pages 293–301, 1995.

[Lievens 1991] P. Lievens, R.E. Silverans, L. Vermeeren, W. Borchers, W. Neu, R. Neugart, K. Wendt, F. Buchinger and E. Arnold. *Nuclear ground state properties of 99Sr by collinear laser spectroscopy with non-optical detection*. Physics Letters B, vol. 256, no. 2, pages 141 – 145, 1991.

[Lindroos 2004] Mats Lindroos. *Review of ISOL-type radioactive beam facilities*. Proceedings of EPAC 2004, Lucerne, Switzerland, pages 45–49, 2004.

[Lunney 2003] D. Lunney, J. M. Pearson and C. Thibault. *Recent trends in the determination of nuclear masses*. Rev. Mod. Phys., vol. 75, pages 1021–1082, 2003.

[Mack 1970] L. L. Mack, P. Kralik, A. Rheude and M. Dole. *Molecular Beams of Macroions. II.* The Journal of Chemical Physics, vol. 52, no. 10, 1970.

[Manea 2013] V. Manea, D. Atanasov, D. Beck, K. Blaum, C. Borgmann, R. B. Cakirli, T. Eronen, S. George, F. Herfurth, A. Herlert, M. Kowalska, S. Kreim, Yu. A. Litvinov, D. Lunney, D. Neidherr, M. Rosenbusch, L. Schweikhard, F. Wienholtz, R. N. Wolf and K. Zuber. *Collective degrees of freedom of neutron-rich $A \approx 100$ nuclei and the first mass measurement of the short-lived nuclide ^{100}Rb*. Phys. Rev. C, vol. 88, page 054322, 2013.

[Marsh 2013] B.A. Marsh, B. Andel, A.N. Andreyev, S. Antalic, D. Atanasov, A.E. Barzakh, B. Bastin, Ch. Borgmann, L. Capponi, T.E. Cocolios, T. Day Goodacre, M. Dehairs, X. Derkx, H. De Witte, D.V. Fedorov, V.N. Fedosseev, G.J. Focker, D.A. Fink, K.T. Flanagan, S. Franchoo, L. Ghys, M. Huyse, N. Imai, Z. Kalaninova, U. Köster, S. Kreim, N. Kesteloot, Yu. Kudryavtsev, J. Lane, N. Lecesne, V. Liberati, D. Lunney, K.M. Lynch, V. Manea, P.L. Molkanov, T. Nicol, D. Pauwels, L. Popescu, D. Radulov, E. Rapisarda, M. Rosenbusch, R.E. Rossel, S. Rothe, L. Schweikhard, M.D. Seliverstov, S. Sels, A.M. Sjödin, V. Truesdale, C. Van Beveren, P. Van Duppen, K. Wendt, F. Wienholtz, R.N. Wolf and S.G. Zemlyanoy. *New developments of the in-source spectroscopy method at RILIS/ISOLDE*. Nuclear Instruments and Methods in Physics Research Section B: Beam Interactions with Materials and Atoms, vol. 317, Part B, pages 550 – 556, 2013. XVIth International Conference on ElectroMagnetic Isotope Separators and Techniques Related to their Applications, December 2–7, 2012 at Matsue, Japan.

[Mayer 1949] M.G. Mayer. *On Closed Shells in Nuclei. II.* Phys. Rev., vol. 75, pages 1969–1970, 1949.

[Mayer 1950] M.G. Mayer. *Nuclear Configurations in the Spin-Orbit Coupling Model. I. Empirical Evidence*. Phys. Rev., vol. 78, pages 16–21, 1950.

[Mayer 1964] M. G. Mayer. *The shell model*. Physics: 1963-1970, vol. 4, page 20, 1964.

[Möller 1981] P. Möller and J.R. Nix. *Nuclear mass formula with a Yukawa-plus-exponential macroscopic model and a folded-Yukawa single-particle potential*. Nuclear Physics A, vol. 361, no. 1, pages 117 – 146, 1981.

[Moller 1995] P. Moller, J.R. Nix, W.D. Myers and W.J. Swiatecki. *Nuclear Ground-State Masses and Deformations*. Atomic Data and Nuclear Data Tables, vol. 59, no. 2, pages 185 – 381, 1995.

[Mukherjee 2008] M. Mukherjee, D. Beck, K. Blaum, G. Bollen, J. Dilling, S. George, F. Herfurth, A. Herlert, A. Kellerbauer, H. J. Kluge, S. Schwarz, L. Schweikhard and C. Yazidjian. *ISOLTRAP: An on-line Penning trap for mass spectrometry on short-lived nuclides*. The European Physical Journal A, vol. 35, no. 1, pages 1–29, 2008.

[Myers 1966] William D. Myers and Wladyslaw J. Swiatecki. *Nuclear masses and deformations*. Nuclear Physics, vol. 81, no. 1, pages 1 – 60, 1966.

[Myers 1974] W.D Myers and W.J Swiatecki. *The nuclear droplet model for arbitrary shapes*. Annals of Physics, vol. 84, no. 1, pages 186 – 210, 1974.

[Naimi 2010a] S. Naimi. *Onsets of nuclear deformation from measurements with the Isoltrap mass spectrometer*. PhD thesis, Citeseer, 2010.

[Naimi 2010b] S. Naimi, G. Audi, D. Beck, K. Blaum, Ch. Böhm, Ch. Borgmann, M. Breitenfeldt, S. George, F. Herfurth, A. Herlert, M. Kowalska, S. Kreim, D. Lunney, D. Neidherr, M. Rosenbusch, S. Schwarz, L. Schweikhard and K. Zuber. *Critical-Point Boundary for the Nuclear Quantum Phase Transition Near* $A = 100$ *from Mass Measurements of* ^{96,97}Kr. Phys. Rev. Lett., vol. 105, page 032502, 2010.

[Naimi 2013] S. Naimi, S. Nakamura, Y. Ito, H. Mita, K. Okada, A. Ozawa, P. Schury, T. Sonoda, A. Takamine, M. Wada and H. Wollnik. *An rf-carpet electrospray ion source to provide isobaric mass calibrants for trans-uranium elements.* International Journal of Mass Spectrometry, vol. 337, pages 24 – 28, 2013.

[Nazarewicz 1985] W. Nazarewicz, J. Dudek, R. Bengtsson, T. Bengtsson and I. Ragnarsson. *Microscopic study of the high-spin behaviour in selected* $A \simeq 80$ *nuclei.* Nuclear Physics A, vol. 435, no. 2, pages 397 – 447, 1985.

[Nilsson 1955] S.G. Nilsson. *K. Dan. Vidensk. Selsk, Math.* Fys. Medd, vol. 29, 1955.

[Nobelprize.org 1989] Nobelprize.org. *Hans G. Dehmelt*, 1989.

[Paul 1955] W. Paul and M. Raether. *Das elektrische Massenfilter.* Zeitschrift für Physik, vol. 140, no. 3, pages 262–273, 1955.

[Paul 1958] W. Paul, H. P. Reinhard and U. von Zahn. *Das elektrische Massenfilter als Massenspektrometer und Isotopentrenner.* Zeitschrift für Physik, vol. 152, no. 2, pages 143–182, 1958.

[Paul 1990] W. Paul. *Electromagnetic traps for charged and neutral particles.* Rev. Mod. Phys., vol. 62, pages 531–540, 1990.

[Pedder 2001] R. E. Pedder. *Practical quadrupole theory: graphical theory.* Excel Core Mass Spectrometers, Pittsburgh, PA, Extrel Application Note RA_2010 A, 2001.

[Penescu 2010] L. Penescu, R. Catherall, J. Lettry and T. Stora. *Development of high efficiency Versatile Arc Discharge Ion Source at CERN ISOLDEa).* Review of Scientific Instruments, vol. 81, no. 2, 2010.

[Penning 1936] F.M. Penning. *Die glimmentladung bei niedrigem druck zwischen koaxialen zylindern in einem axialen magnetfeld.* Physica, vol. 3, no. 9, pages 873 – 894, 1936.

[Petry 1988] R. F. Petry, J. D. Goulden, F. K. Wohn, John C. Hill, R. L. Gill and A. Piotrowski. *Decay of* ^{101}Sr *and the rotational structure of* ^{101}Y. Phys. Rev. C, vol. 37, pages 2704–2721, 1988.

[Pierce 1954] J.R. Pierce. Theory and design of electron beams. Bell Telephone Laboratories series. Van Nostrand, 1954.

[Rainwater 1950] J. Rainwater. *Nuclear Energy Level Argument for a Spheroidal Nuclear Model.* Phys. Rev., vol. 79, pages 432–434, 1950.

[Ring 2004] P. Ring and P. Schuck. The nuclear many-body problem. Springer Science & Business Media, 2004.

[Rodríguez-Guzmán 2010a] R. Rodríguez-Guzmán, P. Sarriguren and L. M. Robledo. *Signatures of shape transitions in odd-A neutron-rich rubidium isotopes.* Phys. Rev. C, vol. 82, page 061302, 2010.

[Rodríguez-Guzmán 2010b] R. Rodríguez-Guzmán, P. Sarriguren, L.M. Robledo and S. Perez-Martin. *Charge radii and structural evolution in Sr, Zr, and Mo isotopes.* Physics Letters B, vol. 691, no. 4, pages 202 – 207, 2010.

[Rodríguez 2014] T. R. Rodríguez. *Structure of krypton isotopes calculated with symmetry-conserving configuration-mixing methods.* Phys. Rev. C, vol. 90, page 034306, 2014.

[Rutherford 1911] E. Rutherford. *LXXIX. The scattering of* α *and* β *particles by matter and the structure of the atom.* Philosophical Magazine Series 6, vol. 21, no. 125, pages 669–688, 1911.

[Rutherford 1929] E. Rutherford, F. W. Aston, J. Chadwick, C. D. Ellis, G. Gamow, R. H. Fowler, O. W. Richardson and D. R. Hartree. *Discussion on the Structure of Atomic Nuclei.* Proceedings of the Royal Society of London A: Mathematical, Physical and Engineering Sciences, vol. 123, no. 792, pages 373–390, 1929.

[Savard 1991] G. Savard, St. Becker, G. Bollen, H.-J. Kluge, R.B. Moore, Th. Otto, L. Schweikhard, H. Stolzenberg and U. Wiess. *A new cooling technique for heavy ions in a Penning trap.* Physics Letters A, vol. 158, no. 5, pages 247 – 252, 1991.

[Schunck 2012] N. Schunck, J. Dobaczewski, J. McDonnell, W. Satuła, J.A. Sheikh, A. Staszczak, M. Stoitsov and P. Toivanen. *Solution of the Skyrme–Hartree–Fock–Bogolyubov equations in the Cartesian deformed harmonic-oscillator basis.: (VII) hfodd (v2.49t): A new version of the program.* Computer Physics Communications, vol. 183, no. 1, pages 166 – 192, 2012.

[Schury 2009] P. Schury, K. Okada, S. Shchepunov, T. Sonoda, A. Takamine, M. Wada, H. Wollnik and Y. Yamazaki. *Multi-reflection time-of-flight mass spectrograph for short-lived radioactive ions.* The European Physical Journal A, vol. 42, no. 3, pages 343–349, 2009.

[Schwarz 2011] S. Schwarz. *{RF} ion carpets: The electric field, the effective potential, operational parameters and an analysis of stability.* International Journal of Mass Spectrometry, vol. 299, no. 2–3, pages 71 – 77, 2011.

[Simon 2012] V. V. Simon, T. Brunner, U. Chowdhury, B. Eberhardt, S. Ettenauer, A. T. Gallant, E. Mané, M. C. Simon, P. Delheij, M. R. Pearson, G. Audi, G. Gwinner, D. Lunney, H. Schatz and J. Dilling. *Penning-trap mass spectrometry of highly charged, neutron-rich Rb and Sr isotopes in the vicinity of* $A \approx 100$. Phys. Rev. C, vol. 85, page 064308, 2012.

[Simpson 2006] G. S. Simpson, J. A. Pinston, D. Balabanski, J. Genevey, G. Georgiev, J. Jolie, D. S. Judson, R. Orlandi, A. Scherillo, I. Tsekhanovich, W. Urban and N. Warr. *High-spin μs isomer in* ^{98}Zr. Phys. Rev. C, vol. 74, page 064308, 2006.

[Sotty 2015] C. Sotty, M. Zielińska, G. Georgiev, D. L. Balabanski, A. E. Stuchbery, A. Blazhev, N. Bree, R. Chevrier, S. Das Gupta, J. M. Daugas, T. Davinson, H. De Witte, J. Diriken, L. P. Gaffney, K. Geibel, K. Hadyńska-Klęk, F. G. Kondev, J. Konki, T. Kröll, P. Morel, P. Napiorkowski, J. Pakarinen, P. Reiter, M. Scheck, M. Seidlitz, B. Siebeck, G. Simpson, H. Törnqvist, N. Warr and F. Wenander. $^{97}_{37}\mathrm{Rb}_{60}$*: The Cornerstone of the Region of Deformation around* $A \sim 100$. Phys. Rev. Lett., vol. 115, page 172501, 2015.

[Takamine 2005] A. Takamine, M. Wada, Y. Ishida, T. Nakamura, K. Okada, Y. Yamazaki, T. Kambara, Y. Kanai, T. M. Kojima, Y. Nakai, N. Oshima, A. Yoshida, T. Kubo, S. Ohtani, K. Noda, I. Katayama, P. Hostain, V. Varentsov and H. Wollnik. *Space-charge effects in the catcher gas cell of a rf ion guide.* Review of Scientific Instruments, vol. 76, no. 10, 2005.

[Takamine 2007] Takamine. *Precision laser spectroscopy of unstable beryllium isotopes using an RF ion guide system*. PhD thesis, 2007.

[Taylor 1965] G. I. Taylor and A. D. McEwan. *The stability of a horizontal fluid interface in a vertical electric field*. Journal of Fluid Mechanics, vol. 22, pages 1–15, 1965.

[Teer 1975] D. Teer and M. Dole. *Electrospray mass spectroscopy of macromolecule degradation in the electrospray*. Journal of Polymer Science: Polymer Physics Edition, vol. 13, no. 5, pages 985–995, 1975.

[Thibault 1981] C. Thibault, F. Touchard, S. Büttgenbach, R. Klapisch, M. de Saint Simon, H. T. Duong, P. Jacquinot, P. Juncar, S. Liberman, P. Pillet, J. Pinard, J. L. Vialle, A. Pesnelle and G. Huber. *Hyperfine structure and isotope shift of the D_2 line of* $^{76-98}$Rb *and some of their isomers*. Phys. Rev. C, vol. 23, pages 2720–2729, 1981.

[Treiner 1986] J. Treiner, W.D. Myers, W.J. Swiatecki and M.S. Weiss. *Bulk compression due to surface tension in Hartree-Fock, Thomas-Fermi and Droplet-model calculations*. Nuclear Physics A, vol. 452, no. 1, pages 93 – 104, 1986.

[Tretner 1960] W. Tretner. *An electrostatic mass spectroscope*. Vacuum, vol. 10, no. 1, pages 31 – 34, 1960.

[von Hahn 2016] R. von Hahn, A. Becker, F. Berg, K. Blaum, C. Breitenfeldt, H. Fadil, F. Fellenberger, M. Froese, S. George, J. Göck, M. Grieser, F. Grussie, E. A. Guerin, O. Heber, P. Herwig, J. Karthein, C. Krantz, H. Kreckel, M. Lange, F. Laux, S. Lohmann, S. Menk, C. Meyer, P. M. Mishra, O. Novotný, A. P. O'Connor, D. A. Orlov, M. L. Rappaport, R. Repnow, S. Saurabh, S. Schippers, C. D. Schröter, D. Schwalm, L. Schweikhard, T. Sieber, A. Shornikov, K. Spruck, S. Sunil Kumar, J. Ullrich, X. Urbain, S. Vogel, P. Wilhelm, A. Wolf and D. Zajfman. *The cryogenic storage ring CSR*. Review of Scientific Instruments, vol. 87, no. 6, 2016.

[Wada 2003] M. Wada, Y. Ishida, T. Nakamura, Y. Yamazaki, T. Kambara, H. Ohyama, Y. Kanai, T. M. Kojima, Y. Nakai, N. Ohshima, A. Yoshida, T. Kubo, Y. Matsuo, Y. Fukuyama, K. Okada, T. Sonoda, S. Ohtani, K. Noda, H. Kawakami and I. Katayama. *Slow RI-beams from projectile fragment separators*. Nuclear Instruments and Methods in Physics Research Section B: Beam Interactions with Materials and Atoms, vol. 204, pages 570 – 581, 2003. 14th International Conference on Electromagnetic Isotope Separators and Techniques Related to their Applications.

[Wang 2012] M. Wang, G. Audi, A.H. Wapstra, F.G. Kondev, M. MacCormick, X. Xu and B. Pfeiffer. *The Ame2012 atomic mass evaluation*. Chinese Physics C, vol. 36, no. 12, page 1603, 2012.

[Wang 2016] Z. M. Wang, A. B. Garnsworthy, C. Andreoiu, G. C. Ball, P. C. Bender, V. Bildstein, D. S. Cross, G. Demand, R. Dunlop, L. J. Evitts, P. E. Garrett, G. Hackman, B. Hadinia, S. Ketelhut, R. Krücken, K. G. Leach, A. T. Laffoley, D. Miller, M. Moukaddam, J. Pore, A. J. Radich, M. M. Rajabali, C. E. Svensson, A. Tan, E. Tardiff, C. Unsworth, A. Voss and P. Voss. *Observation of a large β-delayed neutron emission component in* ^{102}Rb *decay and identification of excited states in* ^{102}Sr. Phys. Rev. C, vol. 93, page 054301, 2016.

[Weizsäcker 1935] C. F. v. Weizsäcker. *Zur Theorie der Kernmassen*. Zeitschrift für Physik, vol. 96, no. 7, pages 431–458, 1935.

[Wienholtz 2013] F. Wienholtz, D. Beck, K. Blaum, Ch. Borgmann, M. Breitenfeldt, R. B. Cakirli, S. George, F. Herfurth, J.D. Holt, M. Kowalska*et al.* *Masses of exotic calcium isotopes pin down nuclear forces*. Nature, vol. 498, no. 7454, pages 346–349, 2013.

[Wigner 1937] E. Wigner. *On the Consequences of the Symmetry of the Nuclear Hamiltonian on the Spectroscopy of Nuclei.* Phys. Rev., vol. 51, pages 106–119, 1937.

[Wohn 1983] F. K. Wohn, John C. Hill, R. F. Petry, H. Dejbakhsh, Z. Berant and R. L. Gill. *Rotational Structure and Nilsson Orbitals for Highly Deformed Odd-A Nuclei in the* $A \sim 100$ *Region.* Phys. Rev. Lett., vol. 51, pages 873–876, 1983.

[Wohn 1986] F. K. Wohn, John C. Hill, C. B. Howard, K. Sistemich, R. F. Petry, R. L. Gill, H. Mach and A. Piotrowski. *Shape coexistence and level structure of* ^{100}Zr *from decay of the low-spin isomer of* ^{100}Y. Phys. Rev. C, vol. 33, pages 677–690, 1986.

[Wohn 1987] F. K. Wohn, John C. Hill, J. A. Winger, R. F. Petry, J. D. Goulden, R. L. Gill, A. Piotrowski and H. Mach. *Decay of* ^{100}Sr *and a "pairing-free"* $K^{\pi} = 1^{+}$ *rotational band in odd-odd* ^{100}Y. Phys. Rev. C, vol. 36, pages 1118–1128, 1987.

[Wolf 2012a] R. N. Wolf, G. Marx, M. Rosenbusch and L. Schweikhard. *Static-mirror ion capture and time focusing for electrostatic ion-beam traps and multi-reflection time-of-flight mass analyzers by use of an in-trap potential lift.* International Journal of Mass Spectrometry, vol. 313, pages 8 – 14, 2012.

[Wolf 2012b] R.N. Wolf, D. Beck, K. Blaum, Ch. Böhm, Ch. Borgmann, M. Breitenfeldt, F. Herfurth, A. Herlert, M. Kowalska, S. Kreim, D. Lunney, S. Naimi, D. Neidherr, M. Rosenbusch, L. Schweikhard, J. Stanja, F. Wienholtz and K. Zuber. *On-line separation of short-lived nuclei by a multi-reflection time-of-flight device.* Nuclear Instruments and Methods in Physics Research Section A: Accelerators, Spectrometers, Detectors and Associated Equipment, vol. 686, pages 82 – 90, 2012.

[Wolf 2013] R.N. Wolf, F. Wienholtz, D. Atanasov, D. Beck, K. Blaum, Ch. Borgmann, F. Herfurth, M. Kowalska, S. Kreim, Yu. A. Litvinov, D. Lunney, V. Manea, D. Neidherr, M. Rosenbusch, L. Schweikhard, J. Stanja and K. Zuber. *ISOLTRAP's multi-reflection time-of-flight mass separator/spectrometer.* International Journal of Mass Spectrometry, vol. 349–350, pages 123 – 133, 2013. 100 years of Mass Spectrometry.

[Wollnik 1990] H. Wollnik and M. Przewloka. *Time-of-flight mass spectrometers with multiply reflected ion trajectories.* International Journal of Mass Spectrometry and Ion Processes, vol. 96, no. 3, pages 267 – 274, 1990.

[Wu 2004] C. Y. Wu, H. Hua, D. Cline, A. B. Hayes, R. Teng, R. M. Clark, P. Fallon, A. Goergen, A. O. Macchiavelli and K. Vetter. *Multifaceted yrast structure and the onset of deformation in* ^{96,97}Sr *and* ^{98,99}Zr. Phys. Rev. C, vol. 70, page 064312, 2004.